

2)

# Modeling Orientation and Ocular Dominance Columns in the Visual Cortex

by

Darren Michael Pierre

Submitted to the Department of Physics  
in partial fulfillment of the requirements for the degree of

Master of Science


at the

MASSACHUSETTS INSTITUTE OF TECHNOLOGY

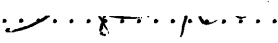
September 1997

© Darren Michael Pierre, MCMXCVII. All rights reserved.

The author hereby grants to MIT permission to reproduce and  
distribute publicly paper and electronic copies of this thesis document  
in whole or in part, and to grant others the right to do so.

Author .....  
 Department of Physics  
June 22, 1997

Certified by .....  
Mehran Kardar  
Professor of Physics  
Thesis Supervisor

Accepted by .....  
 George F. Koster  
Chairman, Departmental Graduate Committee

SEP 16 1997

LIBRARIES

Ad Majorem Dei Gloriam

*to my family*

# Modeling Orientation and Ocular Dominance Columns in the Visual Cortex

by

Darren Michael Pierre

Submitted to the Department of Physics  
on June 22, 1997, in partial fulfillment of the  
requirements for the degree of  
Master of Science

## Abstract

In this thesis, we develop a macroscopic model of the formation of ocular dominance and orientation columns in the mammalian visual cortex. We not only reproduce the static patterns of orientation pinwheels and ocular dominance stripes seen in the macaque monkey, but also model the development of these patterns, paying particular attention to the observed stability of the adult response.

We model ocular dominance as a scalar field. Initial conditions, reflecting small fluctuations around a binocular response, develop into a pattern of domains corresponding to the observed monocular bands. The domains are separated by domain walls where ocular dominance changes rapidly. Competition between short range excitations, which favor continuity, and long range inhibitions, which favor diversity, stabilize the domains and result in a pattern of stripes.

Orientation is modeled by a complex number to reflect both its preference and selectivity. An initial pattern, consisting of small fluctuations around zero selectivity, evolves into a pattern containing vortices, which are naturally associated with the observed pinwheels. Pairs of vortices of opposite circulation experience an effective attraction, and slowly move toward each other, eventually annihilating to create a more uniform response.

We are able to stabilize the pattern of vortices and reproduce observed correlations between the ocular dominance and orientation patterns, by including a local coupling between the two fields. It is natural to think of this coupling as a result of the cortex's limited computational capacity, i.e. areas which respond strongly to orientation cannot simultaneously respond strongly to ocular dominance. In addition to coupling between ocular dominance and orientation patterns, we consider weak coupling to a large number of unknown fields represented by static randomness. This more generalized coupling can explain the presence of stable orientation patterns in animals which do not have detectable ocular dominance bands.

Thesis Supervisor: Mehran Kardar

Title: Professor of Physics

# Acknowledgments

First, I would like to thank Mehran Kardar for his continual guidance and support through all stages of this work. I especially appreciate his willingness to accommodate my changing plans and interests.

Second, I would like to thank George Benedek and Peter Dayan for agreeing to sit on my thesis committee and for adjusting to my constricted schedule.

I also wish to thank Mriganka Sur, Bhavin Sheth, and Jitendra Sharma for their useful conversations and background for this work. Without their their guidance, it would have been impossible to know where to start.

Finally, I wish to acknowledge the financial support of the National Science Foundations (through Grant No. DMR-93-03667) and the Office of Naval Research (through the ONR Fellowship Program).

# Contents

<b>1</b>	<b>Introduction</b>	<b>14</b>
1.1	Anatomy and Basic Physiology of the Visual System . . . . .	16
1.1.1	Nerve Cells . . . . .	16
1.1.2	Eyes and Retina . . . . .	18
1.1.3	Optic Nerves and the Lateral Geniculate Nucleus . . . . .	20
1.1.4	Primary Visual Cortex . . . . .	22
1.1.5	Higher Cortical Areas . . . . .	23
1.2	Physiology of the Primary Visual Cortex . . . . .	25
1.2.1	Experimental Methods . . . . .	25
1.2.2	Ocular Dominance . . . . .	30
1.2.3	Orientation Preference and Selectivity . . . . .	35
1.2.4	Coupling between Ocular Dominance and Orientation . . . . .	39
1.2.5	Summary of Characteristic to be Modeled . . . . .	40
1.3	Previous Models of the Primary Visual Cortex . . . . .	40
1.3.1	Structural Models . . . . .	42
1.3.2	Static Filter Models . . . . .	45
1.3.3	Evolving Field Models . . . . .	47
1.3.4	Neural Network Models . . . . .	52
<b>2</b>	<b>Macroscopic Modeling</b>	<b>55</b>
2.1	General Methodology . . . . .	55
2.1.1	Length Scales . . . . .	56
2.1.2	Analytic Macroscopic Equations . . . . .	57

2.1.3	Cost Functions . . . . .	58
2.2	Equilibrium . . . . .	60
2.2.1	Phase Transitions . . . . .	61
2.2.2	Binary Alloys . . . . .	62
2.2.3	Superconductors . . . . .	64
2.3	Dynamics . . . . .	68
2.3.1	Systems with No Conservation Laws . . . . .	69
2.3.2	Systems with a Conserved Order Parameter . . . . .	70
2.3.3	Discrete Systems . . . . .	71
<b>3</b>	<b>Results of Modeling</b>	<b>73</b>
3.1	Ocular Dominance . . . . .	73
3.1.1	Local Variables and Cost Function . . . . .	74
3.1.2	Short-range Coupling . . . . .	76
3.1.3	Long-range Coupling . . . . .	81
3.1.4	Distribution of $ m_i $ . . . . .	92
3.1.5	Summary . . . . .	96
3.2	Orientation Preference and Selectivity . . . . .	98
3.2.1	Local Variables and the Cost Function . . . . .	99
3.2.2	Short-range Coupling . . . . .	100
3.2.3	Long-range Coupling . . . . .	103
3.2.4	Distribution of $ z_i $ . . . . .	105
3.2.5	Summary . . . . .	109
3.3	Coupling between Ocular Dominance and Orientation Selectivity . . .	112
3.3.1	Local Variables and the Cost Function . . . . .	112
3.3.2	Interactions . . . . .	114
3.3.3	Distribution of $ z_i $ and $ m_i $ . . . . .	119
3.3.4	Summary . . . . .	120
<b>4</b>	<b>Conclusions</b>	<b>123</b>

# List of Figures

1-1	Schematic drawing of the retina showing photoreceptors, horizontal cells, bipolar cells, amacrine cells, and ganglion cells. Information flows vertically from the photoreceptors, to the bipolar cells, then to the ganglion cells. It is carried laterally by the horizontal cells and amacrine cells. Figure reproduced with permission from <i>Principles of Neural Science</i> by Eric Kandel et. al.[1] . . . . .	19
1-2	Schematic drawing of the visual system from the eyes to the primary visual cortex. Fibers from the right side of each retina lead to different layers in the right lateral geniculate nucleus (LGN). A small number terminate in the pretectum and superior colliculus. Fibers from the right LGN travel to the right primary visual cortex, still segregated by the eye to which they respond. They terminate in layer IVc of the primary visual cortex. A parallel system exists on the left half of the brain, but it is not shown. Figure reproduced with permission from <i>Principles of Neural Science</i> by Eric Kandel et. al.[1] . . . . .	21
1-3	The organization of 32 visual areas as suggested by Felleman and Van Essen. Figure reproduced with permission from “Distributed Hierarchical Processing in the Primate Cerebral Cortex” appearing in <i>Cerebral Cortex</i> . [2] . . . . .	24

1-4	Reconstruction of ocular dominance bands in the monkey primary visual cortex based on data from LeVay's reduced silver stain. (Scale shows mm.) In (a) the operculum is shown, in (b) the roof of calcarine fissure, and in (c) the leaves joining the roof to the stem. The dashed line is the border between areas V1 and V2. The dotted line shows places where the cortex is folded under itself. The dark lines in the figure itself are the domain walls of the ocular dominance bands. Note that adjacent bands never join. Figure reprinted from "The Pattern of Ocular Dominance Columns in Macaque Visual Cortex Revealed by a Reduced Silver Stain", by Simon LeVay et. al. appearing in the <i>Journal of Comparative Neurology</i> . Copyright ©Wiley-Liss, Inc.. Reprinted by permission by Wiley-Liss, Inc., a subsidiary of John Wiley & Sons, Inc.[3] . . . . .	32
1-5	Two pairs of orientation and selectivity patterns. (a, c) Orientation preference and (b, d) selectivity in the monkey determined from optical imaging. In (a, c) different colors encode different angular preference as shown in the key on the left. In (b, d) lighter areas are more selective than darker ones. Figure reproduced with permission from "Orientation Selectivity, Preference, and Continuity in the Monkey Striate Cortex" by Gary Blasdel appearing in <i>The Journal of Neuroscience</i> .[4]	37
1-6	The distribution of selectivity in the visual cortex. The squares indicated data for the ferret provided by Mriganka Sur's group at MIT, while the line is a least squares fit to the form $r \exp(-\alpha r^2)$ In this case $\alpha = -14.3$ . . . . .	38
1-7	The icecube model developed by Hubel and Wiesel. R and L indicate ocular dominance columns responding to the right and left eye. Regions with a small diagonal line indicate orientation bands. This figure is not meant to imply that ocular dominance bands cross orientation bands orthogonally or that the bands are straight. . . . .	43



1-8	(a) The pinwheel model as originally developed by Braitenberg and Braitenberg. The orientation is linked to the isorientation lines. Singularities with $+360^\circ$ and $-180^\circ$ are present. (b) The pinwheel model as modified by Gotz. Orientation is no longer bound to isorientation lines, and $\pm 180^\circ$ singularities are present. . . . .	44
3-1	Simulated ocular dominance patterns using only nearest neighbor interactions. Dark areas prefer one eye, while light areas prefer the other. Very little grey is apparent indicating few binocular cells. Although domains appear, they do not form stripes with a regular width. As a result of an artifact of the discretization this pattern is metastable and does not coarsen to give a single uniform domain. In this simulation on a $200 \times 200$ lattice, $k_s = 0.125$ , and $\Delta t = 0.05$ . The simulation is interrupted when all $\Delta m / \Delta t$ becomes less than $10^{-10}$ . . . . .	79
3-2	Simulated ocular bands generated by iterating Eq. (3.13). (Eq. (3.12) yields very similar patterns.) A totally isotropic interaction is sufficient to form this pattern of bands. In this simulation on a $200 \times 200$ lattice, $k_s^{(2)} = 0.05$ , $k_l^{(2)} = -0.025$ , $\Delta t = 0.025$ and $L = 10$ . The simulation is interrupted after 40 time constants when the mean value of $\Delta m / \Delta t$ is less than 0.01. . . . .	84
3-3	Simulated ocular dominance bands according to Eq. (3.12) for a variety of values of $k_l^{(1)}$ -0.1 (a), -0.15 (b), -0.2 (c), and -0.5 (d). Persistence increases with increasing $k_l^{(1)}$ , but cannot be strengthened indefinitely. All simulations started from the same initial conditions on a $200 \times 200$ lattice, with $k_s^{(2)} = 0.5$ , $L = 10$ , and $\Delta t = 0.05$ . The simulations are interrupted when the mean value of $\Delta m / \Delta t$ is less than 0.01. . . . .	86
3-4	Simulated ocular bands generated by iterating Eq. (3.13) with the edges set to $m = 0$ . Compare with Fig. (3-2) which uses the same initial conditions and parameters but periodic boundary conditions. Note that the bands tend to meet the edges at right angles. . . . .	87

3-5	Alternating stripes of positive and negative ocular dominance ( $m = \pm 1$ ) with width $L$ meet an $m = 0$ half plane at an angle $\theta$ to the normal.	89
3-6	The cost of an edge intersecting stripes at an angle $\theta$ to the normal. The cost is given per unit length of the edge. The solid line is a calculation for a continuous system, while the squares are from a discrete model on a hexagonal with a stripe width of 10 sites. In both cases the interaction occurs at the same range as the stripe width. . . . .	90
3-7	The cost of stripes in the bulk as a function of the angle between the stripes and the underlying hexagonal lattice. The cost repeats with a period of $60^\circ$ and has a minimum at 0 where the stripes are aligned with the lattice. The calculation is performed on a discrete system with a stripe width of 10 sites. . . . .	91
3-8	A simulation of monocular deprivation by including a uniform field of $H = 3.5$ . Compare this figure with Fig. (3-2) which uses the same initial conditions and parameters, but has $H = 0$ . . . . .	93
3-9	The distribution of the widths of the repressed in a one dimensional simulation for several value of $H$ . Notice that the peak of the distribution remains fixed. Here $L = 10$ , $k_s^{(2)} = 0.1$ , $k_l^{(2)} = -0.1$ , and $\Delta_l = 0.1$ . . . . .	94
3-10	The profile of a domain wall in one dimension. The field evolved according to Eq. (3.13) with $L = 20$ , $k_s^{(2)} = 0.05$ , and $k_l^{(2)} = 0$ The presence of the domain wall was forced by keeping the left edge at $m_i = +1$ and the right edge at $m_i = -1$ . . . . .	95
3-11	The discontinuity in $m_i$ at the domain wall in a one dimensional simulation as a function of the range of the positive interactions. The size of the discontinuity is expressed as a fraction of the value in the bulk. Notice that a finite jump continues to exist even for very long range interactions. . . . .	96
3-12	A typical distribution of $ m_i $ for a two dimensional simulation using Eq. (3.13). The distribution shown corresponds to Fig. (3-2). . . . .	97

3-13	Simulated orientation pattern generated by iterating Eq. (3.25). Each of the 8 colors shown represents a range of $22.5^\circ$ . The colors cycle through $180^\circ$ of preference, light green $\rightarrow$ yellow $\rightarrow$ orange $\rightarrow$ red $\rightarrow$ violet $\rightarrow$ dark blue $\rightarrow$ light blue $\rightarrow$ dark green $\rightarrow$ light green $\rightarrow$ etc. In this simulation on a $200 \times 200$ lattice, $k'_s = 0.125$ and $\Delta t = 0.05$ . The simulation is interrupted after 50 time constants. . . . .	102
3-14	The same simulated orientation pattern shown in Fig. (3-13) but after 250 time constants. The number of vortices is greatly reduced. The vortices shown eventually annihilate after additional iterations. . . .	104
3-15	Simulated orientation pattern generated by iterating Eq. (3.26). The long-range coupling does not stop the annihilation of vortices but rather causes the formation of rainbow-like bands. In this simulation on a $200 \times 200$ lattice, $k'_s = 0.1$ , $k'_l = -0.01$ , and $\Delta t = 0.1$ . The simulation is interrupted after 100 time constants. . . . .	106
3-16	Simulated selectivity pattern corresponding to Fig. (3-13). Darker areas are less selective, i.e. have lower values of $ z_i $ . . . . .	107
3-17	Simulated selectivity pattern generated by iterating Eq. (3.28). Here $h'_i$ is distributed uniformly over the interval $(-2, 2)$ , to widen the distribution of $ z_i $ . The large amount of randomness needed to widen the distribution of $ z_i $ disrupts the pattern of selectivity. In this simulation on a $100 \times 100$ lattice, $k'_s = 0.05$ , $\Delta t = 0.05$ . The simulation is interrupted after 2500 time constants when the pattern appeared to be stable. . . . .	110
3-18	Simulated orientation pattern generated by iterating Eq. (3.28). This pattern is stable under further iteration. The presence of a quenched random field can stop the annihilation of vortices. This orientation pattern corresponds to the selectivity pattern shown in Fig. (3-17) . . .	111

3-19	Simulated (a) orientation preference, (b) orientation selectivity, and (c) ocular dominance patterns generated by iterating Eqs. (3.36). The coupling between fields prevents the further annihilation of singularities. The locations of the singularities and ocular dominance domain walls are clearly visible in the orientation selectivity. In this simulation on a 100x100 lattice, $\gamma = -0.1$ , $k_s^{(2)} = -0.05$ , $k_l^{(2)} = -0.025$ , $L = 10$ , $k'_s = 0.05$ , and $\Delta t_m = \Delta t_z = 0.025$ . The equations of motion were iterated for 500 time constants. The pattern appeared to be stable during the last 250 time constants. . . . .	116
3-20	The distribution of (a) $ z_i $ and (b) $ m_i $ , corresponding to the patterns in Fig. (3-19). . . . .	121

# List of Tables

1.1	Important properties of ocular dominance and orientation to be considered when evaluating and developing models. . . . .	41
-----	--	----

# Chapter 1

## Introduction

Richard Feynman once remarked with amazement that the brain could reconstruct a complete image from the tiny bit of light passing through a 2 mm pupil.[5] The brain's amazing abilities of reconstruction and perception are of great interest. They are both a gateway to understanding higher brain functions, and a source of ideas for developing artificial systems capable of image recognition.

Since the 1940's, cells in the eyes and midbrain were known to respond to spots of light at different locations.[6, 7] In 1958 David Hubel and Torsten Wiesel were searching for cells in the primary visual cortex that responded similarly. They showed animal subjects hundreds of slides, each with a dot at a different location. To their disappointment they found few cells responding to their dots. However, by accident, they discovered that the cells responded best not to the dots on the slides, but to the dark shadow cast by the edge of slides. Further, they found that cells responded only to dark lines of specific orientations. The visual cortex contained orientation specific cells.[8]

In the following decades Hubel, Wiesel, and many others performed extensive studies of the visual cortex of the cat and macaque monkey, finding not only orientation specific cells, but also cells which favored one eye over the other. Based on such results, the first simple models of the structure of the primary visual cortex were proposed. In many ways these early models were qualitatively correct, but they contained extreme regularity in response that was not to be found in the actual

cortex.

As more advanced experimental techniques were developed and larger portions of the primary visual cortex were studied, it became clear that the cortex's response was disordered on length scales comparable to the size of the cortex. The next generation of models started with random initial conditions and evolved them in different ways. The initial randomness then developed into globally disordered patterns. Many of the models made reasonable predictions for the behavior of the cortex, but the experimental data on the cortex was too limited at that time to make quantitative comparisons.

This remained true until the development of optical imaging. In 1986 Gary Blasdel used optical imaging to study large areas of the primary visual cortex in vivo. This greatly increased the amount of data available. Correlations were found between ocular dominance and orientation preference. Detailed studies were performed on juvenile animals to observe the development before it was complete. This work spurred the development of additional models, and more importantly allowed quantitative comparison between models and to experimental observations.

In this thesis we propose a new model of the primary visual cortex, which builds upon some of the previous models, but is different in significant ways. Our approach relies upon a Landau-Ginzburg expansion which is a well developed tool in statistical mechanics. Our model allows for the easy identification and exploitation of symmetries and interacting quantities.

The remainder of this introduction looks at what is known about the primary visual cortex. First, the anatomy of the entire visual system is surveyed. Next, the physiology of the primary visual cortex is examined in detail. Finally, existing models are examined and compared. Chap. (2) explains the Landau-Ginzburg approach, and its successful use in a variety of other problems. Chap. (3) describes the details of our model, its implementation, and results. Lastly, Chap. (4) reviews the major results of our work.

# 1.1 Anatomy and Basic Physiology of the Visual System

In order to develop a useful model of the primary visual cortex, it is important that we have a basic understanding of the visual system. While it is possible to create a model of the primary visual cortex by looking at it in isolation, this would ignore a wealth of information about how it interacts with the rest of the visual system. Information from the outside world reaches the primary visual cortex by passing through the eyes and then the thalamus, where some processing occurs. After further processing in the primary visual cortex, the information is sent to higher cortical areas where perception arises. By studying these other areas we can better understand the function of the primary visual cortex.

We will describe here the anatomy and basic physiology of the visual system. Anatomy refers to physical structures and physical properties, while physiology refers to the response of the system to outside stimuli. Many different species including ferrets, cats, monkeys, and humans have played important roles in expanding our understanding of the mammalian visual system. Luckily, it is not necessary to describe the visual systems of all these species, most are quite similar in general design. The cursory description that follows applies to most species. When details vary between species, we choose to focus on the macaque monkey whenever possible. The macaque has been extensively studied and is quite similar to the human, the ultimate goal of our understanding. We draw our description of the visual system from *Principles of Neural Science* by Eric Kandel et. al.[1] which deals mainly with humans, and *An Introduction to the Biology of Vision* by James Mcllwain[5], as well as the papers explicitly cited.

## 1.1.1 Nerve Cells

The visual system is composed of discrete cells called neurons. The human brain is believed to contain about 100 billion neurons of as many as 10,000 different types.[1]



Nonetheless, there are many features common to typical neurons. Most neurons have a cell body or soma. A frequently branching network of fibers called dendrites connects to the cell body and collects input. A single long fiber called the axon also extends from the cell body and carries the cell's output. The axon may travel as far as a meter, but eventually terminates into many branching fibers forming an arbor. These fibers make contact to the dendrites of other cells. The junction between an axon and a dendrite is called a synapse. A single cell may have as many as 10,000 synapses to other cells.

The nervous system uses both electrical and chemical signals to carry information. Within a neuron, information is carried by electrical pulses called action potentials. When input from the dendrites or spontaneous activity triggers a cell, an electrical pulse is formed in the cell body and propagates down the axon. Upon reaching the arbor, the pulse triggers the release of chemical neurotransmitters into the synapses. The synapses are nothing more than small gaps between axons and dendrites. The neurotransmitters are picked up by cells, either through dendrites or directly by the cell body. This in turn may cause other cells to fire, repeating the process.

Information is carried by discrete pulses, the action potentials. The number of pulses can be integrated over time to give the level of activity for a cell. This level can be used to track how a cell responds to a variety of stimuli. However, this discards any information which may be contained in the timing of individual pulses. In the visual system, it is unclear if the timing contains useful information. Other systems are known to use this timing information at least in certain circumstances. For example, the auditory system uses timing and rate information when localizing sounds. Firing rates are used to compare the sound intensity at the two ears, while timing information is used to compare the arrival times of the sound at the two ears.

The brain relies on trillions of synapses among billions of neurons to do all its tasks. This presents a developmental problem. The amount of information required to specify all the connections exceeds the total information in DNA by several orders of magnitude. Thus, some form of self organization is required to allow a smaller amount of genetically stored information to determine the developmental pattern

of the brain. Mathematically describing the development of a homogeneous organ with only local connectivity requires only a few simple rules. However, describing the development of the brain with its many heterogeneous long-range connections is much more difficult.

Studying the self organization of one part of the brain, the primary visual cortex, is the goal of this work. The primary visual cortex is composed of two generic types of neurons, although each type has many variants. Large pyramidal cells have long axons that project out to regions beyond the primary visual cortex. Smaller stellate cells mainly connect locally within the primary visual cortex. The stellate cells are further subdivided into spiny stellate cells which tend to excite the cells to which they connect, and smooth stellate cells which tend to inhibit other cells.

### **1.1.2 Eyes and Retina**

All information about the visual field, the outside world as we see it, enters the body through the eyes. The lens of the eye creates an image of the visual field on the back of the eye, called the retinal image.

The retina is composed of five types of neurons, see Fig. (1-1). Photoreceptors (rods and cones) change the retinal image into a pattern of neural activity. (Exactly what is meant by neural activity will be discussed later.) Horizontal cells, bipolar cells, and amacrine cells carry information within the retina. Ganglion cells carry the information from the retina to other parts of the brain.

Many neurons in the visual system have well defined receptive fields. The receptive field is an area of the retinal image that affects the activity of the neuron. The photoreceptors have very simple receptive fields, namely the area of the retinal image falling directly onto them. Ganglion cells have small circular receptive fields centered in the nearby area of the retinal image. Their receptive fields are composed of two parts. Light in the center of the receptive field stimulates the ganglion cell, while light in the surrounding part inhibits the cell. These are called on-center fields. Other ganglion cells have off-center fields which reverse the role of the center and the surround. Together, the on-center and off-center regions are called center-surround

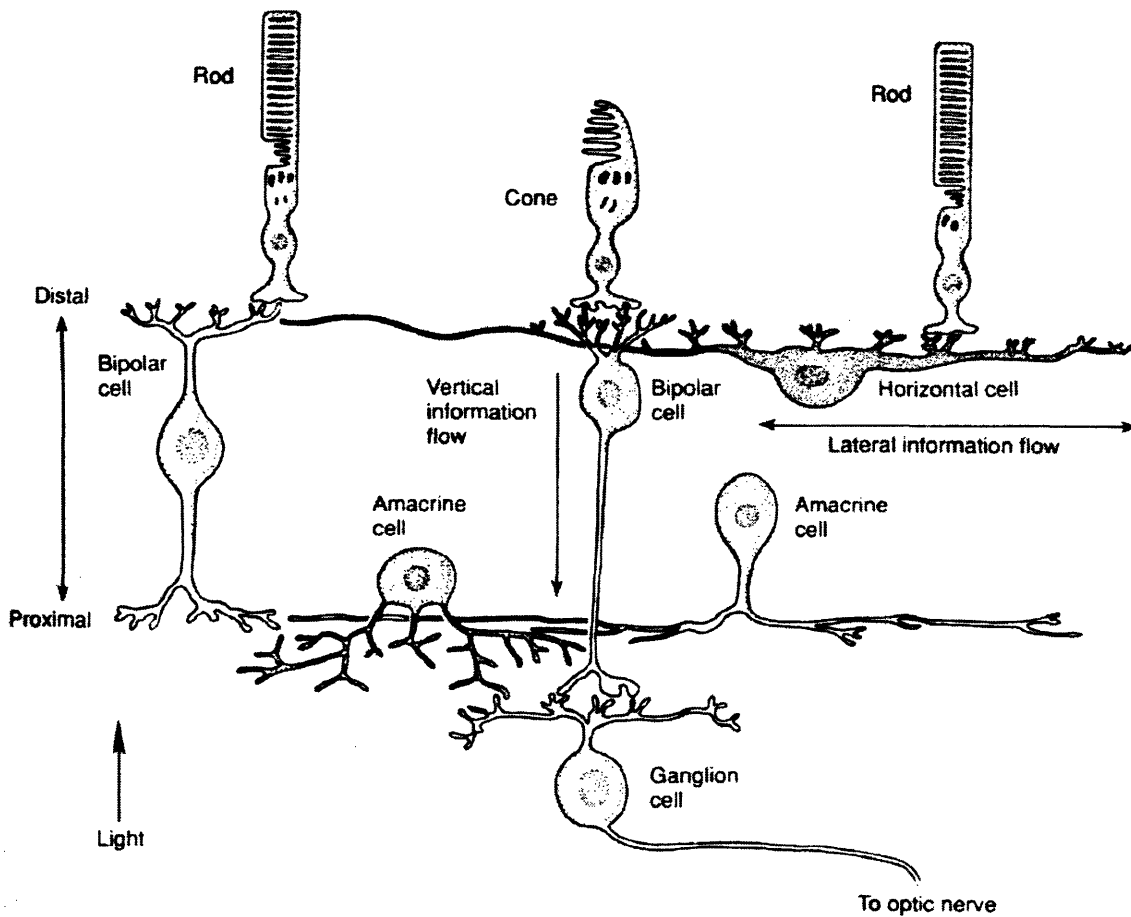


Figure 1-1: Schematic drawing of the retina showing photoreceptors, horizontal cells, bipolar cells, amacrine cells, and ganglion cells. Information flows vertically from the photoreceptors, to the bipolar cells, then to the ganglion cells. It is carried laterally by the horizontal cells and amacrine cells. Figure reproduced with permission from *Principles of Neural Science* by Eric Kandel et. al.[1]

fields.[6, 9]

The photoreceptors form the first of many retinotopic maps in the visual system. A retinotopic map is an array of cells organized topographically according to their receptive fields. The photoreceptors which simply transduce the light that falls on them are obviously ordered by the position of their receptive field. The ganglion cells also form a retinotopic map, which again is unsurprising as each responds to nearby photoreceptors. Other retinotopic maps appear in the brain far removed from the eyes. These cells are still organized according to the position of their retinal field, and form a picture of what stimulates the retina. In some areas the image is heavily processed and distorted, but it is still organized topographically as a picture.

The horizontal and amacrine cells mix information from nearby photoreceptors to create center-surround fields in the ganglion cells. This processing serves to sharpen the image that appears on the retina, highlighting lines and edges while reducing the response to diffuse light. The ganglion cells then carry the information away from the eyes.

### **1.1.3 Optic Nerves and the Lateral Geniculate Nucleus**

The axons from the ganglion cells leave the retina and terminate in the thalamus. In higher mammals, on the order of one million of these axons form the optic nerves leaving each eye. The optical nerves cross and mix in the optic chiasm before proceeding to the right and left sides of the thalamus. All the information from the right half of the visual field goes to left half the thalamus, and vice versa. Such segregation necessitates the mixing of fibers from the two eyes, see Fig. (1-2), as each retinal image contains information from both sides of the visual field.

Upon reaching the thalamus, the majority of the nerve fibers terminate in the lateral geniculate nucleus. A small number terminate in the pretectum, which controls pupil reflexes, and a small number terminate in the superior colliculus, which controls high speed eye movements (saccades). Only the lateral geniculate nucleus (LGN) connects to higher areas responsible for perception.

Each LGN receives input from one half the visual field. Within the LGN, the

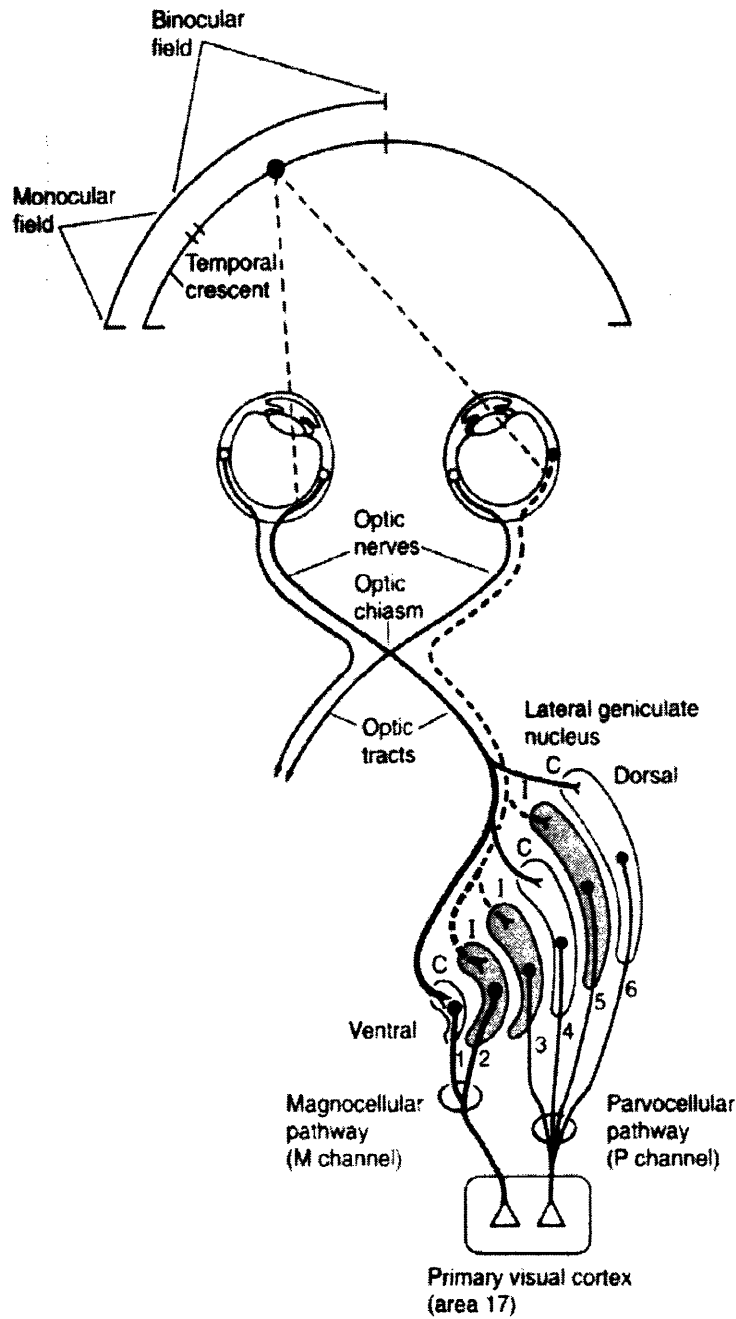


Figure 1-2: Schematic drawing of the visual system from the eyes to the primary visual cortex. Fibers from the right side of each retina lead to different layers in the right lateral geniculate nucleus (LGN). A small number terminate in the pretectum and superior colliculus. Fibers from the right LGN travel to the right primary visual cortex, still segregated by the eye to which they respond. They terminate in layer IVc of the primary visual cortex. A parallel system exists on the left half of the brain, but it is not shown. Figure reproduced with permission from *Principles of Neural Science* by Eric Kandel et. al.[1]

information is further segregated by eye. Three layers within the LGN respond to the right eye and three layers respond to the left eye. The exact number of layers varies with the species, but the segregation is common to all mammals of interest. Most cells within the LGN have axons which leave the thalamus. Thus, there is only a single synapse of processing within the LGN. It is not surprising that the output cells of the LGN show the same center-surround fields that retinal ganglion cells exhibit.[10]

The LGN maintains a retinotopic representation of the visual field. Actually, the LGN contains six retinotopic maps, one in each of its six layers. These six images are aligned. Passing perpendicularly through the six layers, one finds receptive fields located in the same area of the visual fields but switching eyes each layer. The function of the LGN is not well understood. The information about the visual field appears to leave the LGN without further processing. Furthermore, most of the input to the LGN comes not from the retina, but from higher visual areas. The role of this feedback is not known.

#### **1.1.4 Primary Visual Cortex**

The axons from the LGN enter the cortex and terminate in the primary visual cortex (V1), also called the striate cortex or Brodmann's area 17. The primary visual cortex is located in the occipital lobe, the back of the brain. (Oddly, this is as far from the eyes as possible.) The visual cortex is composed of a thin layer of cells between the pial surface, an outer covering on the brain, and the white matter, dense bundles of nerve fibers in the interior of the brain. In the monkey, V1 is roughly 2 mm thick, and if laid flat covers about 13 cm<sup>2</sup>. However, as V1 is folded over itself several times, it require much less space. The portion of V1 on the outer surface of the brain is called the operculum. It is bordered on three sides by area V2. On the fourth side it bends into the calcarine fissure and folds under itself. On the roof of the calcarine fissure it forms a triangle with one side connected back to the operculum and the other two folding under once again.

When discussing V1, we shall refer to the thin (2 mm) dimension as the vertical direction, and to other two dimensions as the horizontal directions. In humans and

monkeys, V1 is organized into 6 layers stacked in the vertical direction. The layers are labeled 1 through 6 with the outer layer labeled 1. Layer 4 is further subdivided into layers 4A, 4B, 4C $\alpha$ , and 4C $\beta$ . The layers were first identified by studying differences in cell and fiber densities.

The fibers from the LGN terminate primarily in layers 4C $\alpha$  and 4C $\beta$ . However, a few fibers terminate in almost every layer. Layers 3 and 4B project fibers to higher cortical areas outside V1, while layers 5 and 6 project back to the LGN and other subcortical areas. Unlike the LGN which has only one synapse of processing, the primary visual cortex has 3-4 synapses of processing connecting the input from the LGN to the output. Cells in V1 typically have arbors which receive input from neighboring cells within 1-2 mm. This processing results in cells which respond to more complicated features than the center-surround fields found in the retina and LGN. However, the cells are still generally organized to form a retinotopic map like the LGN. Modeling the physiological response of V1, which is discussed in detail separately in Sec. (1.2), is main goal of this work.

### 1.1.5 Higher Cortical Areas

The primary visual cortex is only the first of many visual areas as shown in Fig. (1-3). Our understanding of the function of the higher areas is very limited: mostly based on clinical studies of human patients with localized damage to areas of the cortex. Experimental studies on animals are difficult, although some have been performed, as the higher areas are believed to respond to complex and possibly situation dependent stimuli.

Two parallel pathways for information processing exist in the cortex. One pathway for motion (where), and one for color and form (what). Both pathways are dependent on information from the primary visual cortex. Axons leaving layers 3 and 4B of the primary visual cortex connect directly to many other areas: V2, V3, V4, V5, and the middle temporal area (MT) among others. No higher area receives direct input from the LGN or retina, so that all the information eventually used for perception must pass through V1. (This is true in primates, but some other mammals have direct

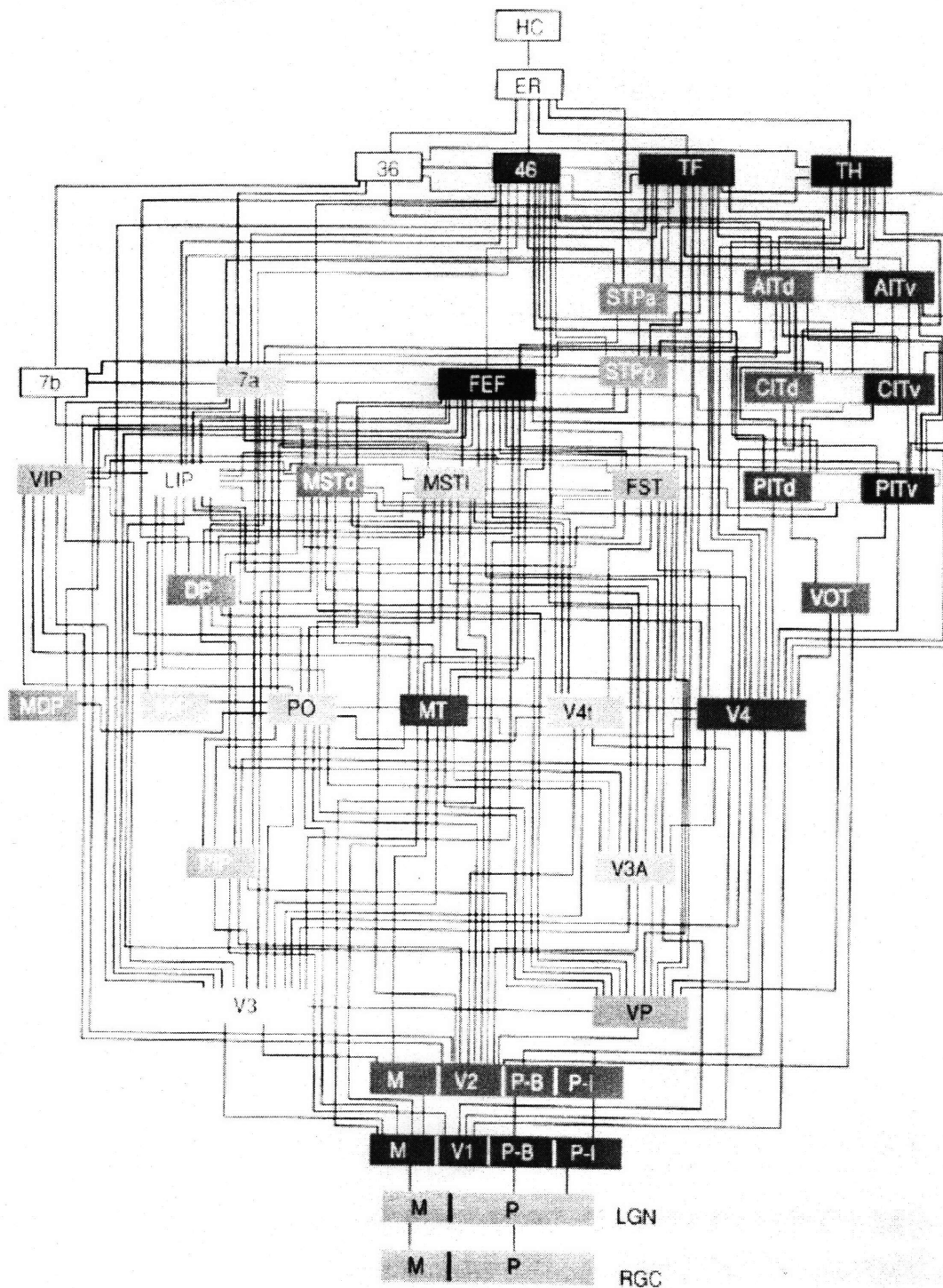


Figure 1-3: The organization of 32 visual areas as suggested by Felleman and Van Essen. Figure reproduced with permission from "Distributed Hierarchical Processing in the Primate Cerebral Cortex" appearing in *Cerebral Cortex*. [2]



connections from the LGN to higher areas.)

Segregation of information for these two pathways may start as early as the retina. Ganglion cells are divided into two classes M and P. The M ganglion cells connect only to the two magnocellular layers in the LGN, while the P ganglion cells connect only to the four parvocellular layers of the LGN. Further, the magnocellular layers of the LGN connect to layer 4C $\alpha$  of the primary visual cortex, while the parvocellular layers connect to 4C $\beta$ . It has been proposed that the segregation continues into layer V2 and beyond. The magnocellular system responds to motion and spatial relationships. Cells within it respond poorly to color differences. Lesions in this area frequently lead to the inability to track moving objects. The parvocellular system responds well to color and appears to be necessary for the recognition of objects. It is unclear how complete the segregation between the two paths is, and many important functions appear in both of the paths.[1]

## 1.2 Physiology of the Primary Visual Cortex

Our goal is to model the development of the functional architecture of the primary visual cortex. This functional architecture is a set of response properties, and is distinct from the underlying physical structure (anatomy) that was described in the previous section. This section describes the physiology that we will be directly modeling.

After a brief overview of the modern experimental methods used to study physiology, we shall describe ocular dominance and orientation selectivity, the two major physiological responses detected in V1. We conclude with a summary of these properties for use in developing and evaluating models.

### 1.2.1 Experimental Methods

Our current understanding of the functional structure of area V1 comes from a long series of experiments conducted during the past thirty years. The overall picture has expanded with the development of new experimental techniques to probe different facets of the cortex. What we know about the primary visual cortex is strongly

influenced by what these techniques can detect. It is therefore worthwhile to take a brief look at them.

### **Microelectrode Recordings**

One of the classic method for studying the physiology of the brain is the use of microelectrodes.[10, 11, 8] This method requires exposing the brain of the subject and inserting conducting electrodes into V1. The electrodes have an insulating coating except for a small area at the tip. The change in voltage associated with individual action potentials is then recorded while the subject views different stimuli. To ensure that the retinal image is not moving relative to the visual field, where the stimulus appears, the subject's eye muscles frequently are paralyzed.

Much of what we know about the cortex comes from microelectrode recordings, which offer many advantages: The full response of the cell, including the exact timing of spikes, is available. Recordings from a single location can be made while the subject views a number of stimuli. In principle, any number of stimuli may be used, and points arbitrarily close together may be studied. In practice, however, microelectrode recordings are made very slowly. One of the pioneers in the field, D. H. Hubel, noted that attacking "such a three-dimensional problem with a one-dimensional weapon is a dismaying exercise in tedium, like trying to cut the back lawn with a pair of nail scissors." [10]

### **Nauta Degeneration Methods**

When the cell bodies of neurons are destroyed, the axons connected to those bodies begin to degenerate. These degenerating axons can be marked by staining slices of the cortex. Thus, by making selective lesions, the connectivity of neurons can be studied. Although this method directly studies the anatomy (physical connections) rather than the actual response of the neurons, it is still very useful for determining the basic function of different sections. The original method was developed in the 1950's by Nauta and others and was applied to the visual cortex by Hubel and Wiesel in the 1970's.[12, 13, 14] By lesioning the LGN, they were able to find where the input

to V1 occurs.

Terminal degeneration studies allow much larger sections of V1 to be studied than are easily accessible by microelectrode penetrations. In a single experiment, the entire cortex can be sliced and stained. However, this method does not directly measure the functional properties of cells, but rather their connectivity.

### **LeVay's Reduced Silver Stain**

Silver stains have long been used to study the density and size of cells in V1 as well as the cortex in general. The six layers which compose V1 are easily detected with a reduced silver stain of a vertical slice of V1. In 1975, LeVay discovered that staining a horizontal slice of V1 revealed a pattern of dark bands separated by narrow light bands.[3] In LeVay's method, silver stains most large and medium nerve fibers but few cell bodies. Thus, the light bands are breaks in the generally high connectivity.

Like the Nauta degeneration method, this approach studies anatomy rather than cell response. In some cases, like ocular dominance, it can be used to find the boundaries of a region whose functionality was previously determined by microelectrode penetrations. However, it also suffers from the same inflexibility as terminal degeneration. It can find functional boundaries only when they coincide with density fluctuations.

### **Autoradiographic Injection**

Certain radioactive tracers deposited near a neuron's cell body are picked by the cell and carried down the axon. Lasnik and others used this property to develop another method to trace the axons and connectivity of cells.[15] After radioactive materials are injected at one point, the cortex is sliced and each slice studied for emissions. Shortly after this method was developed, Grafstock refined it so that the tracers could pass through a synapse.[16] In the mid 1970's Wiesel and Hubel used this refined method to trace connectivity from the eye to V1, passing through the single synapse in the LGN.[17]

Like the Nauta degradation technique, the autoradiographic method studies connectivity. Thus, it has many of the same strengths and weaknesses. Autoradiographic methods, however, may be used in circumstances where making lesions is difficult or undesired.

### **[<sup>14</sup>C]2-deoxyglucose Metabolization**

Radioactive tracers deposited in blood sugar are available to all cells throughout the body. This would not be useful for study, except that neurons take up increased amounts of blood sugar with increased activity. Sokoloff and others developed a method to measure neuronal activity by studying the effects of [<sup>14</sup>C]2-deoxyglucose metabolization.[18] After an injection of [<sup>14</sup>C]2-deoxyglucose, the animal is exposed to a particular stimulus for about an hour. (As with microelectrodes, the eyes muscles are paralyzed to fix the retinal image to the visual field.) Then the animal is killed and the cortex sectioned and studied for radioactive emissions. In the mid 1970's this method was applied to the primary visual cortex by Kennedy and others.[19, 11] Unlike other methods developed after microelectrodes, this method directly measures neuronal activity. The response across the entire visual cortex can be measured to any single stimulus.

The [<sup>14</sup>C]2-deoxyglucose metabolization method is complimentary to microelectrode penetrations. Microelectrodes allow the response of a single point to many different stimuli to be studied, while [<sup>14</sup>C]2-deoxyglucose metabolization allows the response of the entire cortex to a single stimuli to be studied. Since the animal must be killed to study the results, further tests on the same animal are impossible. Still it allows the response of the entire cortex to be mapped, a practical impossibility with microelectrodes.

### **Optical Imaging**

Recently, a significant advance was made with the development of voltage-sensitive dyes. These dyes are injected into the cortex in vivo, and change optical properties depending on the electrical potential of nearby cells. Thus, they can be used to

measure the rate of action potentials in V1. This was done originally by Cohen and others in the early 1970's and repeated by Orbach and others in the mid 1980's.[20, 21] The animal's cortex is exposed and stained with voltage-sensitive dyes. Any point on the surface can be studied with photo diodes while the animal views any desired stimulus. As averaging over time is necessary to reduce noise levels, information about individual action potentials is lost. The method was significantly improved by Blasdel and Salama, who in the mid 1980's started using a video camera and digitizer to image the entire cortex at once.[22]

A related method has been developed that relies on intrinsic optical properties.[23] Active neurons cause changes in the surrounding blood volume, oxygen saturation level in hemoglobin, and ion and water flow rates. All three of these effects change the optical properties of the cortex and can be optically imaged just as voltage-sensitive dyes are imaged. Optical imaging of intrinsic signals has much less time resolution than imaging voltage sensitive dyes, but most experiments on the primary visual cortex are carried over time intervals much longer than the resolution of either method. Imaging intrinsic properties removes the need for applying a voltage sensitive dye which may cause photodynamic damage, and limit the duration of study on an animal.[24]

Optical imaging combines the advantages of both microelectrodes and [ $^{14}\text{C}$ ]2-deoxyglucose metabolism. Like [ $^{14}\text{C}$ ]2-deoxyglucose metabolism, the entire V1 can be studied at once, while like microelectrode recordings, multiple stimuli can be used. This is particularly important in detecting regions that generically respond to any stimuli. As such regions appear in all [ $^{14}\text{C}$ ]2-deoxyglucose studies, it is impossible to know if a responding cell prefers the given stimulus, or responds generically to anything. This method cannot, however, be used to study the vertical structure of the cortex, only the surface layers can be optically imaged. Furthermore, the optical properties recorded are significantly removed from the actual rate of action potentials in spikes per second.

This last point is worth further discussion. The process that leads from the actual neural activity to the number eventually called orientation selectivity or ocular dom-

inance is quite complicated.[25] First the neural activity stimulates a color change in the dye by a process that is not well understood, making it impossible to determine the neural activity given the dye color. The dye is then imaged and digitized, then averaged over both time and space, normalized spatially, combined with data for orthogonal orientations, normalized again, and (in the case of orientation) combined as vectors and subjected to a final normalization. Therefore, the distribution of measured response strengths is very hard to interpret.

It is currently not possible to record from the same animal during different periods of development. Extensive studies can be done with a single animal, but only over the course of hours or days. To study development, a cohort of hopefully similar animals is studied using a different one at each stage. The technical problems preventing prolonged studies of a single animal may soon be overcome.

### **Functional Magnetic Resonance Imaging and Positron Emission Tomography**

Functional magnetic resonance imaging (fMRI) and positron emission tomography (PET) have greatly improved our understanding of the brain. These two techniques rely on the same signal source as optical imaging, so it is tempting to consider applying them to the study of the primary visual cortex. Unfortunately, these techniques currently have a resolution which is an order of magnitude worse than optical imaging.[24] If the resolution of fMRI and PET is improved enough to map the fine structure of visual cortex, they would provide a greatly less invasive method of study. In addition, fMRI and PET would allow the study of deeper layers of the visual cortex, which cannot be optically imaged.

#### **1.2.2 Ocular Dominance**

The primary visual cortex is the first place where input from both eyes is combined. (In the LGN information is strictly segregated by eye.) It is, therefore, interesting to study ocular dominance, i.e. which eye elicits a stronger response from a given site.

In its simplest form, ocular dominance can be considered as a binary field, simply indicating one eye or the other. A better representation is by a real number whose sign indicates which eye dominates, while its magnitude indicates the strength of the dominance. An ocular dominance value of 0 then indicates that a location responds similarly to both eyes. (Both cases of a strong response to all stimuli, and no response to any stimulus are assigned an ocular dominance of zero.)

Early work with microelectrodes revealed that the primary visual cortex is organized into vertical columns.[10, 8] All cells in a given vertical column tend to respond to the same area of the retinal field, and possess the same ocular dominance and other properties. Due to their similarity to features in the somatosensory cortex found by Mountcastle, these features are called ocular dominance *columns*. [26] Cells in layer 4 are predominately monocular, responding almost exclusively to one eye or the other. Over half the cells in layers 2, 3, 5, and 6 are binocular, but show a preference for the eye that dominates layer 4 in that particular column. Nauta degeneration methods and autoradiographic eye injection reveal the anatomical basis for the monocularity in layer 4, in that the fibers from the two eyes are still completely segregated.

The ocular dominance columns are organized into ocular dominance bands, as shown in Fig. (1-4). In the monkey, these bands have a relatively constant width of 0.4 to 0.5 mm. There is a small amount fluctuation in the widths within an given animal and between animals. However, no systematic changes in width occur between different parts of V1. The pattern has been observed by all the methods discussed in the previous section.[14, 10, 3, 17, 19, 25] The exact pattern of bands varies with the particular animal under study, but many features are common to all observations. All the bands tend to intersect the boundary of area V1 at right angles, and all subjects have bands that run in the same general directions. In the operculum, bands tend to run from the edges of V1 toward the calcarine fissure. Once inside the fissure the bands turn sharply as they run into bands coming from the perpendicular direction.

The bands meander, occasionally branching and terminating. We shall refer to the internal order of the patterns as their persistence. Some aspects of persistence are easy to quantify. For example, the number of branches can be counted. Fig. (1-4) has 190

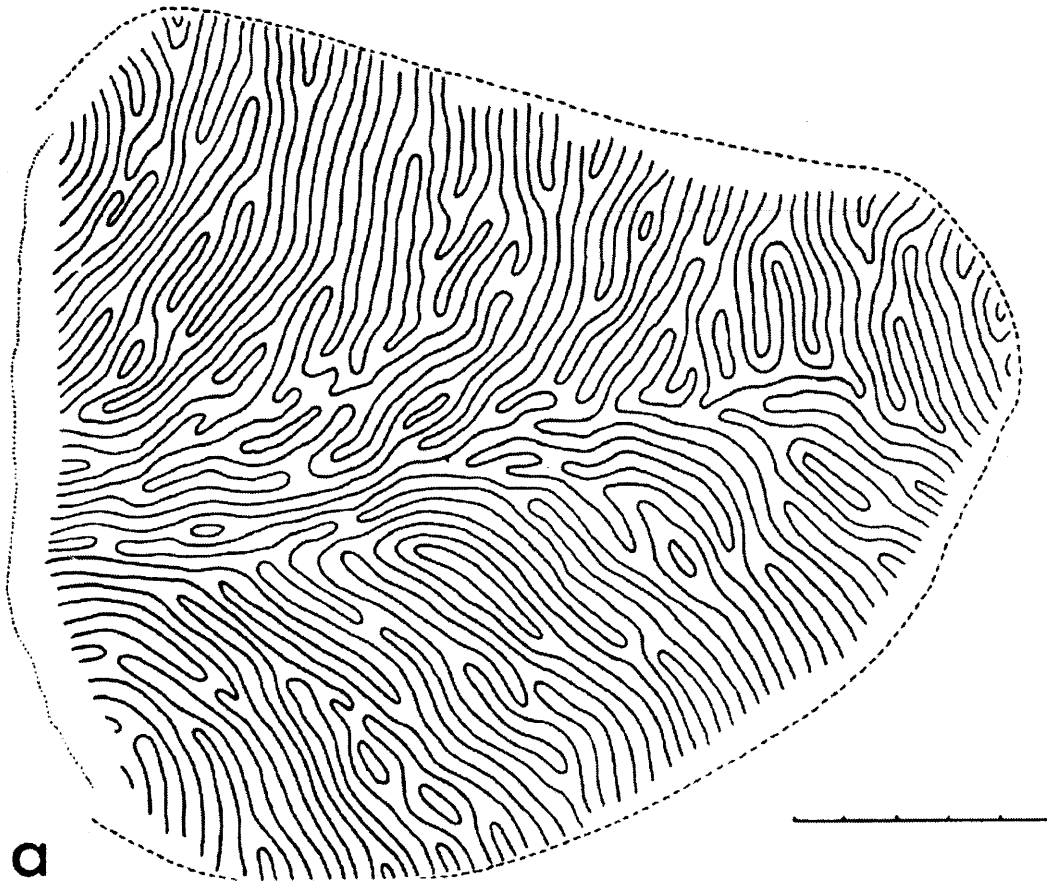
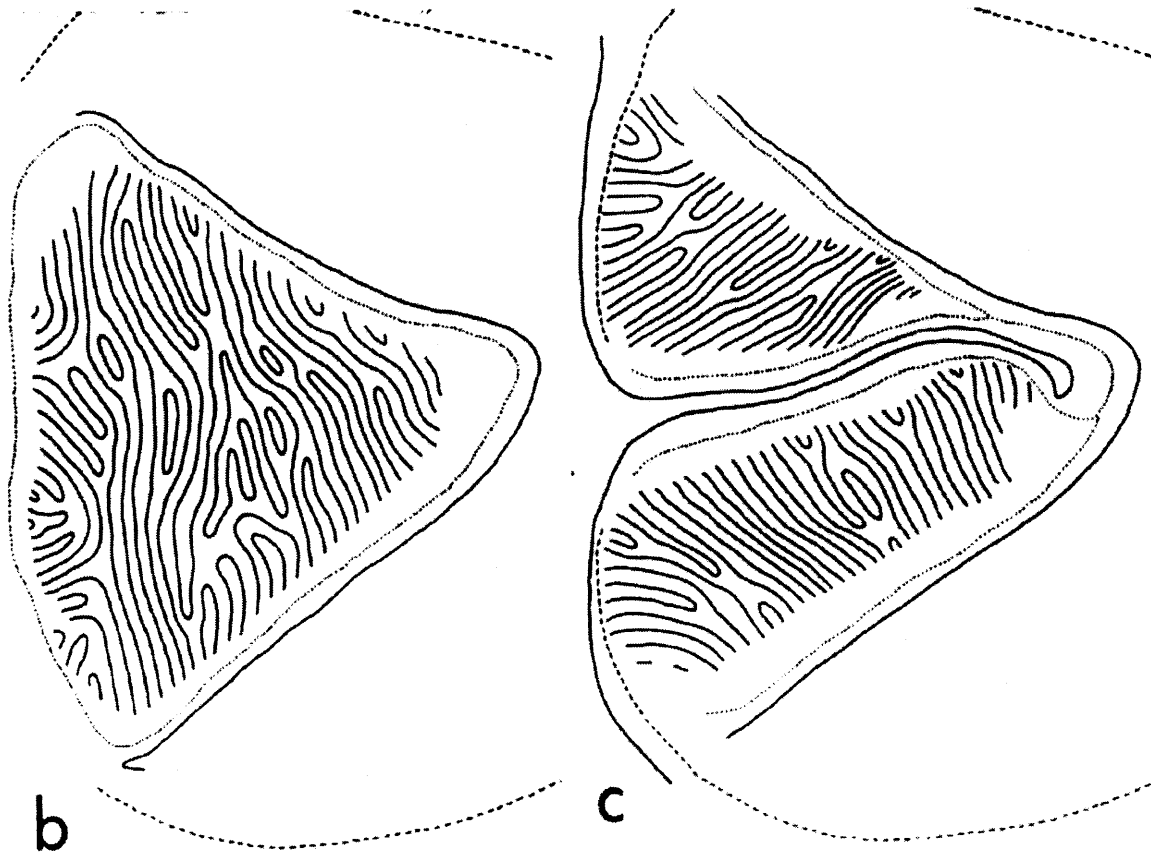


Figure 1-4: Reconstruction of ocular dominance bands in the monkey primary visual cortex based on data from LeVay's reduced silver stain. (Scale shows mm.) In (a) the operculum is shown, in (b) the roof of calcarine fissure, and in (c) the leaves joining the roof to the stem. The dashed line is the border between areas V1 and V2. The dotted line shows places where the cortex is folded under itself. The dark lines in the figure itself are the domain walls of the ocular dominance bands. Note that adjacent bands never join. Figure reprinted from "The Pattern of Ocular Dominance Columns in Macaque Visual Cortex Revealed by a Reduced Silver Stain", by Simon LeVay et. al. appearing in the *Journal of Comparative Neurology*. Copyright ©Wiley-Liss, Inc.. Reprinted by permission by Wiley-Liss, Inc., a subsidiary of John Wiley & Sons, Inc.[3]





branches giving a density of roughly 0.6 branch points per  $\text{mm}^2$  or 0.04 per  $(\text{band})^2$  (the width of the band squared). This latter measure is more useful as the brain undergoes significant shrinkage during LeVay's preparation. The number of branch points, is the same as the number of end points, where a band dead ends, except for corrections at the boundaries. Measuring the persistence on longer scales, i.e. the straightness of the bands, is more difficult. Typically, when comparing different results or simulations, we are forced to rely on the qualitative appearance.

The bands are separated by "domain walls", narrow intervals which respond to both eyes similarly. The form of the domain walls varies with the layer in the cortex. In layer 4 the domain walls are very sharp. Microelectrode penetrations generally fail to record any cells with significant binocular behavior in layer 4, although there is small reduction in ocular dominance extending perhaps 0.1 mm to each side of a domain wall.[10] The LeVay technique reveals an area of reduced fiber density at the domain walls. This area has 1/6 the width of the bands but doesn't necessarily

indicate reduced ocular dominance. In layers 2, 3, 5, and 6, the domain walls are very gradual. Cells with zero ocular dominance occur near the domain walls and the level of ocular dominance rises slowly to a maximum at the center of the band.[10, 25]

A pattern of ocular dominance bands superimposed on a retinotopic map presents interesting organizational issues. This form of organization seems to suggest that at some points in the visual field the brain processes mainly information from the right eye, while at other nearby points the information comes mainly from the left eye. This would indeed be the case if the retinotopic map and the ocular dominance columns were completely independent. However, the retinotopic map is strongly effected by the ocular dominance columns. Discontinuities in the retinotopic map occur on ocular dominance domain walls. Each location in the retinal field is represented twice once in a location of each ocular dominance.[10]

Six weeks before birth, there are no anatomical signs of ocular dominance in the monkey.[27] Physiological experiments are impossible before birth, but layer 4C can be seen to be fully enervated by each eye. At one week before birth, periodic fluctuations can be seen in the density of fibers in layer 4C, but the layer is still fully enervated by each eye. By six weeks after birth, full segregation is complete.[28] This development takes place regardless of visual stimuli, i.e. even if the animal is subjected to complete binocular deprivation. If, however, the animal is subjected to monocular deprivation for a significant period during the first two months after birth, the open eye is favored in ocular dominance. In a normal healthy animal, the fraction of V1 covered by ocular dominance bands for each eye is almost identical. However, if an animal is deprived of the use of one eye during critical postnatal periods, the bands corresponding to the open eye become wider than those of the deprived eye. This effect is permanent unless the monocular deprivation is reversed while still in the critical period. After about two postnatal months, monocular deprivation has no noticeable effect on ocular dominance.

During the first few months after birth, the cortex grows by at least 16% in the monkey.[29] All the growth occurs in a direction perpendicular to the ocular dominance bands.[30] The number of columns remains fixed, but their width increases

by about 16%.

### 1.2.3 Orientation Preference and Selectivity

The primary visual cortex is the first place in the visual system where cells have complex receptive fields, and not simply center-surround responses. In particular, many cells in V1 respond strongly to line segments of a particular orientation. The orientation that most strongly stimulates a cell is called its orientation preference.

Characterizing orientation preference is not as simple as ocular dominance. To fully characterize a cell in V1 requires giving its response to all possible patterns of light. (Even that gives only its static response, neglecting the effects of motion.) This is much too large a space to examine. Instead, we characterize a cell by looking at its response to orientation. In most cases, this means presenting an array of oriented bars. Thus, response is reduced to a single function of angle for each location in V1. This still leaves the choice of what function to measure: firing rate, oxygen usage, voltage as determined by optical dyes, or some other property. Luckily, the response measured in terms of any of these properties shows some key similarities. First, due to simple geometrical constraints, it is periodic over 180 degrees. Second, for most cells, it has a single pronounced peak. The width of the peak doesn't fluctuate significantly from one location to the next.[31] This allows the response to be characterized by a single angle, the orientation preference. Although the width of the peak remains relatively constant, the height of the peak does not. This height is a measure of the strength of the preference called orientation selectivity.

To determine orientation preference and selectivity from optical imaging the following procedure is typically used. The response of a given location is measured for several orientations (typically 4 to 12). The response for each direction ( $\theta$ ) is multiplied by a unit vector pointing in the direction  $2\theta$ . These vectors are then summed. The angle of the resultant is twice the angle of preference and the magnitude of the resultant is a measure of orientation selectivity. Note that cells that respond strongly to all orientations have a small selectivity, even though they may have a large response. The preference and selectivity can be found from  $A_2$ , the second component

of the complex Fourier transform,

$$A_2 = \frac{1}{N} \sum_{n=1}^N e^{i2\theta_n} \mathcal{R}(\theta_n) \quad (1.1)$$

where  $\{\theta_n\}$  are the angles recorded from, and  $\mathcal{R}(\theta)$  is the response at angle  $\theta$ . The complex angle of  $A_2$  gives the preference, while its magnitude,  $|A_2|$ , gives the selectivity.

A second method has been developed to characterize the orientation response using electrode penetrations.[32, 33] This method finds orientation preference similarly, but measures selectivity with the orientation selectivity index (OSI). The OSI value is given by,

$$OSI = 100 \times \frac{|A_2|}{|A_2| + A_0}, \quad (1.2)$$

where  $A_0$  is the zero Fourier component.

Like ocular dominance, orientation selectivity is organized into vertical columns. The same orientation preference appears in layers 2, 3, 5, and 6, at a given horizontal position. Cells in layer 4 do not show orientation preference, but instead still respond to center-surround receptive fields. Orientation columns have been found by both microelectrode penetrations and optical imaging.[11, 22] [ $^{14}\text{C}$ ]2-deoxyglucose metabolism can reveal the response of every location to a particular orientation but not the preferred orientation at a particular location.

Microelectrodes reveal little about the organization of orientation columns but optical imaging reveals a complicated pattern of response, as in Fig. (1-5). The most prominent features are point singularities, where all orientations meet at a single point, called “pinwheels”. Two varieties of pinwheels (positive and negative) exist with the orientations rotating about them in opposite directions. The number of positive and negative singularities are almost nearly the same. The total density of singularities in the monkey is reported as  $8.1 \text{ mm}^{-2}$ . [34] Experimentalists have noted three other features of interest: linear zones, fractures, and saddle points. Linear zones are regions with a diameter of 0.5-1.0 mm where the orientation preference changes slowly in one horizontal direction and remains constant in the perpendicular one. They appear typically in regions away from singularities and locally look like a

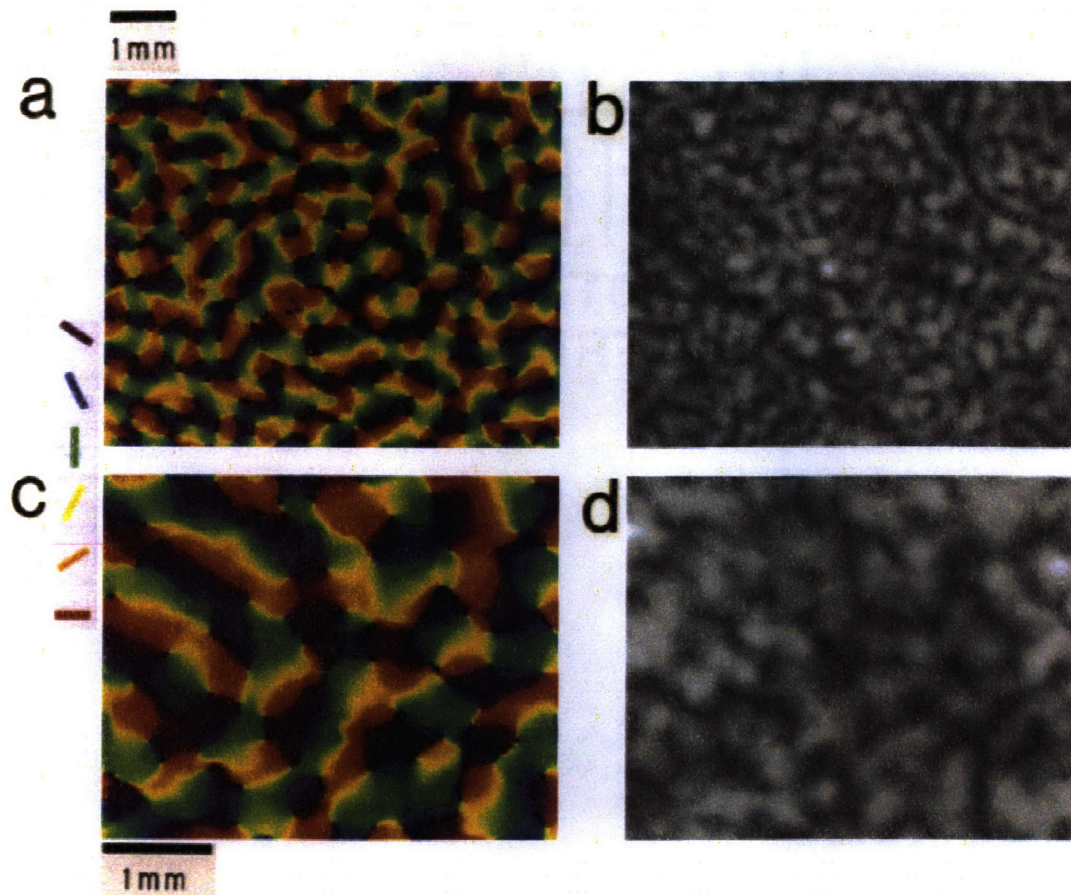


Figure 1-5: Two pairs of orientation and selectivity patterns. (a, c) Orientation preference and (b, d) selectivity in the monkey determined from optical imaging. In (a, c) different colors encode different angular preference as shown in the key on the left. In (b, d) lighter areas are more selective than darker ones. Figure reproduced with permission from “Orientation Selectivity, Preference, and Continuity in the Monkey Striate Cortex” by Gary Blasdel appearing in *The Journal of Neuroscience*.<sup>[4]</sup>

series of parallel orientation bands. Fractures are one dimensional singularities where orientation preference rapidly changes. They tend to run between two pinwheels, connecting them. Finally, saddle points are small areas where orientation preference remains constant. Saddle points are bounded by four singularities that create the region of constant preference.

The distribution of selectivities has not been studied as extensively as other properties, but it appears to be wide and not centered around the origin. In the ferret, the distribution of selectivity appears to be uniform over a wide range of OSI values

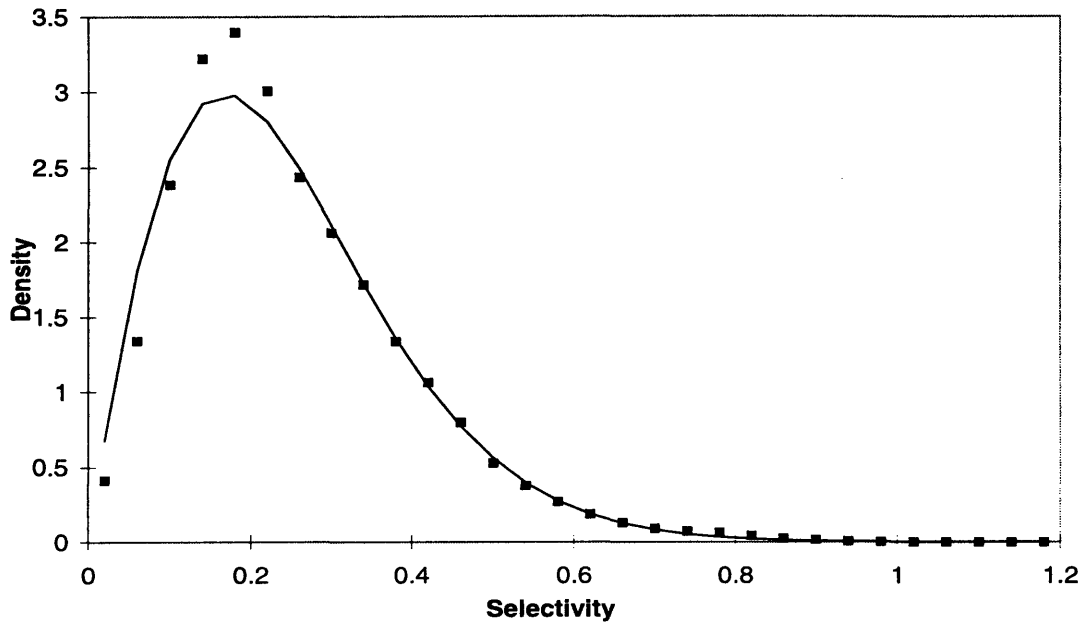


Figure 1-6: The distribution of selectivity in the visual cortex. The squares indicated data for the ferret provided by Mriganka Sur's group at MIT, while the line is a least squares fit to the form  $r \exp(-\alpha r^2)$ . In this case  $\alpha = -14.3$ .

from 15 to 65.[33] Small tails extend to lower and higher values. Our own analysis of optical imaging data in the ferret provided by Mriganka Sur shows a distribution well fitted by a form  $r \exp(-\alpha r^2)$ , as shown in Fig. (1-6).[31] Interpretation of this data is, however, complicated by the rather convoluted definition of selectivity, as discussed in Sec. (1.2.1).

Orientation columns have been observed shortly after birth in the monkey.[35] At three and a half weeks, when optical imaging can be performed, a full pattern comparable to adults is visible. The density of pinwheels remains roughly constant as the monkey matures, despite the fact that the cortex grows by about 16%.[34] In order to maintain this density more singularities must be added either by entry through the boundaries or by creation of positive and negative pairs.

### 1.2.4 Coupling between Ocular Dominance and Orientation

From the first detection of orientation and ocular dominance columns, coupling between the two has been of great interest. Initially, data only presented opportunity for conjecture.[14] Optical imaging has allowed the collection of enough data to study this issue in depth. The fractures and singularities in the orientation columns occur more frequently in the center of ocular dominance bands, rather than near domain walls.[22, 4] This alignment causes lines of isorientation to tend to intersect ocular dominance domain walls at right angles. In linear zones, lines of isorientation are roughly 3 to 4 times more likely to intersect domain walls at the nearly perpendicular (72-90 degrees) rather than nearly parallel (0-18 degrees).[34] In all other regions, except those near singularities, the tendency to cross perpendicularly is still present, although reduced in degree.

Fourier transforms of orientation and ocular dominance maps reveal a similar tendency toward orthogonality. Two dimensional Fourier transforms of ocular dominance fields reveal two clusters of modes displaced at equal distances (roughly  $1.22 \text{ mm}^{-1}$ ) from the origin. The line running through the two clusters is aligned to the axis of repetition for ocular dominance. (As only a small region of V1, several  $\text{mm}^2$ , is transformed, the bands have a locally preferred direction.) Two dimensional Fourier transforms of orientation preferences in the same area reveal a nearly circular ellipse with a diameter near  $1.47 \text{ mm}^{-1}$ . However, the ellipse does have a detectable major axis, which tends to be perpendicular to the corresponding axis of repetition for ocular dominance.[34]

The assigned magnitudes of both ocular dominance and orientation selectivity have arbitrary units, with no absolute meaning. Still, it is possible to study the ratio of average ocular dominance magnitude to orientation selectivity. This ratio increases with age. At three and one half weeks after birth it has been recorded as 0.92 but in mature animals it is roughly 1.36.[30] Thus, ocular dominance either reaches maturation first, or grows more slowly than orientation in the final stages of maturation.

### 1.2.5 Summary of Characteristic to be Modeled

We have enumerated a large number of properties of the primary visual cortex. It is useful to summarize those that will be of interest when modeling the cortex, and we have listed them in Tbl. (1.1).

There are several features not listed in this table that are frequently discussed in conjunction with cortical maps. These include linear zones, saddle points, and fractures. Linear zones will appear in any pattern of angles, so their presence offers little insight. It may be possible to characterize what fraction of the area is in linear zones, but we believe there are better ways to measure the same effect. Similarly saddle points and fractures appear in almost all fields with pinwheels. Again, we could measure the size of saddle points and the rate of change in fractures, but such characterization involves many arbitrary decisions. A better way may be to study the distribution of singularities (pinwheels), focusing not only on its density, but also on correlations among like singularities and between opposite ones. This approach would describe the same features, but in a much more robust manner.

## 1.3 Previous Models of the Primary Visual Cortex

Since the discovery of ocular dominance and orientation columns in V1, many models of the development of these features have been proposed. All these models attempt to show how a limited number of simple rules or interactions generate the patterns found in the cortex. Most of these models do not attempt to explain how the cortex functions, i.e. how it actually identifies objects, rather they focus on the development of the functional architecture.

The models can be placed into four broad categories: structural models, static filter models, evolving field models, and neural network models. Structural models attempt to identify organizational principles without specifying mechanism for their development. Filter models describe the structure in terms of filtered noise. Field



Table 1.1: Important properties of ocular dominance and orientation to be considered when evaluating and developing models.

<i>Ocular Dominance Bands</i>
<ul style="list-style-type: none"> <li>- Bands of width 0.4 to 0.5 mm</li> <li>- Some random fluctuations in width</li> <li>- Random branching and ending with a density of ends and branches equal to 0.04 per (band)<sup>2</sup></li> <li>- Global pattern resembling that found by LeVay, see Fig. (1-4)</li> <li>- Bands tend to intersect the boundary at right angles</li> <li>- Domain walls are sharp (wide) in layer 4 (other layers)</li> <li>- Cortex grows by 16% perpendicularly to bands</li> <li>- Binocular deprivation has little effect</li> <li>- Monocular deprivation during a critical period narrows suppressed bands</li> </ul>
<i>Orientation Columns</i>
<ul style="list-style-type: none"> <li>- pattern of orientation preference with a pinwheel density of 8.1 mm<sup>-2</sup></li> <li>- both types of pinwheels in equal numbers</li> <li>- pattern of pinwheels shows global disorder</li> <li>- constant pinwheel density during development despite cortex growth by 16%</li> <li>- wide distribution of selectivity</li> <li>- critical period of development from prenatal week 6 to post natal week 6</li> </ul>
<i>Coupling</i>
<ul style="list-style-type: none"> <li>- pinwheels tend to occur in the center of ocular dominance bands</li> </ul>

models assume the existence of ocular dominance and orientation fields, and attempt to show their development from some random initial condition to the observed final state. Finally, neural network models attempt to show explicitly how ocular dominance and orientation preference arise from the center surround cells in the LGN. This choice of categories is somewhat arbitrary. Other authors have chosen different classifications.[36, 37]

### 1.3.1 Structural Models

Structural models were developed shortly after the discovery of orientation preference and ocular dominance. These models used the then limited data to extrapolate general organization principles. Structural models have no mathematical algorithms for ongoing development, and make no claims as to the organization of the cortex before maturation. Despite these limitations, structural models are important to understand, as the progenitors of later attempts. They have had significant impact on the development of models and even on the direction in which experimental work proceeded.

#### Icecube Model

The first structural model was developed by Hubel and Wiesel.[10] After noticing regular bands of ocular dominance, and what appeared to be bands of orientation preference, they proposed the simple organizational structure, depicted in Fig. (1-7). Ocular dominance bands run in one direction while orientation columns form bands in another direction. Despite the appearance of the figure, Hubel and Wiesel did not suggest that orientation and ocular dominance bands crossed at right angles. Nor, did they suggest that the orientation bands were straight. Locally in linear regions, the icecube model is accurate. However, globally it ignores both the pinwheels, and the global disorder obvious in the modern patterns of orientation, as in Fig. (1-5).

The icecube model embodies two organizational principles, continuity and diversity, that have long been believed to be important in V1 functional architecture.[38,

<b>R</b>		<b>L</b>	
<b>R</b>	/	<b>L</b>	/
<b>R</b>	/	<b>L</b>	/
<b>R</b>	/	<b>L</b>	/
<b>R</b>	—	<b>L</b>	—
<b>R</b>	\	<b>L</b>	\
<b>R</b>	\	<b>L</b>	\
<b>R</b>	\	<b>L</b>	\

Figure 1-7: The iccube model developed by Hubel and Wiesel. R and L indicate ocular dominance columns responding to the right and left eye. Regions with a small diagonal line indicate orientation bands. This figure is not meant to imply that ocular dominance bands cross orientation bands orthogonally or that the bands are straight.

39] Continuity reflects the observed fact that nearby cells tend to have similar orientation preference and ocular dominance. This is not true near singularities in orientation preference, but is true over much of V1. Diversity reflects the need to fill feature space as completely as possible, so that all possible combinations of location, ocular dominance, and orientation, are represented. Otherwise some kind of “perceptual scotomata” may result where certain objects can not be seen in certain parts of the visual field.[40] The simple structure of the iccube model ensures both continuity and diversity.

The iccube model led to the development of the concept of a hypercolumn, a complete set of either orientation or ocular dominance columns. Fig. (1-7) shows one of each. The notion of hypercolumns is very appealing as it breaks V1 down into small functional modules. Unfortunately, the cortex does not appear to have any discrete modules. The existence of singularities in orientation preference is not easily reconciled with modules of orientation. Furthermore, all attempts to find anatomical evidence for modules, or to measure their typical size have been unsuccessful.[41]

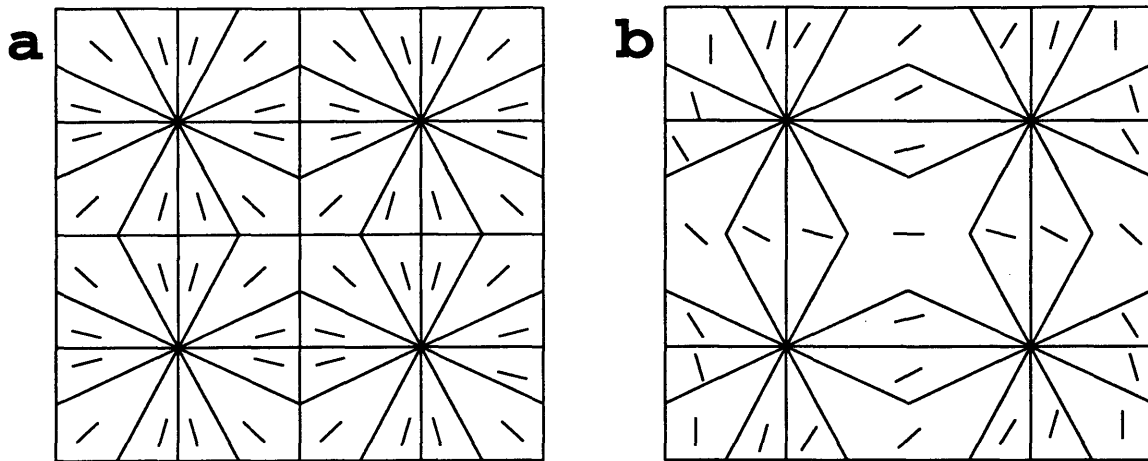


Figure 1-8: (a) The pinwheel model as originally developed by Braitenberg and Braitenberg. The orientation is linked to the isoorientation lines. Singularities with  $+360^\circ$  and  $-180^\circ$  are present. (b) The pinwheel model as modified by Gotz. Orientation is no longer bound to isoorientation lines, and  $\pm 180^\circ$  singularities are present.

### Pinwheel Model

A second structural model, the pinwheel model, incorporates the singularities observed in orientation preference. The original form was suggested by Braitenberg and Braitenberg using only data from microelectrode penetrations.[42] They noted that the observed data for orientation preference were compatible with organizations other than simple parallel bands, as in Fig. (1-8a). While the original pinwheel model required the preferred orientation to be tangential to lines of isoorientation, later refinements removed this constraint as shown in Fig. (1-8b).[43]

The modified version of Fig. 1-8b is qualitatively correct in many ways. It shows linear regions, saddle points, and pinwheels. It incorporates pinwheels of both orientations, and predicts the 1:1 ratio observed between them. However, this simple model does not contain any global disorder. The pattern of pinwheels is perfect and orderly on long scales. The spacing of the pinwheels is constant. Furthermore, this model places too much stress on hypercolumns, and divides the orientation pattern into discrete modules.

### 1.3.2 Static Filter Models

Several models have been developed that use bandpass filtered white noise to generate cortical maps.[44, 45, 46] These models generate patterns by combining simple approximations of the observed Fourier spectra with randomness. As many of the creators of bandpass models emphasize, the procedure is mathematically equivalent to a random source (providing disorder) convoluted with a filter (providing continuity).

Ocular dominance and orientation are modeled by three fields. Two fields are combined to give orientation preference and selectivity, while the third indicates ocular dominance. The fields,  $f_i(\vec{x})$ , are initialized with small random values, either taken from Gaussian white noise centered at zero with some arbitrary variance, or from some other procedure. Each field is then separately convoluted with a bandpass filter,

$$g_i(\vec{x}) = h_i(\vec{x}) * f_i(\vec{x}). \quad (1.3)$$

The passbands are chosen to resemble the Fourier characteristic of the patterns in experiment.[45] For orientation, the filters are annuluses in real space. Grossberg and Olson use a bandpass filter made from the difference of Gaussians[46],

$$h_i(\vec{x}) = \exp\left(-\frac{|\vec{x}|^2}{2s_1^2}\right) - \exp\left(-\frac{|\vec{x}|^2}{2s_2^2}\right). \quad (1.4)$$

For ocular dominance, the filter is typically two clusters evenly offset from the origin. This can be generated by multiplying the above difference of Gaussians filter by a one dimensional exponential, again mimicking the observed Fourier pattern. Orientation preference is given by  $\tan^{-1}(g_1/g_2)$ , while orientation selectivity is given by  $\sqrt{g_1^2 + g_2^2}$ . A third field,  $g_3$ , describes ocular dominance.

This model has the advantage of being computationally very fast. The final state is reached in a single step. There is no need to iterate equations repeatedly, or worry about the effects of discrete time steps. Unfortunately, this means that development is neither observable, nor alterable by changing conditions at some point before maturity. Only the final pattern is available for study.

The ocular dominance patterns generated by these models show parallel wandering and branching bands as seen in the monkey. The average width of bands can be easily adjusted by moving the location of the pass band. The persistence of the bands can be varied by changing the eccentricity of the annulus pass band, while the fluctuation in the width of the bands can be controlled by changing the pass band width. Persistence and width fluctuations do not appear to be completely independent, as increasing the width fluctuations seems to also decrease the persistence.[44]

Other features of ocular dominance are not modeled quite so well. The generated ocular dominance patterns are limited to a single global orientation. This can be alleviated by making the parameters of the filter slowly change with position, but this creates a new problem of modeling the changing parameters. Due to the nature of the model, neither effects of the boundary, nor those of deprivation can be studied easily. They can be incorporated to some extent by modifying the filter parameters near the boundaries, and by incorporating a bias toward one eye in the filter or in the initial conditions. Unfortunately, information on the distribution of selectivity and profiles of the domain walls generated by this model have not been published, so comparison with the observed data is not possible.

These models also generate orientation patterns similar to those observed experimentally. Both types of singularities exist in equal numbers as expected. In addition, linear regions, fractures, and saddle points can all be seen. The density of singularities can be adjusted by varying the diameter of the annulus forming the pass band, although detailed studies of this effect have not been reported. The distribution of selectivity has also not been reported to compare with experimental results.

Grossberg and Olson[46] are able to generate the observed correlations between orientation and ocular dominance by correlating only the initial inputs, but still using independent bandpass filters. Their initial conditions are given by,

$$\begin{aligned}
 f_1(\vec{x}) &= \cos(\alpha(\vec{x})) \cos(\beta(\vec{x})), \\
 f_2(\vec{x}) &= \sin(\alpha(\vec{x})) \cos(\beta(\vec{x})), \\
 f_3(\vec{x}) &= \sin(\beta(\vec{x})),
 \end{aligned}
 \tag{1.5}$$

where  $\alpha(\vec{x})$  and  $\beta(\vec{x})$  are random angles assigned to every point  $\vec{x}$ . These initial conditions explicitly incorporate an inverse relationship between the magnitude of ocular dominance and orientation selectivity,  $|f_{OS}|^2 + |f_{OD}|^2 = 1$ . In this case, pinwheels tend to form in the center of ocular dominance bands and isoorientation lines tend to cross ocular dominance domain walls at right angles. However, these tendencies are not as strong as seen experimentally. The success of this type of model is not surprising, as it starts with the correlation function taken from the experimental data.

### 1.3.3 Evolving Field Models

This class of models treats orientation and ocular dominance as fields, assigning values to each at every point in a two dimensional space. The fields are then updated according to some specified rules which may involve couplings between them. These models are computationally fast, but do require repeated iteration. The number of variables scales linearly with the number of locations modeled. This allows relatively large areas to be studied with a relatively fine scale of discrete points which do not necessarily correspond to individual neurons. Rather, the scale is chosen so that the spacing of points in the mesh is less than the finest feature to be modeled. This is a great advantage, as the two dimensional spacing between cells is on the order of a few microns, while the features of interest vary on the scale of hundreds of microns. The price paid for this computational ease is the loss of information about neural connectivity. These models predict that a certain region will have a particular orientation preference, but they give no clue as to the synaptic wiring that actually causes the cells to respond to that orientation.

Two such models will be described here. The first uses reaction-diffusion equations to update the fields. The second employs dynamics motivated by other pattern formation problems.

## Reaction-Diffusion Model

Reaction-diffusion models of pattern formation date back to the pioneering work of Turing in the 1950's.[47] It has been suggested for some time that reaction-diffusion might play some role in the development of V1:[39] a recent implementation is by Bhaumik and Markan.[48]

Orientation is modeled by a pair of diffusing quantities,  $X$  and  $Y$ . Orientation preference is then given by  $\tan^{-1}(Y/X)$ , while orientation selectivity is given measured by  $X^2 + Y^2$ . Orientation develops according to a simple reaction diffusion equation,

$$\frac{\partial W}{\partial t} = W (\gamma - W^T W) + D \nabla^2 W, \quad (1.6)$$

where,

$$W = \begin{bmatrix} X \\ Y \end{bmatrix}. \quad (1.7)$$

Once the orientation map has reached a desired state, iteration of this equation is suspended, and ocular dominance is modeled. Ocular dominance is represented by a single field,  $Z$ . The magnitude of  $Z$  represents the strength of the dominance and the sign of  $Z$  indicates the preferred eye. Ocular dominance develops according to reaction-diffusion equations coupled to the now static orientation field.

$$\frac{\partial Z}{\partial t} = (1 - W^T W) Z (\Gamma - Z^2) + D \nabla^2 Z. \quad (1.8)$$

Once the ocular dominance map reaches a desired state, its iteration is also stopped.

The reaction diffusion model results in orientation patterns which contains both types of pinwheels in equal ratio. However, the density of pinwheels continues to fall as the pinwheels of opposite circulation annihilate each other. If the simulation is not interrupted, a uniform field without any pinwheels is obtained. The distribution of selectivities is typically much narrower than seen experimentally. It does, however, follow the observed pattern of increasing selectivity with time. The initial distribution is sharply centered around nearly zero selectivity. This sharp peak then moves to



higher values of selectivity.

The model gives regions preferring each eye, but these regions do not form a pattern of stripes as is seen in the monkey. (In mammals other than the monkey, the pattern may not have stripes.) Work has not yet been done to see if this model can reproduce other features desired in a model of ocular dominance. The coupling with the orientation map causes the ocular dominance domain walls to prefer linear regions and isoorientation lines to cross domain walls at right angles. However, the results reported so far are not conclusive.

### Swindale's Model

Swindale has developed a model of the primary visual cortex based on ideas from Hubel and Wiesel, and insights from pattern formation.[39, 49, 50] This model is the most similar to the one we have developed, see Chap. (3). The initial motivation came from Hubel and Wiesel's suggestion of a competition between efferents from the left and right eyes. Swindale also incorporates from work on pattern formation in zebras, feathers, and many species of fish.

An ocular dominance field,  $n(\vec{x})$ , is used to measure of the density of synapses in layer 4 connected to each eye. The density of right eye synapses is  $(1 - n)/2$ , while that of left eye synapses is  $(1 + n)/2$ . Values  $n = \pm 1$  indicate monocular regions: the total density is constant. The density of synapses at each point interacts with the densities in the surrounding area. Up to a distance of  $200 \mu\text{m}$ , synapses from one eye inhibit synapses from the other eye, while at separations of  $200 \mu\text{m}$  to  $600 \mu\text{m}$ , they reinforce growth of synapses from the opposite eye. This is expressed as a convolution in the dynamical equation,

$$\frac{\partial n(\vec{x})}{\partial t} = g_n (n(\vec{x}) * \omega_n + K) (1 - n(\vec{x})^2), \quad (1.9)$$

where  $K$  is zero unless monocular deprivation is taking place, and the kernel of the

convolution is the differences of Gaussians,

$$\omega_n(r) = A_n \exp\left(-\frac{r^2}{d_{n1}}\right) - B_n \exp\left(-\frac{(r-h)^2}{d_{n2}}\right). \quad (1.10)$$

The non-linear factor is included to limit the density of right and left eye efferents to non-negative values. Swindale suggests that long range interaction is mediated by chemicals diffusing through cortex or results from the horizontal synaptic connectivity: “that two synapses are in contact with the same postsynaptic cell, that they belong to the same axon, or that they are driven by the same area of the retina.”[39]

Orientation preference and selectivity are encoded in Swindale’s model as a complex number,  $z = |z|e^{i\phi}$ . The preference is given by  $\phi/2$ , and selectivity by  $|z|$ . The evolution of orientation is controlled by an equation similar to the one for ocular dominance.

$$\frac{\partial z(\vec{x})}{\partial t} = g_z (z(\vec{x}) * \omega_z) (1 - |z|), \quad (1.11)$$

where  $\omega_z$  is a convolution kernel identical in form to  $\omega_n$ , but potentially with different parameters. Swindale later expanded the model to include a coupling between ocular dominance and orientation,

$$\frac{\partial z(\vec{x})}{\partial t} = g_z (z(\vec{x}) * \omega) (1 - |n * \omega_n|)^a (1 - |z|), \quad (1.12)$$

where  $a$  controls the strength of the coupling. A reciprocal coupling was not included in the ocular dominance dynamics as it was not needed. The form of the coupling was chosen because  $|n * \omega_n|$  is largest in the center of the ocular dominance stripes. The other reasonable choice  $|n|$  was not used as  $|n|$  reaches a constant value everywhere except directly on the domain walls in their simulations. This is consistent with a model of layer 4.

Swindale’s model shows most of the observed features in V1. It produces a pattern of ocular dominance bands, whose width can be adjusted by changing  $d_{n1}$  and  $d_{n2}$ . Persistence and width fluctuations can be modified also by changing  $\omega_n$ . Although a detailed study of this effect was not made, Swindale notes that strengthening the

negative portion of  $\omega_n$  increases persistence and decreases width fluctuations.[39] The reverse takes place when the positive portion of  $\omega_n$  is strengthened. Furthermore, allowing open boundary conditions naturally leads to bands that meet the edge perpendicularly. The domain walls are all very narrow, and the final distribution of  $|n|$  is almost uniform, as is seen in layer 4.

The expansion of the cortex is modeled by changing the spacing between lattice points, resulting in stripes that tend to run parallel to the direction of the expansion.[39] In reality, the expansion occurs entirely perpendicularly to the direction of the bands, a fact unknown at the time of the simulations.[30] The attempts to model monocular deprivation by using non-zero value of  $K$ , lead to difficulties. Rather than alternating narrow and wide stripes, islands of the suppressed eye form in a field of the open eye. Narrow and wide stripes are formed by combining monocular deprivation with cortical expansion, but here as before the stripes run in the wrong direction.

The orientation field develops a pattern of pinwheels of both circulations in equal numbers, as desired. The patterns show some of the features found in the experimental patterns: linear regions, saddle points, and fractures. Swindale notes, however, that the fractures are not true discontinuities but just areas of rapid change. As the simulation continues, the mean of the distribution of selectivity increases, eventually reaching a value of 1 everywhere. It is suggested that some outside process stops development before this takes place.

For significantly large values of the coupling,  $a$  in Eq. (1.12), the orientation singularities tend to occur in the center of ocular dominance bands. To ensure this effect, the development of the orientation field has to be slow enough (small  $g_z/g_n$ ) that the orientation field does not form completely before ocular dominance bands. Swindale did not explicitly study if lines of isoorientation crossed domain walls at right angles, but he does note that fractures tended to cross domain walls perpendicularly.

### 1.3.4 Neural Network Models

By far the majority of the models of V1 employ neural networks. While the filter and field models attempt a macroscopic description, the neural network approach attempts to microscopically model the actual connectivity of neurons.

Neural network models focus on a much shorter time scale than macroscopic ones which only simulate development on a scale of days or weeks. By contrast, microscopic models simulate the response to stimuli occurring on the scale of milliseconds, roughly 8 orders of magnitude less than the developmental scale. Computational limitations prevent neural network models from simultaneously simulating both microscopic response and macroscopic development. Most models choose a relatively small number of representative stimuli. The most ambitious can typically achieve only a ratio of  $10^4$  between response and developmental time scales.

In broad terms, the models are relatively simple: a stimulus is presented to the network, to which it responds according to a preexisting set of model synapses. The synapses are then modified based on the response using some sort of Hebbian learning rule. These steps are repeated many times to simulate development.[51]

Neural network modelers must do significant work to obtain many properties that are assumed in the more macroscopic approach. For example, in the early 1980's Kohonen developed a network that showed self-organizing topological maps.[52] This is needed to establish a retinotopic map in V1, a fact implicitly assumed in every field model. Much work on neural network models is also required to demonstrate the existence of orientation or ocular sensitive cells.[53]

A typical neural network model, such as the one developed by Malsburg in the early 1970's, has two layers of neurons.[54] Each layer is placed on a two dimensional lattice. One layer acts as input, while the other takes up the processing and output. The input layer,  $\{A_i(t)\}$ , is a retinotopic map of visual space. If a horizontal bar is the stimulus, then the neurons lying in a horizontal bar are active while the rest are dormant,

$$A_i(t) = \begin{cases} A & \text{if cell } i \text{ is in the stimulus pattern,} \\ 0 & \text{otherwise.} \end{cases} \quad (1.13)$$

Each cell in the input layer is initially randomly connected to a large number of neurons in the processing layer by weighted synapses. A strength  $s_{ik}$  connects input cell  $A_i(t)$  to processing cell  $H_k(t)$ . The neurons in the processing layer,  $\{H_k(t)\}$ , determine their activity by summing weighted inputs from the input layer, and neighboring neurons in the processing layer, as

$$\frac{d}{dt}H_k(t) = -\alpha_k H_k(t) + \sum_{l=1}^N p_{lk} \Theta(H_l(t) - \theta_l) + \sum_{i=1}^M s_{ik} A_i(t), \quad (1.14)$$

where  $\alpha_k$  is a decay constant for activity in cell  $k$ ,  $\theta_l$  is a threshold for activation of cell  $l$ , and  $M$  is the number of inputs connected to each cell. Each processing cell is connected to  $N$  other processing cells by weights  $p_{lk}$ . A fixed point in Eq. (1.14) gives the response in layer  $H_k(t)$  to the stimulus presented in  $A_k(t)$ . After the response is established, synaptic weights connecting active cells in the input and response layers are increased. Then all the weights are normalized. This simulates the development due to the presentation of a single stimulus. The weights connecting cells within the processing layer and the threshold values of the processing cells, do not change.

Other neural network models differ in several ways from Malsburg's, but retain the same principles. Some models vary the number of weights changed, number of layers, initial conditions, type of stimuli used, and many other details.[38, 55, 56, 57] Other models don't train directly with patterns, but with spatial correlations.[58, 59]

Most neural networks concentrate on the development of orientation columns rather than ocular dominance. They successfully show the development of orientation specific cells, and the clustering of these cells into regions preferring a single orientation, sometimes forming a pinwheel pattern. Unfortunately, the large computational requirements, and the large number of parameters, make it difficult to compare with the details of the structures observed experimentally.

A successful neural network model provides a detailed description of the connectivity, and the role of individual neurons. However, analytic calculations are difficult due to the long range and non-uniform interactions, while simulations can only explore space-time domains many orders of magnitude smaller than the actual cortex and

its development. Furthermore, the actual cortex contains hundreds of different types of cells, feed-back connections from extrastriate areas, and individual neurons much more complicated than their mathematical models. A neural network model may find a mechanism that can explain the development, but there is no guarantee that the mechanism is actually used in the cortex. Still, the types of mechanism found may be of great importance in designing computational networks, and providing insight into how the cortex functions.

# Chapter 2

## Macroscopic Modeling

### 2.1 General Methodology

Understanding the emergence of macroscopic behavior from the interactions of its microscopic components is the challenge of statistical mechanics. In the early part of this century Landau and Ginzburg developed a formal macroscopic approach to study phase transitions.[60, 61, 62, 63] Noting that several different phase transitions are modeled by similar Taylor expansions of an order parameter, Landau suggested that perhaps all phase transitions can be described in a similar manner. The method that grew out of this observation is known as the Landau-Ginzburg approach.

The Landau-Ginzburg approach deals only with macroscopic quantities, avoiding the complications of the underlying microscopic structure. It uses ideas of symmetry, continuity, stability, and locality to create simple equations that depend on phenomenological parameters. The values of these parameters are not determined from the approach, but are fit to experimental results. When successful, this approach generates equations that can model a wide range of phenomena by varying a few phenomenological parameters.

### 2.1.1 Length Scales

Most collective phenomena occur at length scales that are significantly longer than the size of the constituent parts of the system. The system changes slowly on these macroscopic length scales. For example, a gold-silicone alloy may separate into regions of pure gold and pure silicon with typical sizes of a few microns.[64] The pattern of these regions can be described on a scale of microns, even though the underlying lattice has a spacing in angstroms. Similarly, a wide variety of superconductors exhibit coherence lengths and London penetration depths of a few microns while the spacing between atoms is much smaller.

An ab initio microscopic approach has to start from the constituent particles and their interactions, from which the long scale behavior has to emerge. Such an approach is frequently quite complicated as the emergent properties are separated by many orders of magnitude in time and length scales from the input interactions. Furthermore, since it starts with the details of a particular system, it is unique to that system. For example, to study a gas with a microscopic approach requires considering a large collection of particles moving about and colliding. Microscopically modeling superconductors or binary alloys requires simulating the interactions among a huge number of individual atoms. As these interactions are fundamentally quantum mechanical, this undertaking must proceed through the many-particle wavefunction.

By contrast, the macroscopic approach starts with coarse graining the system to a length scale intermediate between the macroscopic scale of the collective behavior and the short scale on which its components interact. The system is then described by a few collective fields that fluctuate on the long length scale. A binary alloy can be characterized by the density difference,  $X(\vec{x}) = \rho_A(\vec{x}) - \rho_B(\vec{x})$  where  $\rho_A(\vec{x})$  and  $\rho_B(\vec{x})$  are the density of components A and B, respectively. The macroscopic density,  $X_A(\vec{x})$  is coarse grained to remove all fluctuations with frequencies higher than  $\Lambda$ . Since for a large range of  $\Lambda$  the macroscopic density remains unchanged, the subscript A is frequently dropped. This macroscopic density is a smooth, analytic function, unlike the microscopic density function which indicates if a particle is present exactly at



position  $\vec{x}$ ,

$$X_{\text{mic}} = \sum_{i=1}^N \left( \delta^3(\vec{x} - \vec{x}_i^A) - \delta^3(\vec{x} - \vec{x}_i^B) \right) \quad (2.1)$$

where  $\{x_i^A\}$  and  $\{x_i^B\}$  are the positions of the A and B particles, respectively. The macroscopic density can be obtained from the microscopic one by averaging over length scales  $1/\Lambda$ .

Macroscopically, a superconductor can be described by the wave function of the Cooper Pairs  $\psi(\vec{x})$ . This density of the superconducting component is given by  $n_s(\vec{x}) = |\psi(\vec{x})|^2$ . It is necessary to use the wave function rather than  $n_s(\vec{x})$  to accurately reflect the quantum nature of the superconductivity. This order parameter is coarse grained in a manner similar to the above density.

Sometimes it is possible to derive equations which describe how the macroscopic system develops directly from the microscopic approach. For example, macroscopic superconducting equations have been determined from a microscopic approach by Gor'kov.[65], but it is a long and laborious journey. Often it is desirable to take a phenomenological approach and determine the equations without appealing to the underlying microscopies. In this case symmetries can guide the determination of the equations, which have a number of phenomenological parameters that must be fitted to experiment. When the macroscopic approach is successful, the number of parameters is small. Changing the microscopic conditions, e.g. the type of particles in our alloy or superconductor, should only require changing the values of the phenomenological parameters. Since the equations are determined by symmetry, seemingly different systems that have the same symmetries are governed by similar equations.

### 2.1.2 Analytic Macroscopic Equations

We have learned to expect the coarse grained order parameters and evolution equations to be smooth, analytic functions. Non-analytic behaviors and sudden changes are removed by the averaging procedure. The governing equations are then expressed by the first few terms of a power series, and a finite number of derivations. A wide variety of physical systems are successfully described this way, from superfluids and

superconductors to ferromagnets and binary alloys. For example, in the case of the binary alloy, the microscopic density is a highly non-analytic function, while the macroscopic density is smooth and well behaved. The smoothness of the macroscopic system usefully limits the types of functions that need to be considered in governing equations.

Some existing macroscopic models of the visual cortex use interactions which are not analytic and thus not suited for the macroscopic approach. For example, Swindale's model couples the orientation at one point to the ocular dominance over a wide area, see Eq. (1.12). Biologically, it may be plausible for the orientation at one point to interact with the ocular dominance in a complicated manner through a kernel function, and such coupling may give desired results. However, this type of interaction should not be needed in a macroscopic model, where coarse graining should result in smooth, analytic interactions. While it may give desirable results, it adds many parameters to the model.

### 2.1.3 Cost Functions

The principle of energy conservation is at the foundation of our understanding of physical systems. In the microscopic domain, the energy of a system is calculated as a *Hamiltonian* which sums the potential and kinetic energies of the individual constituents (atoms, or electrons and nuclei, depending on the level of detail). At the macroscopic level, the appropriate quantity is the internal energy introduced in the framework of thermodynamics. At this level of abstraction the sum of incoherent kinetic energies is replaced by the phenomenological quantity heat.

Another aspect of the macroscopic (thermodynamic) perspective is the role played by the environment. While in an isolated atom, composed of electrons and a nucleus, the energy is strictly conserved, for a spinning top the energy is dissipated through interactions with the environment. Such dissipation leads to states of lower energy, until eventually the top reaches an equilibrium states with no spin, setting on its side.

The lowest energy state does not characterize the equilibrium of a system coupled to the environment in all cases. For example, a system held at a constant temperature

does not seek a minimum energy, which would require losing all its thermal energy. Instead, it seeks a minimum of the Helmholtz free energy. For other systems energy is generalized to enthalpy or Gibbs free energy, but in all cases we discover that the system evolves so as to minimize some generalized energy. To make contact with concepts used in neural models, we call this generalized energy a cost function.[51]

In some cases the cost function of a system can be calculated from a microscopic approach. For the binary alloy with  $N$  particles the interaction energy is given by,

$$E = \sum_{ij} V_{AB}(\vec{x}_i^A - \vec{x}_j^B) + \sum_{\langle ij \rangle} V_{AA}(\vec{x}_i^A - \vec{x}_j^A) + \sum_{\langle ij \rangle} V_{BB}(\vec{x}_i^B - \vec{x}_j^B), \quad (2.2)$$

where  $V_{AB}(\vec{x})$ ,  $V_{AA}(\vec{x})$ , and  $V_{BB}(\vec{x})$  are the potentials between particles. This energy can be simplified by placing the particles on a lattice of fixed sites and looking only at interactions between adjacent sites. Such simplifications, already throw out much microscopic detail such as the interaction between electrons, and the motions of the nuclei.

In the macroscopic approach, a phenomenological energy is constructed as a function of the order parameter, based on a few general principles: The function should be *translationally invariant*, so that moving the entire system a uniform amount has no effect. To ensure translational invariance, the cost function should not depend explicitly on  $\vec{x}$  only implicitly through the order parameter,  $X(\vec{x})$ . Due to the averaging process, the cost function should be an *analytic* function of  $X(\vec{x})$ , as discussed in Sec. (2.1.2), represented as a power series in  $X(\vec{x})$  and its derivatives. For most physical systems the cost function is *local*, as most interactions in nature occur primarily between nearby particles. This implies that the cost function should rely on only a few derivatives of  $X(\vec{x})$ . Many systems are also *rotationally symmetric*, so that rotating the entire system does not change its cost function. In this case terms such as  $\vec{b} \cdot \nabla X(\vec{x})$  are prohibited. Systems subject to environmental influences such as an external magnetic field, may not be rotational symmetric. Subject to these

restrictions, the cost function must have the form,

$$F(\{X(\vec{x})\}) = \int d^3x \left[ a_1 X(\vec{x}) + a_2 X(\vec{x})^2 + a_3 X(\vec{x})^3 + \dots \right. \\ \left. + b_1 \nabla^2 X(\vec{x}) + b_2 (\nabla X(\vec{x}))^2 + \dots \right]. \quad (2.3)$$

The terms in the cost function are further limited by the symmetry of the system. If the cost of the binary alloy is unchanged under globally exchanging A and B atoms, i.e.  $X(\vec{x}) \rightarrow -X(\vec{x})$ , then no odd terms in  $X(\vec{x})$  can be present leaving only,

$$F(\{X(\vec{x})\}) = \int d^3x \left[ a_2 X(\vec{x})^2 + a_4 X(\vec{x})^4 + \dots \right. \\ \left. + b_2 (\nabla X(\vec{x}))^2 + \dots \right]. \quad (2.4)$$

The next allowed derivative terms are high order in  $X(\vec{x})$  or  $\nabla$  such as  $(\nabla^2 X(\vec{x}))^2$  or  $X(\vec{x})^2 (\nabla X(\vec{x}))^2$ . The term  $X(\vec{x}) \nabla^2 X(\vec{x})$  is equivalent to  $(\nabla X(\vec{x}))^2$  under integration except for surface terms. If the order parameter is complex number or a vector, the cost function is a series in  $|X(\vec{x})|^2$  and the lowest order derivative term is  $|\nabla X(\vec{x})|^2$ .

## 2.2 Equilibrium

A system is in equilibrium when its *macroscopic properties* do not change with time. The system constantly fluctuates on the microscopic scale as its individual components move about and interact, but in equilibrium these microscopic changes do not effect the macroscopic description.

Equilibrium states are particularly interesting because they give stable long term behavior. Once an isolated system enters an equilibrium state, by definition, it remains there. No physical system ever achieves this ideal equilibrium, as no system is truly isolated from the rest of the universe. In practice, equilibrium means that the system is stable on some long time scale appropriate to a set of observations.

A system in equilibrium is characterized by a few macroscopic variables. A gas, for example, may be characterized by its temperature, volume, and pressure. A

binary alloy can be described by its temperature and the difference between the constituents' densities,  $X$ , while a superconductor is described by the temperature, applied magnetic field, and the superconducting order parameter.

### 2.2.1 Phase Transitions

Small changes in some of the macroscopic variables of a system can induce great changes in others. For example, cooling a gas through its boiling point causes changes in volume and pressure as the vapor condenses. This point of qualitative macroscopic change is called a phase transition. Each of possible homogeneous behaviors, e.g. the gas and the liquid, are called phases.

The study of phase transitions is a particularly challenging problem in statistical mechanics as qualitative changes takes place in the macroscopic behavior of the system, while the underlying microscopic Hamiltonian has changed very little. Describing exactly how the collective behavior changes requires insight over a large span of length and time scales.

Phase transitions are generally classified into first or second order. First order transitions are marked by two phase coexistence, and the presence of latent heats. In a first order transition two phases, like gas and liquid, both have the same free energy and coexist. The first derivative of the free energy has a discontinuity resulting in a latent heat. The term "second order" was coined for transitions with a discontinuity in the second derivative of the free energy, but now the term is generally applied to all transitions that are not first order. A more complete discussion of phase transitions can be found in most statistical mechanics texts.[66, 64]

In the next two sections, we look at macroscopic models of phase transitions in binary alloys and superconductors in more detail. These two systems are of particular interest because they have symmetries similar to ocular dominance and orientation selectivity. Binary alloys are a mixture of two metals, as ocular dominance patterns are a mix between two eyes. A particular region can either be thoroughly mixed, binocular, or exhibit preference for one component, monocular. Slightly less obviously, both superconductors and orientation patterns have an order parameter with a continuous

symmetry. Orientation patterns have a preferred angle varying continuously, while superconductors have a quantum mechanical phase that also varies continuously.

### 2.2.2 Binary Alloys

A binary alloy is a mixture of two metals, for example  $\beta$ -brass is a mixture of zinc and copper on a body centered cubic lattice. At extremely low temperatures, a completely ordered state exists with a cubic lattice of zinc and an offset cubic lattice of copper such that a copper atom appears at the center of each zinc unit cell. At higher temperatures it becomes possible for the zinc and copper atoms to exchange places. At a temperature of 742 K a phase transition takes place and the copper and zinc become thoroughly mixed. Below that temperature X-ray diffraction reveals two sets of atomic planes, one for copper and one for zinc, while above that temperature only one set of planes for the copper-zinc mixture is detected.[66]

While in  $\beta$ -brass, the microscopic interactions favor zinc and copper atoms to be next to each other, in other alloys and binary solutions, the interactions favor like atoms to be adjacent. The ordered phase segregates into A and B rich domains. Due to the similarity to ocular dominance, we shall develop a model for the latter phase separation from the macroscopic perspective. To simplify the calculations, we choose to work with two metals A and B which are symmetric under interchanging all A's and all B's. The alloy can then be described by an order parameter  $X = \rho_A - \rho_B$ . Above the transition temperature the two metals are thoroughly mixed, so that  $X$  is zero. Below the transition temperature, we expect both nearly pure A and nearly pure B to be present, so  $X$  has two degenerate values, one positive and one negative. We can construct a simple macroscopic free energy function, in terms of  $X$ ,

$$F(X) = a_0 + \frac{a_2}{2}X^2 + \frac{a_4}{4}X^4 + \dots, \quad (2.5)$$

where  $a_0$ ,  $a_2$ , and  $a_4$  are arbitrary constants that may depend on temperature. As a first step we have assumed that  $X$  is uniform across the system, which is called a mean field approximation. Odd powers of  $X$  are not present due to our assumed

symmetry between A and B. We are interested in studying the vicinity of the phase transition where  $X$  is small, so an expansion in  $X$ , keeping only the first few non-zero terms, is justified.

To clarify the extrema of Eq. (2.5) (corresponding to equilibrium points), we examine the first and second derivatives of  $F$  with respect to  $X$ ,

$$\begin{aligned}\frac{\partial F(X)}{\partial X} &= X(a_2 + a_4 X^2), \\ \frac{\partial^2 F(X)}{\partial X^2} &= a_2 + 3a_4 X^2.\end{aligned}\tag{2.6}$$

It is clear that  $X = 0$  is a stable minimum if  $a_2 > 0$  and an unstable solution if  $a_2 < 0$ . To model the transition, the constant  $a_2$  must switch signs at  $T = T_c$ , the transition temperature: hence  $a_2 \propto t = (T - T_c)/T_c$ , with an unknown constant of proportionality.

Above  $T_c$ ,  $X = 0$  is the only stable solution. Below the critical temperature there are two stable solutions,  $X_{\text{eq}} = \pm\sqrt{-t/a_4}$ . The coefficient  $a_4$  must be positive to give finite solutions. In a region between  $-X_{\text{eq}}/\sqrt{3}$  and  $X_{\text{eq}}/\sqrt{3}$ , the function  $F(X)$  is not convex so that such densities are not locally stable. Instead of a uniform density, the alloy divides into regions which are A rich, and regions that are B rich, to minimize the free energy. The global density is maintained, by adjusting the sizes of the two types of regions. The points where decomposition sets in,  $\pm X_{\text{eq}}/\sqrt{3}$  are called spinodal points.

The regions that are A rich or B rich are called domains. In each domain, the alloy locally takes on one of the equilibrium ratios. The boundaries between domains, domain walls, are defects where the order parameter cannot take on an equilibrium value. Thus, these defects have a cost penalty. The global lowest energy state consists of a single large A-rich domain and a single large B-rich domain, thus minimizing the area of the costly domain walls.

Although the free energy changes smoothly across the phase transition, the heat

capacity experiences a finite jump,

$$\frac{C}{V} = \begin{cases} 0 & (t > 0), \\ \frac{3kT_c^2}{2a_4} & (t < 0). \end{cases} \quad (2.7)$$

This is a signature of a second order phase transition.

The macroscopic approach can thus model the phase transition in binary alloys without resorting to studying the solid state properties of the metals themselves. A mean field approach assuming a uniform  $X$ , describes the nature of a phase transition from a disordered state to an ordered state where regions rich in one of the metals arise. The regions are separated by domain wall defects that incur a cost penalty for being away from the equilibrium values of the order parameter. These regions form patterns, which cannot be obtained from this mean field approach, but may be modeled by extending it to non-uniform  $X(\vec{x})$ .

### 2.2.3 Superconductors

At low temperatures many metals show no resistance to the flow of current; they become superconductors. The change from normal to superconductor takes place over a narrow temperature range and constitutes a phase transition. In the superconducting state a finite fraction of the electrons (Cooper pairs) enter into a superconducting component that flows without resistance. The superconductor is also a perfect diamagnet, expelling any magnetic field from its interior. Sufficiently strong magnetic fields eventually destroys superconductivity. In type I superconductors this happens at a critical field  $H_{c1}(T)$ . By contrast, in type II superconductors, magnetic field lines penetrate the superconductor in a field interval between  $H_{c1}(T)$  and  $H_{c2}(T)$  to form the so called mixed vortex state. A complete discussion of superconductivity can be found in a variety of texts.[67, 68]

In 1950 Ginzburg and Landau began the development of a macroscopic model for superconductors.[62, 63] Their work is one of the foundations of the Landau-Ginzburg approach, which has now been generalized to to describe dynamic as well as static sys-



tems. Their original paper, however, describes the behavior of a static superconductor in a magnetic field. They choose as their order parameter an effective wave function  $\Psi(\vec{x})$  whose square magnitude gives the density of the superconducting component,  $n_s(\vec{x}) = |\Psi(\vec{x})|^2$ . Despite the use of a wave function, this is a macroscopic and not quantum mechanical approach. The wave function is necessary to accurately model the symmetry of the superconducting component that has a complex phase. While the complex phase is not observable, it must be included for a correct description.

When developing their macroscopic model, Landau and Ginzburg first consider a local free energy arising from a uniform (mean field)  $\Psi$ ,

$$F(\Psi, T) = a_0(T) + a_2(T)|\Psi|^2 + \frac{a_4(T)}{2}|\Psi|^4, \quad (2.8)$$

where  $a_0(T)$ ,  $a_2(T)$ , and  $a_4(T)$  are arbitrary parameters which may be temperature dependent. Symmetry requires that all terms depend on  $|\Psi|$  and analyticity around  $\Psi = 0$  prohibits odd terms. The coefficient  $a_0(T)$  can be immediately identified with the normal, non-superconducting, free energy,  $F_N$ . The equilibrium value of  $\Psi$  is given as a minimum of the free energy. Since  $|\Psi|^2 = 0$  for  $T > T_c$  and  $|\Psi|^2 > 0$  for  $T < T_c$ ,  $a_2(T_c) = 0$ ,  $a_4(T_c) > 0$ , and  $a_2(T < T_c) < 0$ .

For superconductors, the coefficients  $a_2(T)$  and  $a_4(T)$  can be expressed in terms of two macroscopic properties, the critical field,  $H_c(T)$ , and the London penetration depth,  $\lambda(T)$ , which are more easily observable experimentally. The equilibrium value of  $|\Psi|^2$  for  $T < T_c$  is,

$$|\Psi_{\text{eq}}|^2 = -\frac{a_2(T)}{a_4(T)}. \quad (2.9)$$

Using the equilibrium value of the  $\Psi$ , the free energy difference between the superconducting and the normal phases can be found. This free energy difference is equal to the critical field energy required to suppress superconductivity, i.e.,

$$F(\Psi, T) - F_N = -\frac{a_2^2(T)}{2a_4(T)} = -\frac{H_c^2(T)}{8\pi}. \quad (2.10)$$

From London theory,  $\lambda^2(T) \propto 1/n_s(T)$ , giving a second relation,

$$\frac{\lambda^2(0)}{\lambda^2(T)} = \frac{|\Psi_{\text{eq}}(T)|^2}{|\Psi_{\text{eq}}(0)|^2} = -\frac{a_2(T)}{a_4(T)}. \quad (2.11)$$

Together, Eqs. (2.10) and (2.11) determine  $a_2(T)$  and  $a_4(T)$  in terms of experimentally accessible quantities, as

$$\begin{aligned} a_2(T) &= -\frac{H_c^2(T)\lambda^2(T)}{4\pi\lambda^2(0)}, \\ a_4(T) &= -\frac{H_c^2(T)\lambda^4(T)}{4\pi\lambda^4(0)}. \end{aligned} \quad (2.12)$$

Examining only the local terms in the free energy, Eq. (2.8), gives a second order phase transition much like we found in binary alloys. However, while below a critical temperature,  $|\Psi|$  has a finite equilibrium value, unlike a binary alloy it does not form domains of two possible values. Since the phase of  $\Psi$  can change continuously there are no sharp domain walls in the superconductor.

The defects in a superconductor have a different character: Since the phase of  $\Psi$  must be continuous, it changes by a multiple of  $2\pi$  when a closed loop is traversed. If the phase changes by  $0$ , the loop can be continuously deformed to a point. However, if the loop contains a non-zero multiple of  $2\pi$  it also contains a topological defect called a vortex and cannot be shrunk to a point. In a two dimensional system the vortex is simply a point of singularity, while in a three dimensional system it forms lines. The ends of each vortex line must either terminate on an edge, or form a closed vortex loop. Both types of vortex lines have been observed in superconductors.

At the center of each vortex, there is no superconductivity and  $|\Psi|$  is zero. Around a vortex all possible phases circulate in either clockwise or counterclockwise direction. Since at the vortex the order parameter does not have its equilibrium value it has an energy penalty. The free energy would indeed be reduced if the equilibrium value of  $|\Psi|$  could be reached at all points, but this is prevented by the requirement that the phase as well as the magnitude of  $\Psi$  be continuous. The lowest possible free energy state does not contain any vortices, but vortices can arise as defects either

when superconductivity sets in or as the result of the application of a magnetic field. Rather than result in the complete loss of super conductivity, in type II material, a magnetic field is confined to vortices, while the bulk of the material remains a superconductor.

Landau and Ginzburg also explored the effects of a non-uniform  $\Psi(\vec{x})$ . They include a term in the free energy proportional to the  $|\nabla\Psi(\vec{x})|^2$  which looks like a kinetic energy in quantum mechanics. To account for the interaction between the current and the magnetic field and to ensure gauge-invariance, a so called covariant derivative  $(-i\hbar\nabla\Psi(\vec{x}) - \frac{e}{c}\vec{A}(\vec{x})\Psi(\vec{x}))$  replaces the normal derivative in the presence of the electromagnetic gauge potential  $\vec{A}(\vec{x})$ . The total free energy density includes the local terms in Eq. (2.8), the gradient terms, and the energy of the field itself, yielding

$$F(\Psi, T) = \left[ a_0(T) + a_2(T)|\Psi(\vec{x})|^2 + \frac{a_4(T)}{2}|\Psi(\vec{x})|^4 \right] + \frac{1}{2m} \left| -i\hbar\nabla\Psi(\vec{x}) - \frac{e}{c}\vec{A}(\vec{x})\Psi(\vec{x}) \right|^2 + \frac{H^2(\vec{x})}{8\pi}, \quad (2.13)$$

where  $e$  and  $m$  are phenomenological parameters associated with the effective charge and mass of the electron pairs in the superconductor.

Varying Eq. (2.13) with respect to  $\Psi^*(\vec{x})$  gives a differential equation for  $\Psi(\vec{x})$  and  $\vec{A}(\vec{x})$ .

$$\left[ a_2(T) + a_4(T)|\Psi(\vec{x})|^2 \right] \Psi(\vec{x}) + \frac{1}{2m} \left[ -i\hbar\nabla - \frac{e}{c}\vec{A}(\vec{x}) \right]^2 \Psi(\vec{x}) = 0. \quad (2.14)$$

Varying the free energy with respect to  $\vec{A}(\vec{x})$  using the London gauge,  $\nabla \cdot \vec{A}(\vec{x}) = 0$ , gives a second differential equation,

$$\nabla^2 \vec{A}(\vec{x}) = \frac{2\pi ie\hbar}{2m} [\Psi^*(\vec{x})\nabla\Psi(\vec{x}) - \Psi(\vec{x})\nabla\Psi^*(\vec{x})] + \frac{4\pi e^2}{mc^2} |\Psi(\vec{x})|^2 \vec{A}(\vec{x}). \quad (2.15)$$

Together these two non-linear partial differential equations determine  $\Psi(\vec{x})$  and  $\vec{A}(\vec{x})$ .

Although quite complicated, the equations generated for  $\Psi(\vec{x})$  and  $\vec{A}(\vec{x})$  can be solved to give much of the observed behavior of superconductors. Abrikosov and

others have used them to study the vortex defects discussed earlier.[69] Without dealing with the specific nature of super conductivity, Landau and Ginzburg are able to determine constitutive equations for the order parameter. These equations have been independently derived from microscopic theory by Gor'kov, adding to the credibility of this approach.[65]

The study of superconductors is intimately related to the study of superfluids. Both express very similar behavior and can be described using the same approach. In a superfluid, a zero viscosity component has an order parameter with unobservable phase angle. Since superfluids have the same symmetries as superconductors, they are described by very similar equations. However, since the superfluid component has no charge, the phenomenology implies no coupling to the electromagnetic field needs to be included.

## 2.3 Dynamics

The cost function determines many of the equilibrium properties of a system. It determines the phase for a given set of macroscopic conditions as well as the nature of the transitions between different phases. It also characterizes the static response functions, as well as some correlations of equilibrium fluctuations. The cost function, however, does not determine how the system reaches equilibrium and its dynamic properties. The dynamic properties include relaxation times, responses to time dependent perturbations, and transport coefficients.

The dynamics of a system may belong to one of many classes, depending not only on its cost function, but also on other conditions. One broad way to classify dynamics is into dissipative and non-dissipative. Dissipative systems seek to lower their cost and relax to a lowest cost or equilibrium configuration. Non-dissipative systems conserve the cost, possibly changing between configurations of equal cost. We discuss two possible dissipative dynamics in the following sections, drawing upon work by Hohenberg and Halperin.[70]

### 2.3.1 Systems with No Conservation Laws

The simplest type of dissipative dynamics is one that is purely relaxational. The overall cost is a functional of the order parameter and assigns a real number to every possible system configuration. For the moment, let us consider the cost function of superconductors,  $F(\Psi)$ , given in Eq. (2.13). This function creates a “landscape” in the high dimensional phase space of possible  $\{\Psi(\vec{x})\}$ . A dissipative system seeks to lower its cost by moving to lower cost configurations. It can do this just as water flowing down a hill by going down the path of steepest gradient,

$$\frac{\partial \Psi(\vec{x})}{\partial t} = -\mu \frac{\partial F(\Psi)}{\partial \Psi(\vec{x})}, \quad (2.16)$$

where the “mobility”,  $\mu$ , describes how rapidly the system moves toward equilibrium. Eq. (2.16) describes the time evolution of  $\Psi(\vec{x})$ , and its corresponding equation of motion. The system continues to evolve according to its equation of motion until it reaches a minimum.

A system following Eq. (2.16) evolves completely deterministically, and comes to rest at the first *local minimum* where  $\partial F/\partial \Psi = 0$ . There may be other global minima with lower cost, but the system is prevented from reaching them because there is no way to climb out of a metastable minimum. Furthermore, most physical systems at finite temperatures experience natural equilibrium fluctuations. It is then natural to include the effect of the environment (and also the degrees of freedom removed in the coarse graining step) by adding a noise term such that,

$$\frac{\partial \Psi(\vec{x})}{\partial t} = -\mu \frac{\partial F(\Psi)}{\partial \Psi(\vec{x})} + \theta(\vec{x}, t). \quad (2.17)$$

The noise,  $\theta(\vec{x}, t)$ , is usually taken from a Gaussian distribution of zero mean, with no correlations in space and time. To achieve the proper Boltzmann weights for the equilibrium states, the mobility and the variance of the noise are related by the the

Einstein fluctuation-dissipation condition,

$$\langle \theta(x, t) \theta(x', t') \rangle = 2D \delta(x - x') \delta(t - t'), \quad (2.18)$$

with  $D = \mu k_B T$ . The random fluctuations introduced by  $\theta$  allow the system to move over a cost barrier, and hence to evolve toward the global minimum of the cost function. Of course, once they reach the global minimum, random fluctuations out of this minimum are also possible. A process of annealing, where the effective temperature is slowly reduced, is sometimes used to find the global minimum of a complicated cost function.

### 2.3.2 Systems with a Conserved Order Parameter

Some systems have an order parameter that must be conserved. In superconductors the order parameter,  $\Psi(\vec{x})$ , does not need to be conserved as the entire system may become superconducting or normal. However, the order parameter for our binary alloy,  $X(\vec{x})$ , must be conserved as the relative number of A and B atoms does not change in the mixing process.

The dynamics introduced in the previous section do not satisfy this conservation constraint. However, other simple dynamics can be devised that incorporate this constraint. In particular, in the so called B dynamics,

$$\frac{\partial X(\vec{x})}{\partial t} = -\lambda \nabla^2 \frac{\partial F(X)}{\partial X(\vec{x})} + \theta(\vec{x}, t), \quad (2.19)$$

where  $\lambda$  is a transport coefficient.[70] If this equation of motion is integrated over all space, the Laplacian ensures that the net change in  $\int X(\vec{x})$  is zero except for surface effects. This preserves the global ratio of the atoms in the mixture while allowing it to vary locally. The variance of the noise must also be corrected according to  $\langle \theta(x, t) \theta(x', t') \rangle = 2\lambda k_b T \delta(x - x')$ .

It is important to note that the dynamics are not uniquely determined by the cost function. An identical cost function could be used in both types of dynamics

discussed above, giving very different results. In fact the cost functions we developed for binary alloys and superconductors are quite similar but must experience different dynamics because of different conservation constraints.

### 2.3.3 Discrete Systems

Although the macroscopic approach generally gives simple cost functions and equations of motion, they are frequently still too complicated to be solved analytically. To solve them numerically, both time and space need to be made discrete. Space is broken into a lattice on the scale of the coarse graining, which is intermediate between the lengths of the microscopic units, and the macroscopic fluctuations. The discrete cost function has derivatives replaced by coupling between sites. A continuous cost function for a spatially varying order parameter,  $X(\vec{x})$ , must be integrated over all space to give a total cost,

$$F(X) = \int d^3x \left[ a_1 X(\vec{x}) + a_2 X(\vec{x})^2 + a_3 X(\vec{x})^3 + \dots + |\nabla X(\vec{x})|^2 + \dots \right]. \quad (2.20)$$

The integration is replaced by summation over all the sites on a discrete model,

$$F(X) = \sum_i \left( a_1 X_i + a_2 X_i^2 + a_3 X_i^3 + \dots \right) + \sum_{ij} (b_1 X_i X_j + \dots), \quad (2.21)$$

where  $X_i$  is the value of  $X(\vec{x}_i)$  for each site  $\vec{x}_i$ . Time is also divided into discrete units on a scale between the time scale of the microscopic processes and the macroscopic changes. A discrete equation of motion results, such as

$$\frac{\Delta X(\vec{x})}{\Delta t} = -\mu \frac{\partial F(X)}{\partial X(\vec{x})}. \quad (2.22)$$

Landau-Ginzburg macroscopic modeling techniques have been applied to a wide variety of systems, including binary alloys and superconductors, but also ferromagnets, superfluids, and dipolar liquids. This approach avoids the microscopic details of the systems, and is instead based on symmetries and conservation laws. Both

static and dynamic properties can be described in terms of few phenomenological parameters.



# Chapter 3

## Results of Modeling

We develop a macroscopic model for ocular dominance and orientation based on the Landau-Ginzburg approach. We do not attempt to simulate the intricate interactions between neurons but instead develop a phenomenological picture of the observed patterns. Our model describes an evolving field, and in this respect is similar to that of Swindale.[39, 49, 50] We motivate our equations with ideas of symmetry and analyticity developed while studying many physical systems. This approach frees us from becoming entangled in the complexities of modeling individual neurons, which requires dealing with both their great variety and number. It also allows us to easily apply insight gained from many other systems, which although they may have vastly different constituent parts, have similar symmetries.

In Sec. (3.1) we develop a model for ocular dominance, while in Sec. (3.2) we consider orientation preference and selectivity. Finally, in Sec. (3.3) we explore coupling the two models.

### 3.1 Ocular Dominance

Our model for ocular dominance is motivated by the Landau-Ginzburg approach discussed in Chap. (2). We wish to produce patterns of ocular dominance similar to those observed experimentally, as described in detail in Sec. (1.2.2), whose key features are reviewed again here. Ocular dominance bands show a pattern of wan-

dering and branching, with roughly 0.04 branches per (band)<sup>2</sup>. The width of the bands fluctuates around 0.4 to 0.5 mm. The bands tend to intersect the boundary of the primary visual cortex perpendicularly. Away from the boundary the bands tend to run toward the calcarine fissure, at least in the top operculum. The domain walls between the bands are sharp in layer 4 and gradual in the other layers. During post-natal development, the cortex grows by roughly 16%, entirely perpendicularly to the bands. Binocular deprivation has little or no effect on development, while monocular deprivation during a critical period of early development causes the bands corresponding to the deprived eye to shrink while the other bands grow. After the critical period monocular deprivation has little effect.

### 3.1.1 Local Variables and Cost Function

Ocular dominance can be completely specified by a real field  $m(\vec{x})$ , with eye preference at a point  $\vec{x}$  given by the sign of  $m(\vec{x})$ . Positive values represent one eye while negative values represent the other. The strength of the preference is given by  $|m(\vec{x})|$ . From the outset we assume a discrete lattice and label  $m(\vec{x}_i)$  with  $m_i$  for each lattice point  $\vec{x}_i$ .

We shall initially introduce a *local* cost function  $F(m_i)$  that describes how closely the variables at site  $i$ , satisfies various required properties. The microscopic form of this cost function is presumably very complex, and presently not well understood. It may reflect a need to minimize the length of “cortical wiring”, the necessity of having information from both eyes in close proximity to determine binocular disparity, or a variety of developmental constraints.[37]

Since we are approaching development from a macroscopic, phenomenological view, we need not worry about these details. Our cost function depends smoothly on  $m_i$ , limited by symmetry, with a few parameters to be fit to observed patterns. In a normal healthy subject, both eyes should be treated similarly, so the cortical cost must be invariant under  $m \rightarrow -m$ . This constraint eliminates all odd terms of  $m$  in

the cost function leaving,

$$F(m_i) = a_2 m_i^2 + a_4 m_i^4 + \dots, \quad (3.1)$$

where  $a_2$ ,  $a_4$ , etc. are, as of yet, arbitrary constants.

Experience with many other systems (as well as simplicity) suggests that the cost function should depend on only the first few terms in the expansion. We wish the cost function to have its minimum for finite, non-zero values of  $|m_i|$ , as monocular regions (corresponding to a finite  $|m_i|$ ) are the prevalent feature. A minimum at  $m_i = 0$  would lead to binocular regions. Choosing  $a_2$  to be negative ensures that  $m_i = 0$  is not a minimum, while setting  $a_4 > 0$  and all higher order coefficients zero, results in minimum at a finite value of  $m_i$ . It is, of course, possible to meet the requirement for a finite, non-zero minimum in the cost function by many other combinations of higher order terms, but the above simplest choice is generically sufficient.

With only local interactions, each site is completely independent. A steepest descent minimization of the cost function gives an equation for each  $m_i$ ,

$$\tau \frac{\partial m_i}{\partial t} = -\frac{\partial F(m_i)}{\partial m_i} = -2a_2 m_i - 4a_4 m_i^3, \quad (3.2)$$

where  $\tau$  reflects the rate at which the system relaxes. Most of our discussion will be in terms of the equations of motion, although we will occasionally refer directly to a cost function when it is useful.

The coefficients,  $a_2$  and  $a_4$ , can be absorbed into  $m$  and  $\tau$  by appropriately changing units,

$$\tau \frac{\partial m_i}{\partial t} = m_i - m_i^3. \quad (3.3)$$

In this form, an unstable fixed point at  $m_i = 0$  and stable fixed points at  $m_i = \pm 1$  become obvious. In these unit,  $\tau$  is clearly a relaxation time. These local terms result in ocular dominance, but without any coupling between sites, we cannot hope to generate the desired patterns.

### 3.1.2 Short-range Coupling

The simplest type of coupling is a nearest neighbor interaction between adjacent sites,

$$\tau \frac{\partial m_i}{\partial t} = m_i - m_i^3 + \sum_{j \in \text{n.n.}} k_{ij} (m_j - m_i), \quad (3.4)$$

where  $k_{ij}$  is the interaction matrix which determines the strength of the coupling between any two adjacent sites  $i$  and  $j$ . To a first approximation the processes mediating the development of the cortex should be same across its surface and lack any preferred direction, so the interaction should be both translationally invariant and isotropic.

Both the 16% growth of the cortex, and the trends in ocular dominance stripes observed by LeVay, suggest that the actual interaction may not be fully translationally invariant and isotropic. The growth is believed to occur entirely perpendicularly to the stripes, possibly causing an anisotropy. LeVay has found that the stripes on the operculum tend to run toward the calcarine fissure, while stripes on the roof of the calcarine fissure run in a perpendicular direction. This suggests an anisotropic interaction that varies with location. Since these effects are small and their origin is not well understood, we choose to ignore them in our model.

The coupling is then uniform between all nearest neighbors,

$$\tau \frac{\partial m_i}{\partial t} = m_i - m_i^3 + k_s \sum_{j \in \text{n.n.}} (m_j - m_i). \quad (3.5)$$

The coupling between adjacent sites,  $k_s$ , must be positive to ensure the continuity of domains, i.e. produce regions with a uniform value of  $m_i$ . A negative  $k_s$  causes adjacent sites to alternate in sign, creating features in the pattern alternating on the same scale as the lattice itself. With positive  $k_s$ , the absolute minimum of the cost function, the ground state, is a uniform pattern with all  $m_i = 1$  or all  $m_i = -1$ . Thus, there are two degenerate ground states.

## Implementation

To study the consequences of these equations, we simulate them numerically using discrete time steps,

$$\Delta m_i = \Delta t \left( m_i - m_i^3 + k_s \sum_{j \in \text{n.n.}} (m_j - m_i) \right), \quad (3.6)$$

where  $\Delta m_i$  is the discrete change in  $m_i$ , and  $\Delta t$  is the time step. The time constant,  $\tau$ , has been set to one for convenience.

The model is studied on a discrete hexagonal lattice, so that each site has 6 nearest neighbors, and  $6n$   $n$ th neighbor sites. The use of a hexagonal lattice avoids the highly anisotropic effects of the diagonals in the square lattice. Sec. (3.1.3) discusses the artifacts of the discrete lattice.

The initial values of  $m_i$  were chosen randomly and independently from a distribution centered at 0. We typically used a uniform distribution that allowed  $m_i$  to be a few percent of the saturation value. This distribution mimics the initial fluctuations in ocular dominance. Since layer IV is completely enervated by both eyes in the prenatal monkey, it is reasonable to assume that the initial ocular dominance is near zero. The exact distribution is unknown, but has little impact on the simulations.

After a few time constants, a pattern of ocular dominance becomes apparent. The values of  $|m_i|$  rise rapidly during this time, approaching a value of 1. This period of growth simulates the critical period observed in the monkey. The length of the critical period depends on the initial conditions used. During the initially stages of growth,  $m_i^3$  is small and the equation is linear. The characteristic time scales are then obtained by diagonalizing the interaction matrix. The eigenmode with a uniform  $m_i = \bar{m}$  evolves according to a simple equation,

$$\tau \frac{\partial \bar{m}}{\partial t} = \bar{m}. \quad (3.7)$$

The number of time constants required for  $\bar{m}$  to reach the saturation value of  $\pm 1$  is

given by,

$$\frac{t}{\tau} = -\ln |\bar{m}_0|, \quad (3.8)$$

where  $|\bar{m}_0|$  is the typical initial magnitude. Once the value of  $|\bar{m}|$  reaches a significant fraction of 1, the linear approximation breaks down, but the value of  $k_s$  and the initial conditions typically used give a saturations time on the order of a few time constants as observed in the simulation.

After this initial period of rapid development, the pattern undergoes smaller changes along the borders between domains. Although changes continue for many time constants, the pattern is basically frozen. In addition to its frozen appearance, the pattern is no longer sensitive to small perturbations. If a small uniform field is added initially, it has a dramatical effect on the pattern development, while the same field added after this critical period has little effect, as discussed in Sec. (3.1.3).

### Domain Walls as Defects

Iterating Eq. (3.6) results in a pattern of splotchy domains of  $m_i = \pm 1$  separated by domain walls, as shown in Fig. (3-1). These domain walls are the natural defects in a system with two possible stable states. Regions evolve toward either  $m_i = 1$  or  $m_i = -1$  depending on which was favored by local initial conditions. Since the interactions are of finite range, spatially separated regions evolve toward different fixed points. The boundaries between these regions form domain walls where  $m_i$  changes rapidly.

With only nearest neighbor interactions,  $m_i$  changes abruptly at the domain walls. Almost all sites have  $|m_i| \approx 1$ , which corresponds to completely monocular cells. These domain walls are very similar to the band walls seen in layer 4 of the visual cortex. Unfortunately, nearest neighbor interactions do not generate a regular pattern of bands.

Since domain walls are the natural defects in systems with two degenerate lowest cost states, they are seen in a wide range of systems. Other examples from statistical mechanics the Ising model of uniaxial ferromagnets and the q-state Potts model. A

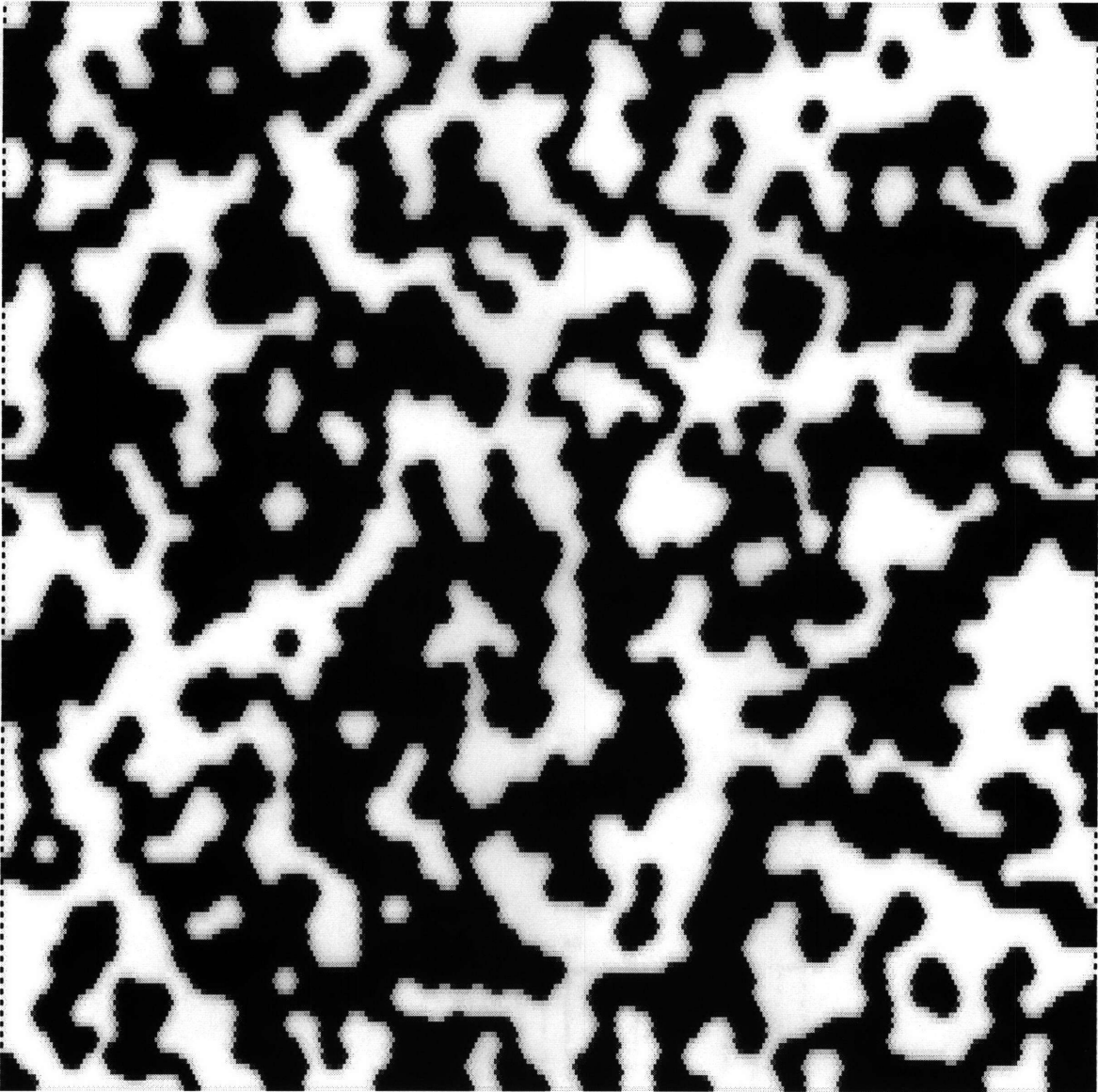


Figure 3-1: Simulated ocular dominance patterns using only nearest neighbor interactions. Dark areas prefer one eye, while light areas prefer the other. Very little grey is apparent indicating few binocular cells. Although domains appear, they do not form stripes with a regular width. As a result of an artifact of the discretization this pattern is metastable and does not coarsen to give a single uniform domain. In this simulation on a  $200 \times 200$  lattice,  $k_s = 0.125$ , and  $\Delta t = 0.05$ . The simulation is interrupted when all  $\Delta m / \Delta t$  becomes less than  $10^{-10}$ .

system as simple as a glass of ice water also has domain walls between the solid and liquid states of water, which at 0° C are degenerate in cost.

### Coarsening

The size of the domains that develop during the critical period is controlled by  $k_s$ . During this period,  $|m_i|$  rapidly increases to a value of 1 as domains form. Increasing the value of  $k_s$  makes sites more strongly influenced by their neighbors and results in larger domains. After this critical period the pattern continues to coarsen on a much longer time scale. Small islands and sharp corners disappear as the system moves toward a uniform state.

Note that the minimum of the cost function is a state in which all  $m_i$  are aligned. An artifact of our discretization causes the pattern to freeze in a metastable state at a higher cost, as shown in Fig. (3-1). In a continuous system islands always shrink, as the boundary can be smoothly deformed inward, slowly lowering the cost of the pattern. In our discrete system on a lattice, small islands still shrink and disappear, but islands above some critical size, controlled by  $k_s$ , remain. (By increasing  $k_s$  sufficiently, this critical size can be made of the same order as the system size, and the finite system coarsens to a single uniform state.) To remove these islands requires temporarily passing through a state of higher cost, which is not allowed by our equations of motion.

It is tempting to use this effect to stabilize patterns of ocular dominance, but this is not in keeping with our macroscopic approach. It relies on a microscopic feature, the discrete nature of the lattice, to control the macroscopic properties. Even though the actual system does in fact have discrete neurons, our coarse grained variable in fact represent many neurons. If we identify each lattice point with a single neuron, we are committed to having them behave and interact like real neurons, performing complicated processing and coupling through tree like arbors of axons and dendrites.

We can remove the metastability by adding noise (effective temperature) that allows the system to pass through patterns of higher cost while evolving toward the lowest state. However, this adds additional complications to the model and may be



difficult to motivate biologically.

### 3.1.3 Long-range Coupling

Many systems in both physics and biology exhibit patterns of stripes. Magnets with dipole interactions, zebras, bird feathers, many species of fish, and even fingerprints all show patterns of stripes. Following the early work by Turing, reaction-diffusion models have been frequently used to model such systems.[47]

The common mechanism (at least in the better understood cases) is a competition between short range attraction and long range repulsion. In the context of the visual cortex this idea was first proposed by Hubel and Wiesel in 1977.[10] Both the short range and the long range interactions cannot be simultaneously satisfied. The best compromise depends both on the relative range and strengths of the interaction and the initial conditions. This randomness in the initial conditions provides the seed for the irregular pattern of branching and bending stripes.

We considered several different interaction forms for the long range coupling. In the simplest interaction form, we add an additional isotropic  $L$ th neighbor coupling leading to,

$$\tau \frac{\partial m_i}{\partial t} = m_i - m_i^3 + k_s^{(1)} \sum_{j \in \text{n.n.}} (m_j - m_i) + k_l^{(1)} \sum_{j \in L\text{th n.n.}} (m_j - m_i), \quad (3.9)$$

where  $k_s^{(1)}$  is the strength of the short range (nearest neighbor) coupling and  $k_l^{(1)}$  is the strength of the long range ( $L$ th neighbor) coupling. To ensure the continuity of the domains,  $k_s^{(1)}$  is positive, while  $k_l^{(1)}$  is negative to cause a periodic alternation of the sign of  $m_i$ .

We also considered a second more general interaction form,

$$\tau \frac{\partial m_i}{\partial t} = m_i - m_i^3 + \sum_j k^{(2)}(i, j)(m_j - m_i), \quad (3.10)$$

where  $k^{(2)}(i, j)$  is a interaction matrix that depends only on the distance between

sites  $i$  and  $j$ ,

$$k^{(2)}(i, j) = \begin{cases} k_s^{(2)} & \text{if } i \text{ and } j \text{ are within } L/2 \text{ sites of each other,} \\ k_l^{(2)} & \text{if } i \text{ and } j \text{ are between } L/2 + 1 \text{ and } L \text{ apart,} \end{cases} \quad (3.11)$$

where  $L$  is the range of the coupling. (As before,  $k_s^{(2)} > 0$  and  $k_l^{(2)} < 0$ .)

We perform the simulations using these long range couplings entirely in real space, rather than Fourier space. In principle, it may be useful to break the equation of motion into two parts: The on-site, including the cubic limiting term, and the short range part of the interaction are calculated in real space, while the long range part of the interaction is calculated Fourier space. The two parts of the equation of motion are then combined with fast Fourier transforms. This may greatly speed calculations that involve many long range interactions. We, however, did not choose to use this route, as most of our simulations have only a limited number of long range interactions.

In the absence of long range couplings, it was necessary to have a positive coefficient on the  $m_i$  term in the equation of motions to ensure that  $m_i = 0$  was not a stable solution. In the presence on long range couplings, this is not necessary, and we find that using a negative coefficient gives better results. Since we implement the long range coupling with a factor of  $k_l(m_j - m_i)$ , a negative value of  $k_l$  results in a sufficiently large positive multiple of  $m_i$  to destabilize the  $m = 0$  solution. With this small change, we implement our long range coupling with discrete time steps. For the coupling in Eq. (3.9),

$$\Delta m_i = \Delta t \left[ -m_i - m_i^3 + k_s^{(1)} \sum_{j \text{ in n.n.}} (m_j - m_i) + k_l^{(1)} \sum_{j \in L\text{th n.n.}} (m_j - m_i) \right], \quad (3.12)$$

and for the coupling in Eq. (3.10),

$$\Delta m_i = \Delta t \left[ m_i - m_i^3 + \sum_j k^{(2)}(i, j)(m_j - m_i) \right] \quad (3.13)$$

where  $\tau$  has been set to 1 in both cases.

## Bands and Their Width

Both forms of interaction result in a pattern of bands with a period of slightly less than  $2L$ , as shown in Fig. (3-2). The period can be estimated by looking at the Fourier transform of the interaction. A peak in the Fourier spectrum indicates a period selected by the interaction. The Fourier spectrum of the first interaction is the difference of two Bessel functions,

$$K^{(1)}(s) = k_s^{(1)} J_0(2\pi s) + k_l^{(1)} L J_0(L2\pi s), \quad (3.14)$$

where the frequency,  $s$ , is measured in inverse lattice points. For a value of  $L = 10$ , as we typically used with  $k_s^{(1)} = -k_l^{(1)}$ ,  $K^{(1)}(s)$  has a peak at approximately  $s = 0.061$  corresponding to a period of 16.4. For the second interaction form, the Fourier spectrum is a bit more complicated,

$$K^{(2)}(s) = k_s^{(2)} \sum_{l=1}^{L/2} l J_0(2\pi l s) + k_l^{(2)} \sum_{l=L/2+1}^L l J_0(l2\pi l s). \quad (3.15)$$

In this case, for a value of  $L = 10$  with  $k_s^{(2)} = -k_l^{(2)}$ ,  $K^{(2)}(s)$  has a peak at approximately  $s = 0.068$ , corresponding to a period of 14.7. In both cases, simulations reveal typical strip widths consistent with these calculations.

Many other interactions with the same typical structure in Fourier space would also result in a pattern of bands. Most reasonable interactions with competing positive short range interactions and negative long range interactions have this property. It is tempting to try to determine the exact shape of the interaction by studying the distribution of excitatory and inhibitory connections on individual cells. However, it is important to distinguish the neural network that mediates the response of V1 from the unknown interaction that directs the formation of the visual cortex. The existing connections in the mature animal are certainly responsible for generating the response at a particular location to stimuli. But, as we wish to study the development of these connections, it is necessary to find the neuro or chemical interaction responsible for developing the observed connections.

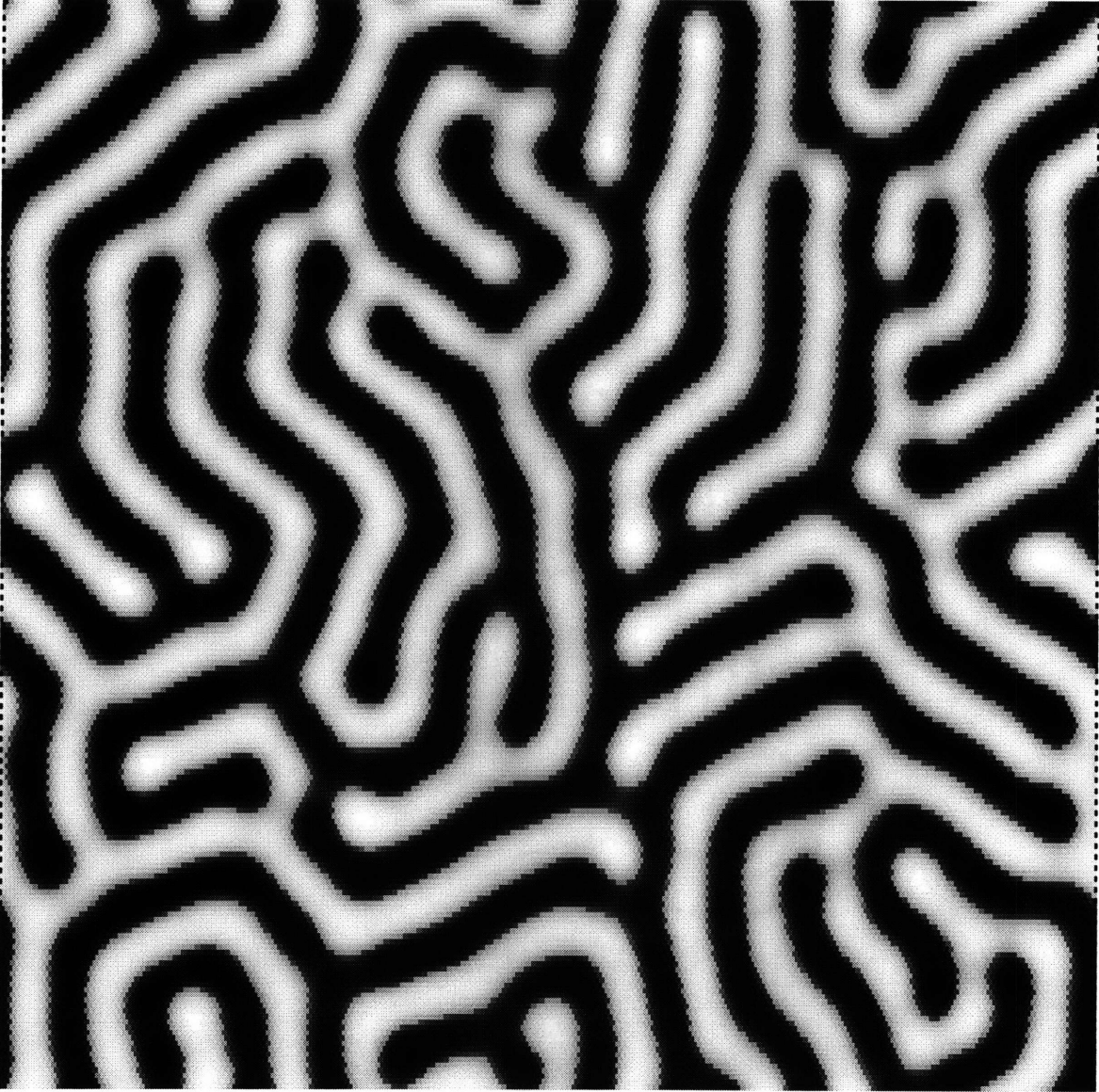


Figure 3-2: Simulated ocular bands generated by iterating Eq. (3.13). (Eq. (3.12) yields very similar patterns.) A totally isotropic interaction is sufficient to form this pattern of bands. In this simulation on a  $200 \times 200$  lattice,  $k_s^{(2)} = 0.05$ ,  $k_l^{(2)} = -0.025$ ,  $\Delta t = 0.025$  and  $L = 10$ . The simulation is interrupted after 40 time constants when the mean value of  $\Delta m / \Delta t$  is less than 0.01.

## Persistence

Persistence is a measure of the internal order of the bands, which includes the density of branches and the straightness of the bands. The persistence of the bands is determined mainly by the long range interaction strength,  $k_l^{(1)}$  or  $k_l^{(2)}$ . The short range interactions mainly influence the roughness of individual domain walls. For extremely weak short range interactions, the domain walls become so rough that the stripes are disturbed and persistence is difficult to measure.

Persistence tends to increase with increasing  $k_l^{(1)}$ , as seen in Fig. (3-3). However, there is a maximum persistence that can be achieved by simply increasing  $k_l^{(1)}$  as is evident in the figure. Patterns with a persistence comparable to that in the monkey can be achieved with a value of  $k_l^{(1)}$  near -0.5. This is based on both visual comparison, and matching the density of branches. The second form for the long range interaction shows similar trends in persistence.

## Edge Effects

Boundary conditions play an important role in the overall appearance of the patterns. The pattern of Fig. (3-2) was generated with periodic boundary conditions in which the sites at one edge connect to the opposite edge. Such boundary conditions are frequently used to reduce edge effects. However, to simulate the whole cortex, open boundary conditions may be more appropriate. For open boundary conditions there are fewer connections for the sites close to edges as they have fewer neighbors. This more accurately reflects the cells near the edge of the primary visual cortex that receive a limited amount of ocular dominance information. Using three methods, we demonstrate that open boundary conditions favor stripes orthogonal to the edges. Fig. (3-4) shows the results of a simulation using open boundary conditions. In addition to direct simulations, we considered the effects of edges by cost function calculations in both the continuous limit of the model, and explicitly on hexagonal lattices.

When considering a continuous system, we assume that some combination of in-

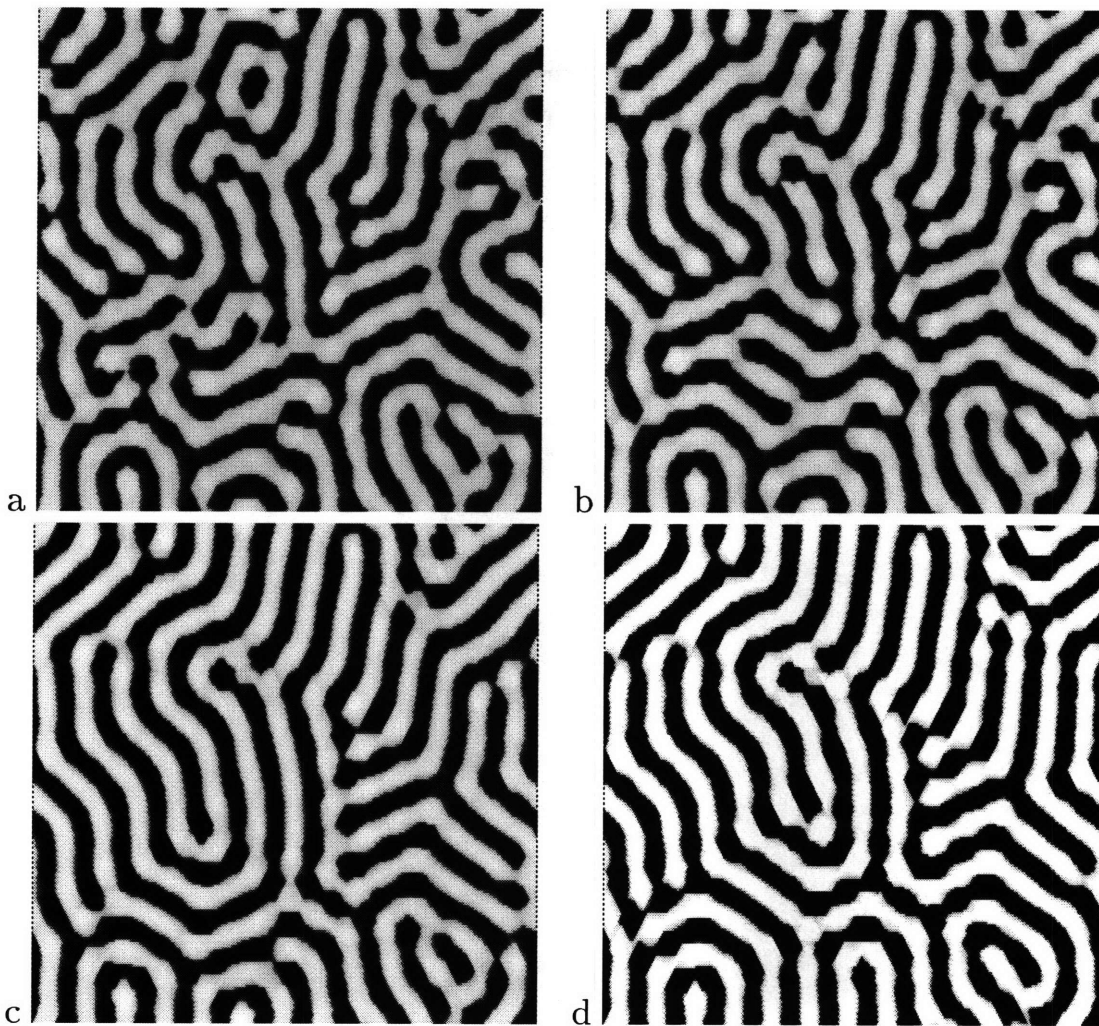


Figure 3-3: Simulated ocular dominance bands according to Eq. (3.12) for a variety of values of  $k_i^{(1)}$  -0.1 (a), -0.15 (b), -0.2 (c), and -0.5 (d). Persistence increases with increasing  $k_i^{(1)}$ , but cannot be strengthened indefinitely. All simulations started from the same initial conditions on a 200 x 200 lattice, with  $k_s^{(2)} = 0.5$ ,  $L = 10$ , and  $\Delta t = 0.05$ . The simulations are interrupted when the mean value of  $\Delta m / \Delta t$  is less than 0.01.

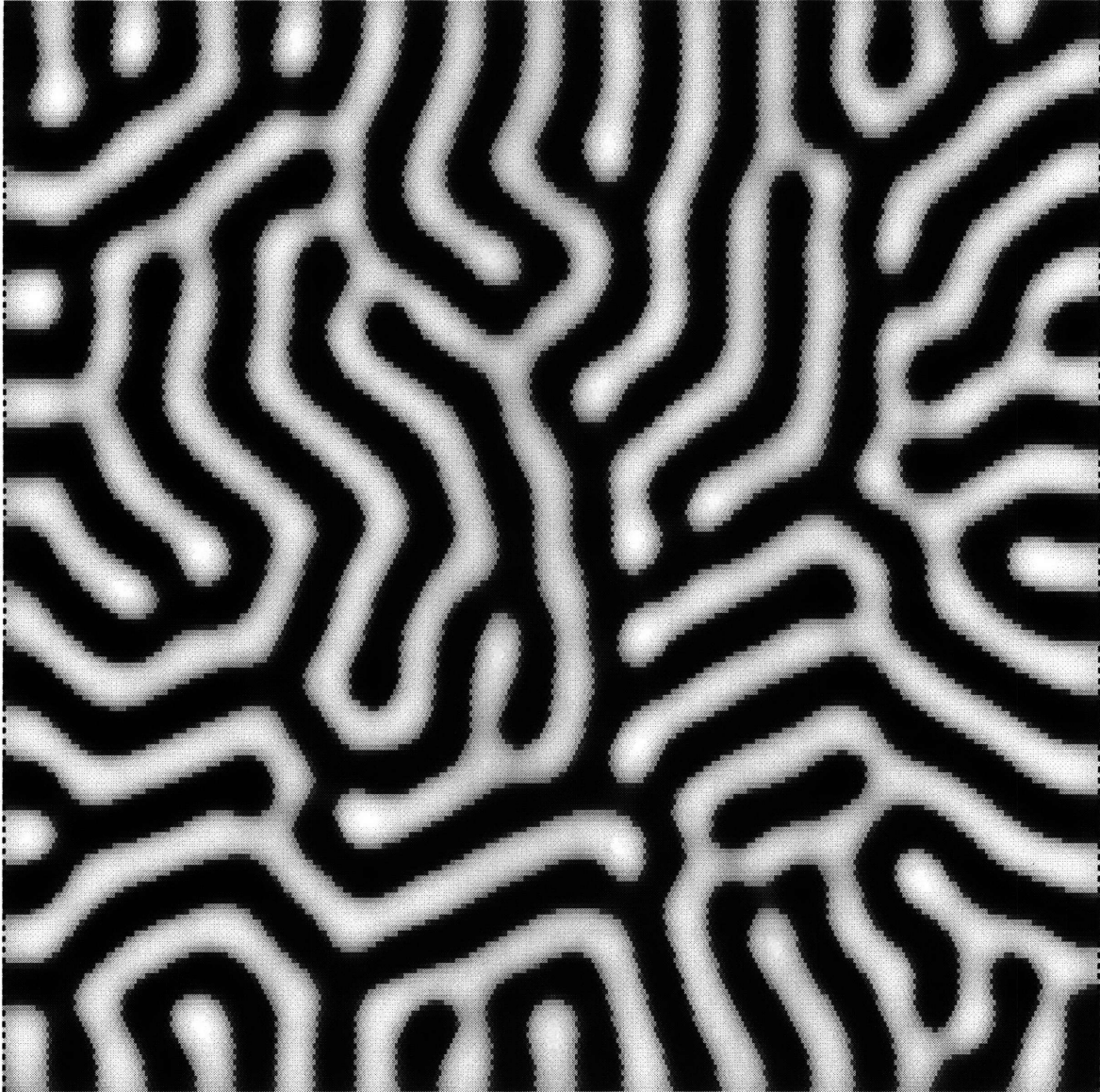


Figure 3-4: Simulated ocular bands generated by iterating Eq. (3.13) with the edges set to  $m = 0$ . Compare with Fig. (3-2) which uses the same initial conditions and parameters but periodic boundary conditions. Note that the bands tend to meet the edges at right angles.

teractions has stabilized a pattern of stripes and consider the effects of the presence of an edge. For simplicity we assume that the stripes have sharp domain walls between bands. We calculate the change in the long range part of the cost function of stripes using a continuous function,

$$F = \int d^2x d^2x' m(\vec{x})m(\vec{x}')\delta(|x - x'| - L), \quad (3.16)$$

where  $L$  is both the range of the long-range interaction, and the width of the stripes. Choose  $m(\vec{x})$  to be a set of straight parallel stripes of width  $L$  ending on the edge at an angle  $\theta$  to the normal, as in Fig. (3-5). Within the stripes, the value of  $m(\vec{x})$  is taken to be  $\pm 1$  with the sign alternating between adjacent bands. The edge is an open boundary with  $m(\vec{x}) = 0$  on the far side. We calculate the per stripe cost of this edge by direct integration,

$$\Delta F_{\text{stripe}}(\theta) = 2L^3 (1 - \sec(\theta) + \theta \tan(\theta)). \quad (3.17)$$

This is related to the energy change per unit length of boundary,  $\Delta F_{\text{edge}}$ , by a factor of  $\cos(\theta)/L$ , yielding

$$\Delta F_{\text{edge}} = 2L^2 (\cos(\theta) - 1 + \theta \sin(\theta)). \quad (3.18)$$

Both forms of the energy change have a minimum at  $\theta = 0$ , which corresponds to stripes perpendicular to the wall, as in Fig. (3-6).

We performed the same calculation on a hexagonal lattice with stripes of width 10 lattice points. The results are compared to the continuous calculation in Fig. (3-6). Small differences arise due to the discrete nature of the lattice, but the general form of the angular dependence is clearly similar. Using the discrete lattice, we also calculated the cost of the nearest neighbor interaction, and confirmed that it contributes much more weakly to the angular dependence than the long range part.

We examined the difference in the bulk energy between stripes at different angles relative to the lattice, as shown in Fig. (3-7). The changes in energy due to alignment



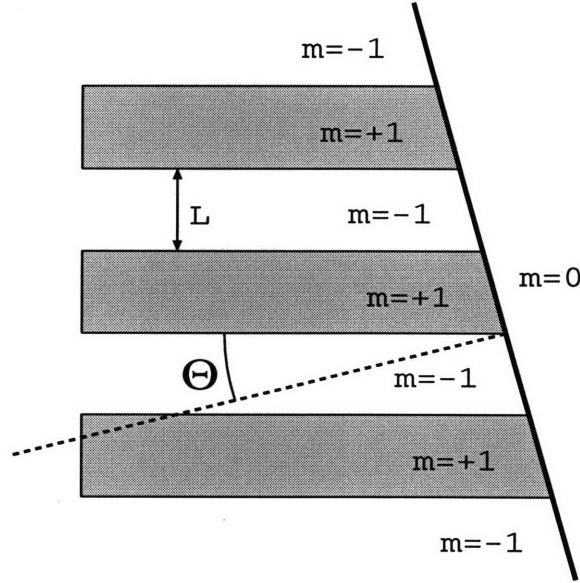


Figure 3-5: Alternating stripes of positive and negative ocular dominance ( $m = \pm 1$ ) with width  $L$  meet an  $m = 0$  half plane at an angle  $\theta$  to the normal.

with the lattice are small. However, there is a remaining artifact in a cost advantage to aligning with one of the six primary lattice directions. This effect has also been seen in simulations, as the bands have a tendency to orient with one of these directions.

### Monocular Deprivation

In monocular deprivation experiments, one eye is closed or otherwise inhibited during some part of development. If this occurs during the critical period of early development, ocular dominance begins to favor the open eye. This observation is consistent with a Hebbian learning algorithm which relies on correlation in activity to strengthen synapses. Synapses corresponding to the closed eye are not strengthened frequently, creating a preference for the open eye.

We can model monocular deprivation by adding a bias term to the equation of motion,

$$\tau \frac{\partial m_i}{\partial t} = m_i - m_i^3 + \sum_j k_{ij}(m_j - m_i) + H(t), \quad (3.19)$$

where  $H(t)$  is the strength of the preference caused by monocular deprivation, which could in principle depend on time, and  $k_{ij}$  is the total interaction matrix that may

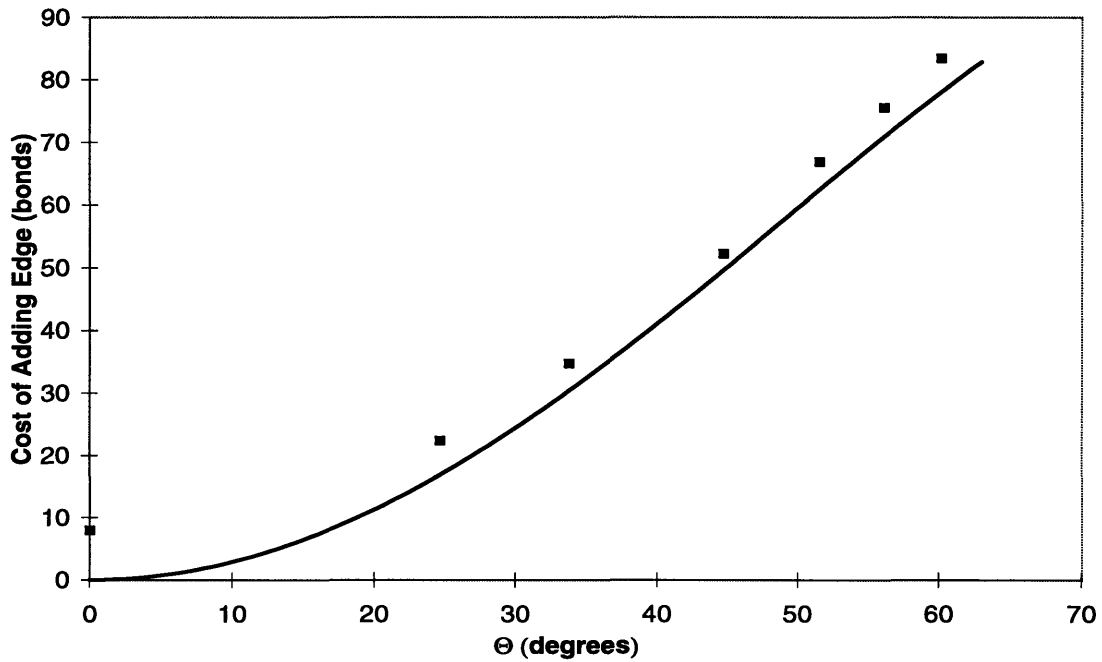


Figure 3-6: The cost of an edge intersecting stripes at an angle  $\theta$  to the normal. The cost is given per unit length of the edge. The solid line is a calculation for a continuous system, while the squares are from a discrete model on a hexagonal with a stripe width of 10 sites. In both cases the interaction occurs at the same range as the stripe width.

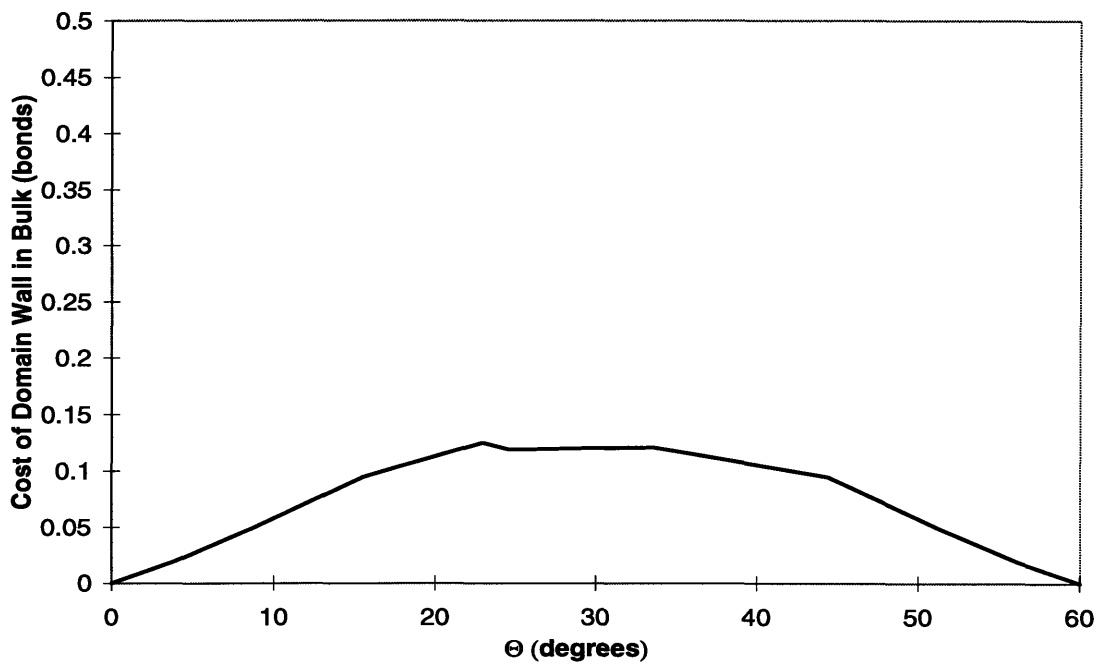


Figure 3-7: The cost of stripes in the bulk as a function of the angle between the stripes and the underlying hexagonal lattice. The cost repeats with a period of  $60^\circ$  and has a minimum at 0 where the stripes are aligned with the lattice. The calculation is performed on a discrete system with a stripe width of 10 sites.

take either of the forms in Sec. (3.1.3). In the Landau-Ginzburg language,  $H(t)$  is a symmetry breaking field that prefers one eye.

This symmetry breaking reproduces some features of monocular deprivation. If the field is applied early in the simulation, it results in a preference for one eye over the other, while if applied in the later stages, it has little or no effect. Like monocular deprivation, it is effective only during a critical period. However, this interaction does not reproduce the observed pattern of alternating narrow and wide bands. Instead, a pattern forms with islands of the deprived eye appearing in a sea of the dominate eye, as seen in Fig. (3-8). The typical width of features for both eyes remains constant, while the overall area covered by the deprived eye is reduced by an amount depending on the  $|H(t)|$ . For sufficiently large values of  $|H(t)|$ , the symmetry breaking field dominates and a uniform pattern results.

The effect of a uniform field may be more easily understood in one dimension. Since it is very easy to determine the width of the stripes in a pattern in one dimension, we can examine the distribution of stripe widths. With  $H(t) = 0$ , the distribution of stripe widths is identical for both eyes. In the monkey, stripes of the deprived eye are narrowed so that their distribution shifts to the left, while that of the other eye shifts to the right. In our model, however, the peak of the distributions remains fixed as shown in Fig. (3-9). The stripes anti-aligned with the field tend to have the same width but become fewer in number. The stripes aligned with the field do show a tendency to have increased width, but the distribution of widths becomes wider, not simply shifted to longer lengths.

### 3.1.4 Distribution of $|m_i|$

The narrow interaction form given in Eq. (3.12) produces stripes with sharp domain walls, and a narrow distribution of  $|m_i|$ . This corresponds well with the observed behavior in layer IV. Here the domains do seem to change abruptly at the walls with a very narrow crossover. Almost all the cells are monocular, meaning that  $|m_i|$  should be sharply peaked at its maximum value.

The wider interaction form given by Eq. (3.13) produces smoother domain walls

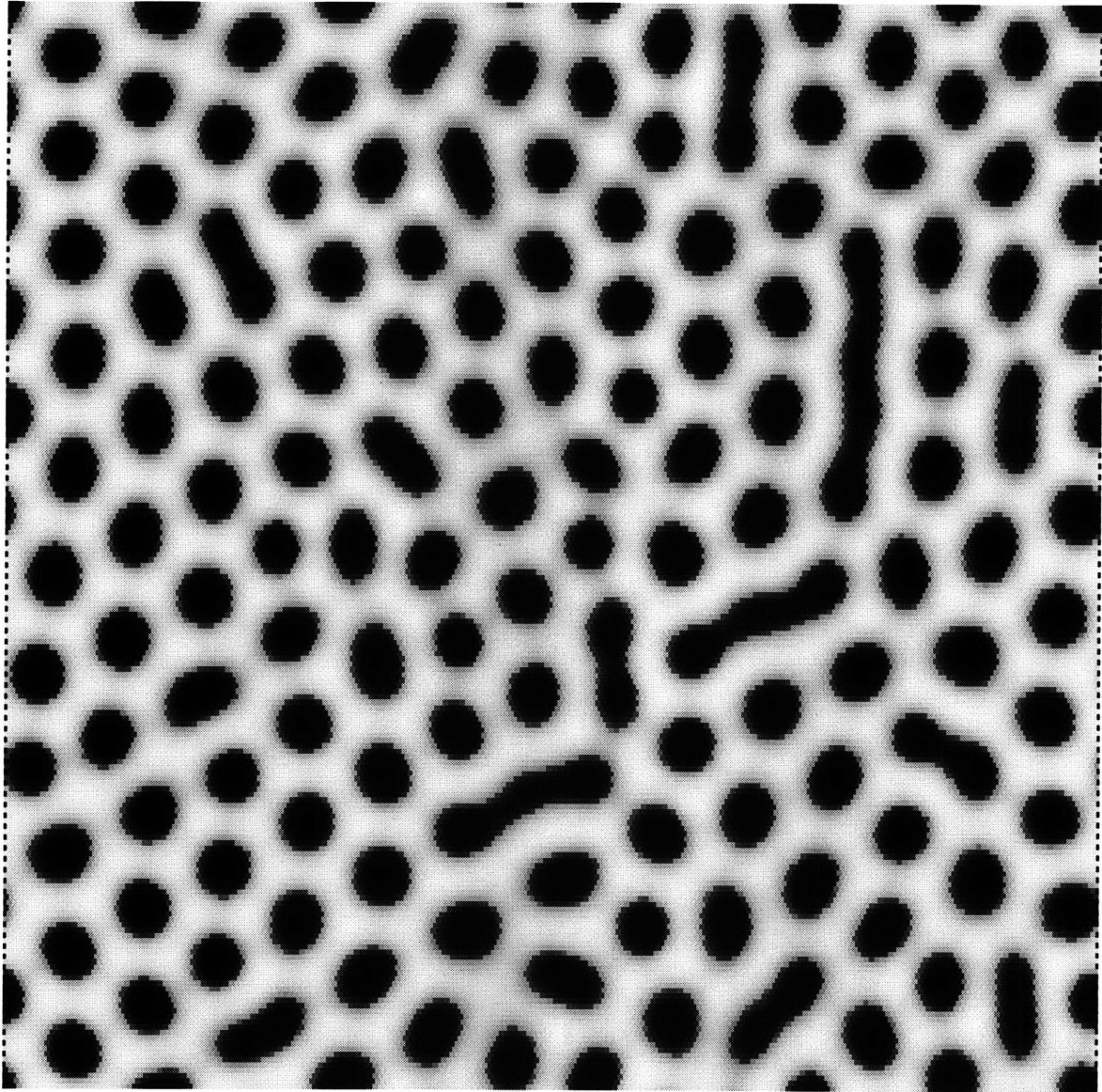


Figure 3-8: A simulation of monocular deprivation by including a uniform field of  $H = 3.5$ . Compare this figure with Fig. (3-2) which uses the same initial conditions and parameters, but has  $H = 0$ .

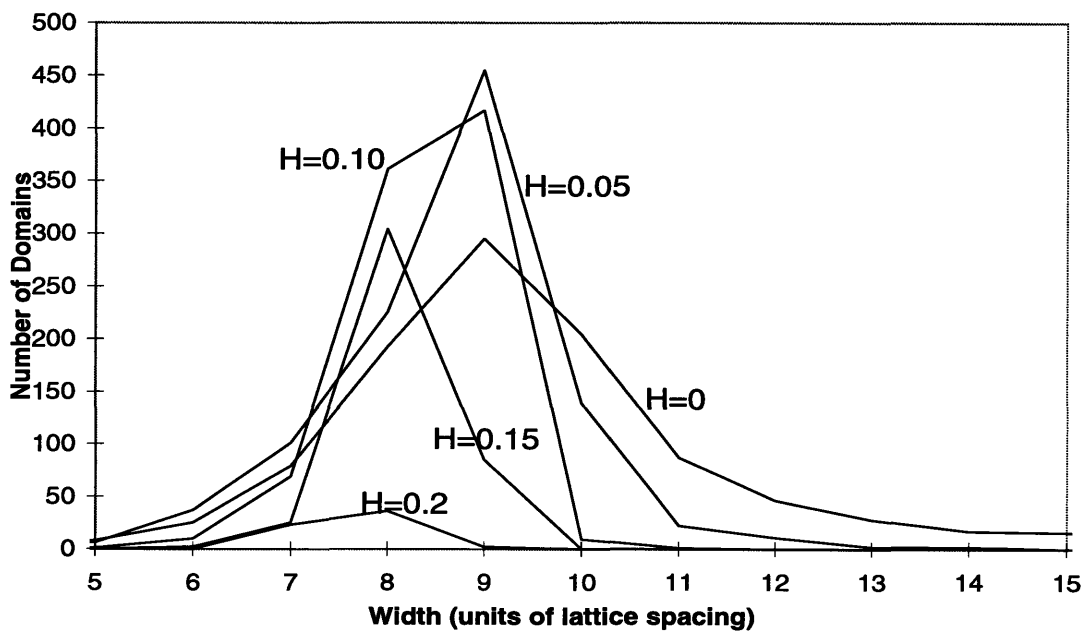


Figure 3-9: The distribution of the widths of the repressed in a one dimensional simulation for several value of  $H$ . Notice that the peak of the distribution remains fixed. Here  $L = 10$ ,  $k_s^{(2)} = 0.1$ ,  $k_l^{(2)} = -0.1$ , and  $\Delta_t = 0.1$ .

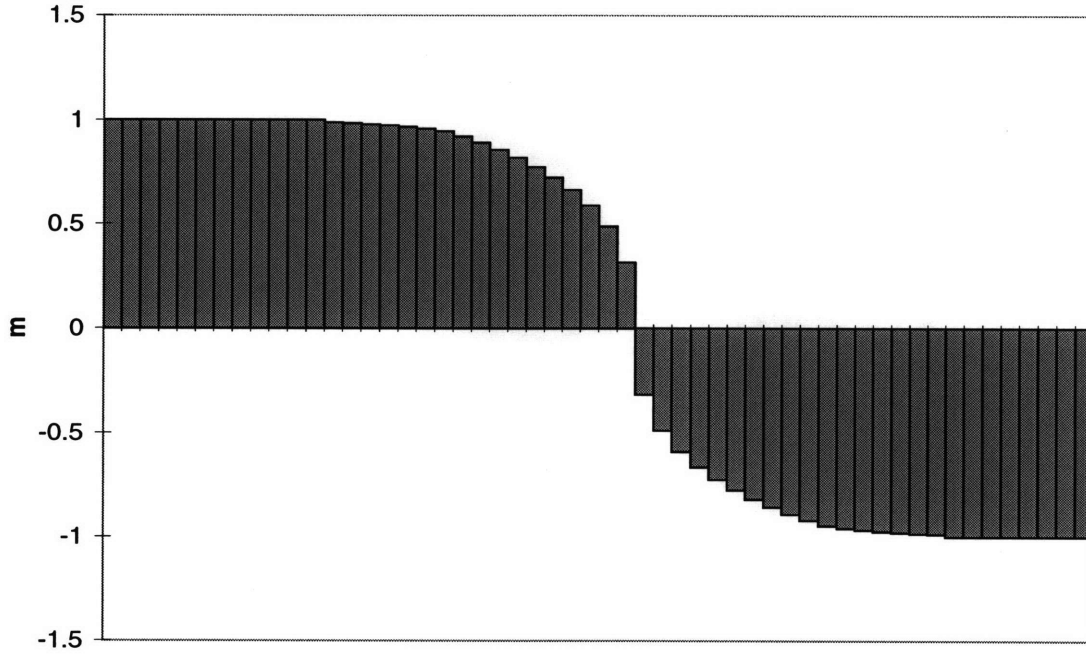


Figure 3-10: The profile of a domain wall in one dimension. The field evolved according to Eq. (3.13) with  $L = 20$ ,  $k_s^{(2)} = 0.05$ , and  $k_l^{(2)} = 0$ . The presence of the domain wall was forced by keeping the left edge at  $m_i = +1$  and the right edge at  $m_i = -1$ .

and a correspondingly wider distribution of  $|m_i|$ . This case better matches the behavior seen in all the layers except layer 4. There are, however, still significant differences. Experimental observations suggest that  $m$  changes linearly near the domain wall, while the wide interaction form results in domain walls that always include a discrete jump as in Fig. (3-10).

The discrete jump can be studied on one dimension. The width of the domain wall scales linearly with the range of the interaction but a discontinuity remains even for very long range interactions, as seen in Fig. (3-11). The discontinuity originates from the non-linear terms in the equation of motion. For small values of  $m_i$ , an interaction that generates a desired domain wall shape can be found from the Fourier transform of the domain wall. However, for large values of  $m_i$ , the cubic term in the equation

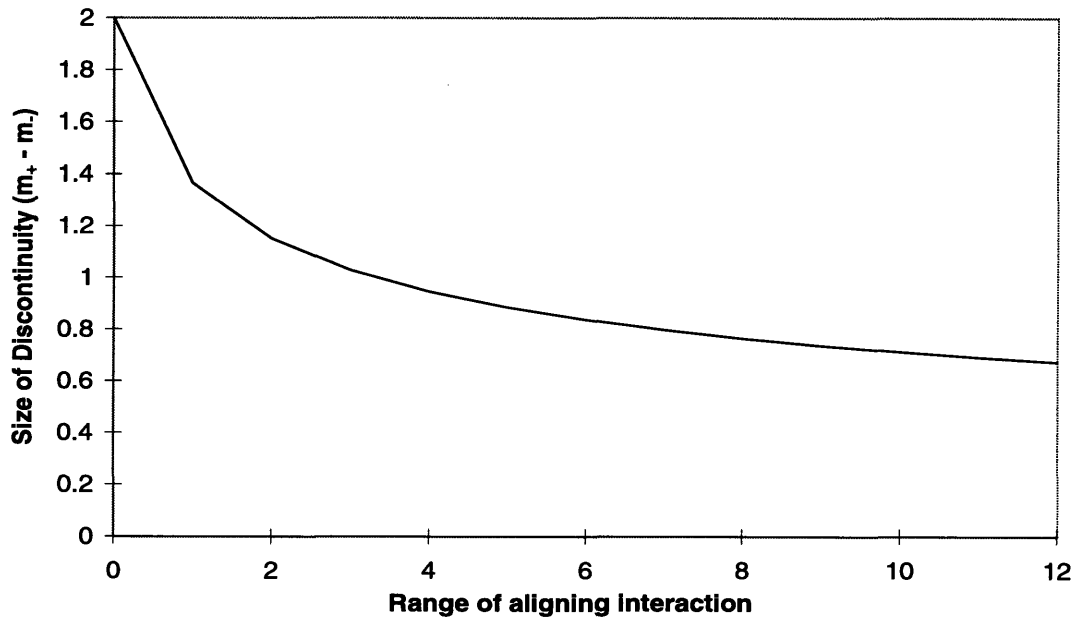


Figure 3-11: The discontinuity in  $m_i$  at the domain wall in a one dimensional simulation as a function of the range of the positive interactions. The size of the discontinuity is expressed as a fraction of the value in the bulk. Notice that a finite jump continues to exist even for very long range interactions.

of motion begins to have a dominant role and the linear approximation necessary for the Fourier transform no longer holds. Despite the presence of the discontinuous jump at the domain wall, the wide interaction form still models non-layer IV ocular dominance well. It produces a wide distribution in  $m_i$  as is observed, as indicated in Fig. (3-12). Unfortunately, the exact shape of the experimental distribution is not known.

### 3.1.5 Summary

The patterns produced by our equations of motion, accurately reproduce many of the desired features of ocular dominance. Competition between short-range and long-



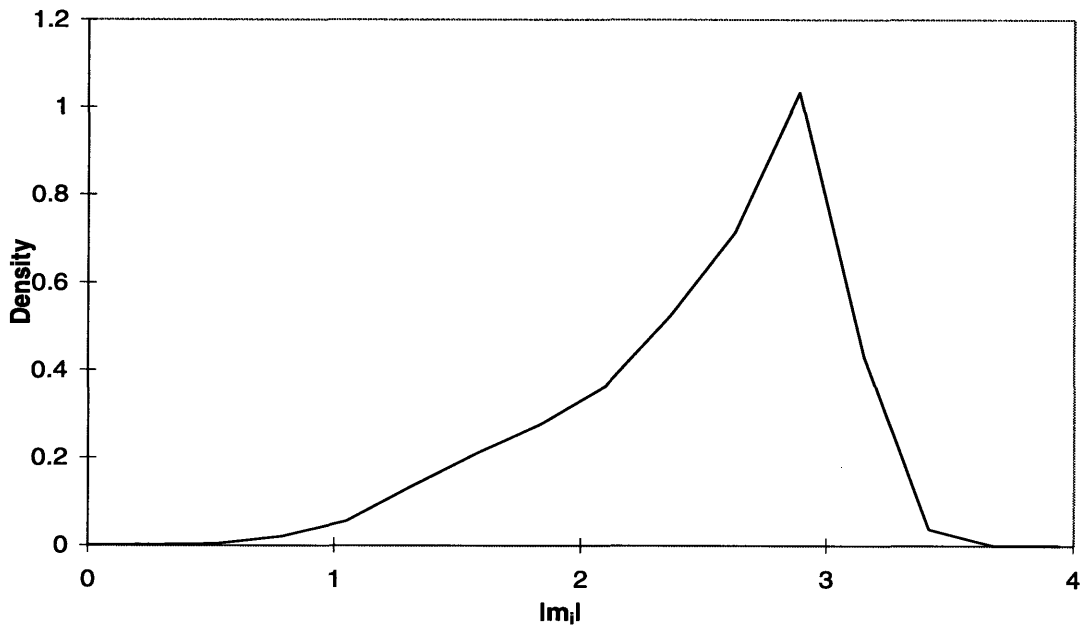


Figure 3-12: A typical distribution of  $|m_i|$  for a two dimensional simulation using Eq. (3.13). The distribution shown corresponds to Fig. (3-2).

range coupling produces a meandering, branching pattern of bands. The width of the bands is determined primarily by the range of the interactions, while the relative strengths of the short and long range coupling can be adjusted to achieve a persistence similar to that seen in the monkey. Open boundary conditions naturally cause the stripes to meet edges at right angles. The stripes appear during a critical period of development during which they are sensitive to an applied field representing monocular deprivation. After this critical period, the pattern is stable to small perturbations. The domain walls and distribution of  $m_i$  seen in our simulation are quite similar to those in layer 4. The domain walls are sharp and narrow, i.e. the distribution of  $|m_i|$  is narrowly centered around the maximum possible value, a completely monocular response.

The equations of motion cannot be easily modified to model layers other than 4. Outside layer 4, the distribution of  $|m_i|$  is wide extending down to 0, and the domain walls are wide and smooth. Our simulated domains always have a discontinuity, and although we can widen the distribution of  $|m_i|$  we cannot achieve any significant number of binocular cells. Furthermore, in our equations we make no attempt to model the growth of the cortex or the tendencies seen in LeVay's patterns for stripes to align in prescribed directions.

### 3.2 Orientation Preference and Selectivity

We next use the Landau-Ginzburg approach to develop a macroscopic model for orientation preference and selectivity patterns. In the monkey the orientation pattern is marked by pinwheels, areas that respond similarly to all orientations. Different possible orientation preferences circulate around these singularities. The two possible directions of circulation give two types of pinwheels which occur in equal numbers. The patterns develop during a critical period during which they are sensitive to outside perturbations. The density of pinwheels remains constant during the later parts of the critical period (the only observable period of development), despite the growth of the cortex.

### 3.2.1 Local Variables and the Cost Function

We use a complex field,  $z(\vec{x})$ , to model the orientation preference and selectivity. The orientation preference is given by half the complex angle, since it repeats with a period of  $180^\circ$ . It is necessary to divide the angle by two, rather than take the complex angle modulus  $180^\circ$ , to ensure that the singularities in the model are surrounded by one complete cycle of orientations, and not two. The magnitude of the complex field,  $|z(\vec{x})|$ , is a measure of the selectivity. From the outset we assume a discrete lattice and label  $z(\vec{x}_i)$  with  $z_i$  for each lattice point  $\vec{x}_i$ .

We construct a local cost function  $F(z_i)$  by considerations similar to those in Sec. (3.1.1). Because there is no a priori reason to distinguish between different orientations, the cortical cost function must be only a function of  $|z_i|$ . However, a function involving odd powers of  $|z_i|$  is not smooth around  $z_i = 0$  and is not a good candidate for a cost function. Thus,  $F(z_i)$  is a series in  $|z_i|^2$ ,

$$F(z_i) = a'_2|z_i|^2 + a'_4|z_i|^4 + \dots, \quad (3.20)$$

where  $a'_2$ ,  $a'_4$ , etc. are, as of yet, arbitrary constants.

As in our model for ocular dominance, choosing  $a'_2 < 0$  and  $a'_4 > 0$ , and setting all other coefficients zero, results in a minimum cost for a finite, non-zero value of  $|z_i|$ . With only local interactions, each site is completely independent. A steepest descent minimization of the cost function gives an equation of motion for each  $z_i$ ,

$$\tau' \frac{\partial z_i}{\partial t} = -\frac{\partial F(z_i)}{\partial z_i} = -2a'_2 z_i - 4a'_4 z_i |z_i|^2, \quad (3.21)$$

where  $\tau'$  reflects the rate at which the system relaxes.

The coefficients,  $a'_2$  and  $a'_4$ , can be absorbed into  $m$  and  $\tau$  by appropriately changing units,

$$\tau' \frac{\partial z_i}{\partial t} = z_i - z_i |z_i|^2. \quad (3.22)$$

In this form an unstable fixed point at  $z_i = 0$  and stable fixed points at  $|z_i| = 1$  become obvious. These local terms result in orientation preference, although without

any coupling between sites we cannot hope to generate the desired patterns.

### 3.2.2 Short-range Coupling

Including nearest neighbor coupling between adjacent sites results in,

$$\tau' \frac{\partial z_i}{\partial t} = z_i - z_i |z_i|^2 + \sum_{j \in \text{n.n.}} k'_{ij} (z_j - z_i), \quad (3.23)$$

where  $k'_{ij}$  is the interaction matrix. The requirements of translationally invariance and isotropy lead to,

$$\tau' \frac{\partial z_i}{\partial t} = z_i - z_i |z_i|^2 + k'_s \sum_{j \in \text{n.n.}} (z_j - z_i). \quad (3.24)$$

Again, the coupling between adjacent sites,  $k'_s$ , must be positive to ensure the continuity of domains.

#### Implementation

We simulate orientation preference using discrete time steps on a hexagonal lattice, in much the same way as ocular dominance. We use a discrete equation of motion

$$\Delta z_i = \Delta t \left( z_i - z_i |z_i|^2 + k'_s \sum_{j \in \text{n.n.}} (z_j - z_i) \right), \quad (3.25)$$

where  $\Delta z_i$  is the discrete change in  $z_i$  and  $\Delta t$  is the time step. The time constant  $\tau'$  has been set to one for convenience.

The exact distribution of orientation preference and selectivity at early stages of development is not known. The most reasonable assumption is a uniform distribution of angles. Experiments also show that selectivity is lower in immature animals. To model this distribution, we assume initial conditions for  $z_i$  that are uniform on the complex angle with a fixed magnitude that is small, typically  $|z_i| = 0.1$ . (It is likely that the initial magnitude is also distributed over some range, but as there is little information on this, and the final results are not affected, we choose to simply use a

single value.)

We performed simulations with both periodic and open boundary conditions. Because of the short-range nature of the interactions, the boundary conditions do not seem to play a significant role. There is experimental evidence that orientation continues smoothly from area V1 to neighboring area V2, suggesting that periodic boundary conditions are not entirely inappropriate.

### **Vortices as Defects**

During the simulation, orientation preference rises quickly for several time constants until it approaches a maximum value of approximately of 1. These first few time constants form a critical period where the field is sensitive to small perturbations. Fig. (3-13) shows the pattern of orientation that develops, which is marked by singularities called vortices.

These vortices are topological defects that correspond to the pinwheels observed experimentally. They are points of reduced selectivity surrounded by regions responding to all possible orientations. Vortices are well defined topological features, that can be detected by adding together the changes in angle preference around a closed loop. If this sum is  $\pm 180^\circ$ , a vortex is enclosed in the loop. The vortex has a circulation of  $\pm 1$  depending on sign of the sum. A loop enclosing two similar vortices gives a sum of  $\pm 360^\circ$ , while a loop enclosing two opposite vortices yields a sum of  $0^\circ$ . Our simulations give an equal number of both circulations of vortices in agreement with experiment.

Since vortices are the natural defects in angular fields it is not surprising that they are generated by a wide variety of apparently disparate models. Any model that gives adequate attention to the angular nature of the orientation pattern will generate vortices. Most previous models have not addressed the annihilation of vortices, which we discuss in the following sections.

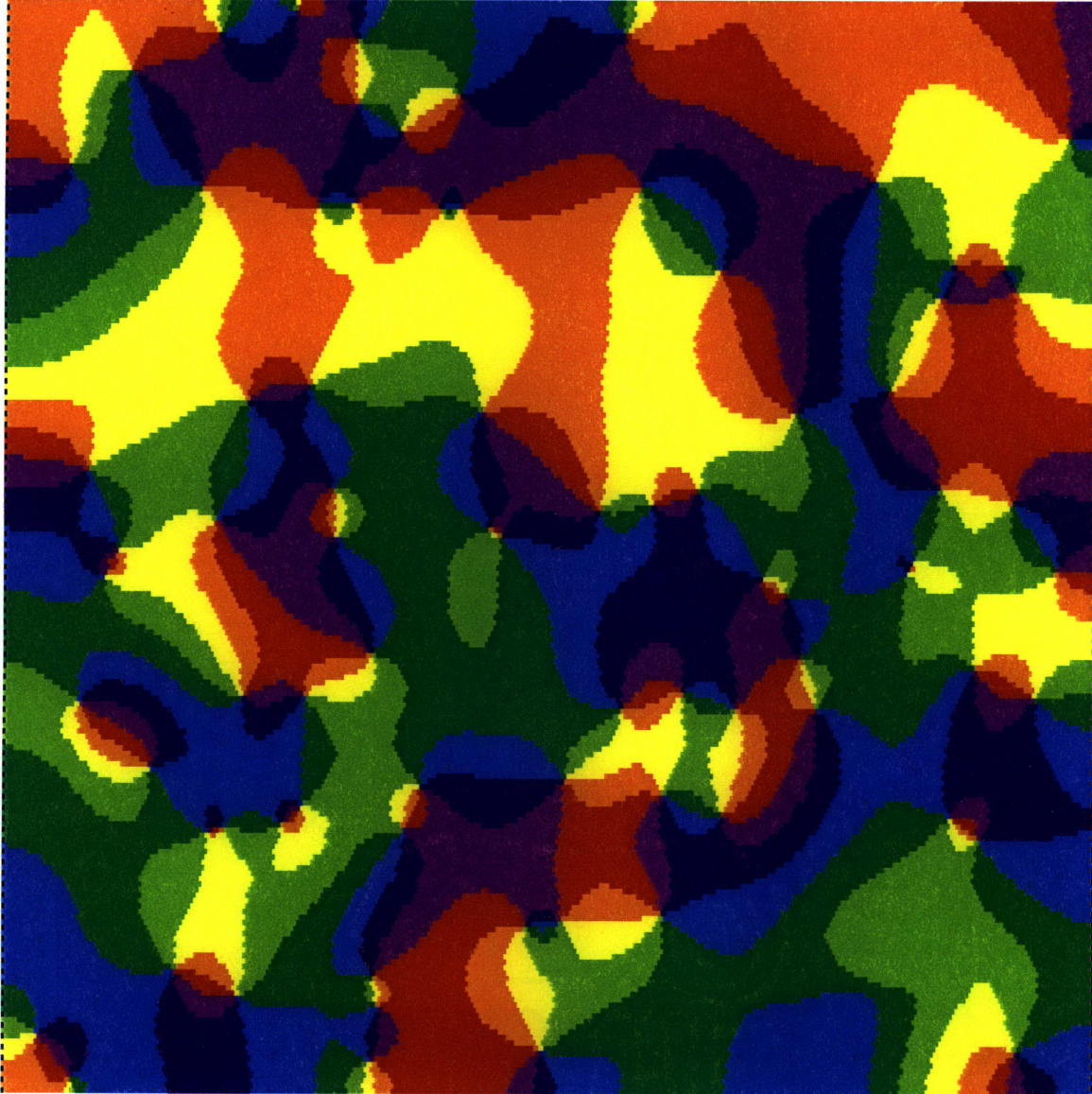


Figure 3-13: Simulated orientation pattern generated by iterating Eq. (3.25). Each of the 8 colors shown represents a range of  $22.5^\circ$ . The colors cycle through  $180^\circ$  of preference, light green  $\rightarrow$  yellow  $\rightarrow$  orange  $\rightarrow$  red  $\rightarrow$  violet  $\rightarrow$  dark blue  $\rightarrow$  light blue  $\rightarrow$  dark green  $\rightarrow$  light green  $\rightarrow$  etc. In this simulation on a  $200 \times 200$  lattice,  $k'_s = 0.125$  and  $\Delta t = 0.05$ . The simulation is interrupted after 50 time constants.

## Coarsening

The pattern of vortices resembles those seen experimentally. However, the density of vortices does not remain constant. Vortices of opposite circulation attract and annihilate as the simulation proceeds, as shown in Fig. (3-14). This takes place on a much longer time scale than the initial formation of vortices. Eventually, all the vortices annihilate leaving a single uniform orientation. This is in sharp contrast to the experimental observations where the vortex concentration remains constant. As the cortex grows by 16%, this means that the number of vortices increases rather than decreases.

The ground state, absolute minimum of the cost function, occurs when all sites have the same orientation. Since the cost is independent of orientation, this ground state is highly degenerate. Vortices are the natural defects in this angular field. They arise because the short-range interactions allow separated regions to relax independently. Each region moves to one of the degenerate ground states that was favored locally by the initial conditions. Domain walls usually do not form between these different regions as adjacent “domains” can be smoothly deformed into each other. Vortices, however, are topological defects and cannot be removed by smoothly changing the field.

Vortices of opposite circulation experience an effective attraction. This attraction causes the vortices to move toward each other, collide, annihilate in pairs, and slowly reduce their density. In this manner the pattern continues to coarsen and evolve toward a true ground state.

### 3.2.3 Long-range Coupling

Long range couplings, which stabilized the pattern of ocular dominance, are not as useful for fixing the pattern of orientation preference. Including the simplest possible long range interaction,

$$\tau' \frac{\partial z_i}{\partial t} = z_i - z_i |z_i|^2 + k'_s \sum_{j \in \text{n.n.}} (z_j - z_i) + k'_l \sum_{j \in \text{Lth n.n.}} (z_j - z_i), \quad (3.26)$$



Figure 3-14: The same simulated orientation pattern shown in Fig. (3-13) but after 250 time constants. The number of vortices is greatly reduced. The vortices shown eventually annihilate after additional iterations.



with  $k'_i < 0$  does not lead to a finite density of vortices. This is because the cost function associated with this equation of motion can be minimized without any vortices, by creating a rainbow pattern of orientations, as shown in Fig. (3-15). This pattern resembles a series of orientation bands, that were once conjectured but are not seen experimentally. We also checked several wider interaction forms, similar to Eq. (3.26). All of these failed to prevent the collapse of vortices.

Long range interactions which are linear in  $z_i$  do not directly act on singularities, which are zeros in  $|z_i|$ . It may be possible to create an interaction that causes the distances between singularities to favor a particular non-zero length. We investigated this possibility by considering higher order interactions, such as

$$\tau' \frac{\partial z_i}{\partial t} = \dots + z_i \sum_j k''_{ij} |z_j|^2 + \sum_j k'''_{ij} z_j |z_j|^2 + \dots \quad (3.27)$$

However, we concluded that this approach is not promising and did not investigate it extensively.

### 3.2.4 Distribution of $|z_i|$

Our model for orientation preference generates patterns similar to those found experimentally. However, the selectivity is not modeled well. The experimentally observed selectivity has a wide distribution, with large areas of reduced selectivity surrounding each pinwheel. Our model gives nearly uniform selectivity of 1 as seen in Fig. (3-16). While selectivity is zero at the singularities, the reduction extends only to a few adjacent lattice sites.

By coupling to a quenched random field, the distribution of selectivity can be widened. A quenched random field can be motivated as arising from two possible mechanisms. One motivation comes from fluctuations in the density or computational effectiveness of neurons. Small fluctuations in density have been observed in the cortex, and might reasonably be considered as uncorrelated. Fluctuations in computational effectiveness have not been studied in the monkey, but are a reasonable assumption considering the variety of different types of neurons present. A second

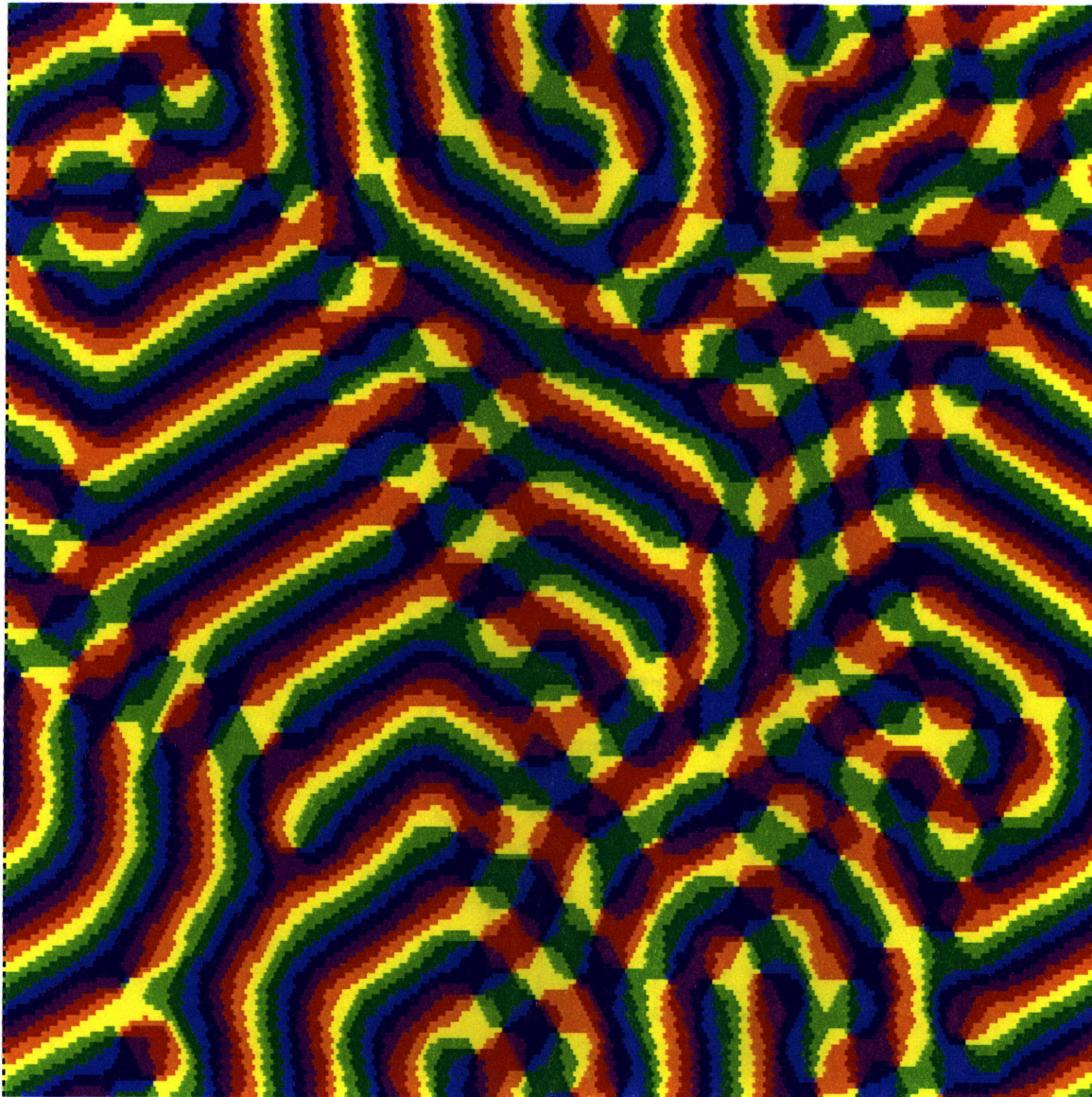


Figure 3-15: Simulated orientation pattern generated by iterating Eq. (3.26). The long-range coupling does not stop the annihilation of vortices but rather causes the formation of rainbow-like bands. In this simulation on a  $200 \times 200$  lattice,  $k'_s = 0.1$ ,  $k'_l = -0.01$ , and  $\Delta t = 0.1$ . The simulation is interrupted after 100 time constants.

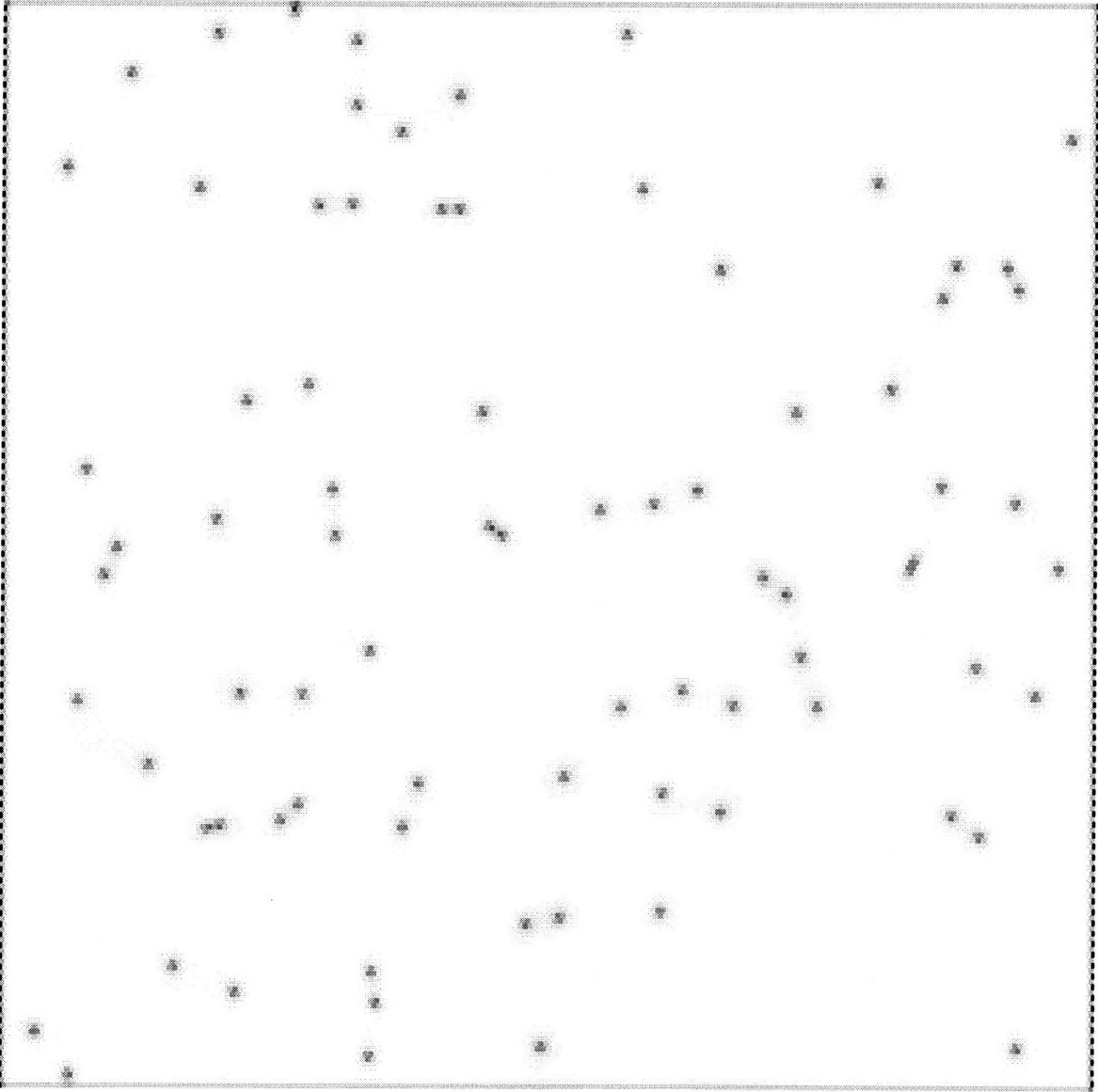


Figure 3-16: Simulated selectivity pattern corresponding to Fig. (3-13). Darker areas are less selective, i.e. have lower values of  $|z_i|$ .

motivation comes from the coupling between a number of other fields which might contain information about color, texture, motion, or other properties. Coupling to a large number of unknown fields, can be represented by a single uncorrelated random field. The possibility of coupling between a small number of correlated fields is discussed further in Sec. (3.3).

A random field that represents density fluctuations or the computational demands of many other fields, is better represented by a real number, rather than a complex number which also contains angular information. (A complex random field may be motivated by considering coupling to vector fields, e.g. direction of motion. However, unless the net effect of a large number of vector fields is being considered, this field would not be random, but highly correlated with its own equations of motions.) In the context of phase transitions in magnets, a field appears as an addition to the equations of motion, such as  $H(t)$  in Eq. (3.19). Here, we use the term loosely, referring to a set of random parameters,  $\{h_i\}$ , multiplying the orientation order parameter  $\{z_i\}$ . More correctly in the magnetic context, this is a random energy term. We thus consider the modified equation,

$$\tau' \frac{\partial z_i}{\partial t} = z_i - z_i |z_i|^2 + k'_s \sum_{j \in \text{n.n.}} (z_j - z_i) + h'_i z_i. \quad (3.28)$$

The local fixed points of this equation of motion can be studied by looking at each location independently,

$$\tau' \frac{\partial z_i}{\partial t} = z_i - z_i |z_i|^2 + h'_i z_i. \quad (3.29)$$

In the presence of a random field  $h'_i$ , the preferred local magnitudes of  $|z_i|$  are changed to  $\sqrt{1 + h'_i}$

It is difficult to biologically motivate the distribution of  $h'_i$ , as we have not specifically identified the processes generating the random field. If the randomness is the result of the sum of many other fields,  $h'_i$  may be normally distributed. However, if the randomness arises from structural fluctuations in the cortex, the distribution may have some other shape. We use a uniform distribution for convenience, but there is no reason to believe that other distributions of  $h'_i$  will give qualitatively different

results.

Coupling to randomness widens the distribution of  $|z_i|$  so that extends to zero. However, the amount of randomness required to give a distribution similar to the experimentally observed ones disrupts the overall pattern of selectivity. The experimental patterns have smoothly varying selectivity that is reduced in regions around singularities, while our simulated pattern, shown in Fig. (3-17), is dominated by the random field itself. We have included only nearest neighbor couplings in our simulations. Using longer range coupling may increase the size of the vortices and reduce the impact of the random field on the selectivity pattern.

Coupling orientation to a random field provides a promising method for stabilizing the singularities. This approach is analogous to the pinning of vortices by defects in superconductors. Fig. (3-18) shows a stable pattern of vortices. The vortices become trapped, or pinned, in local minima of the random field. A sufficient amount of randomness creates a pattern of vortices that appears to be stable over long time scales. Smaller amounts of randomness slow, but do not prevent, the pair annihilations.

Although we choose only to investigate the effects of a random field, random couplings generate many of the same effects. Random couplings may reflect fluctuations in the ease with which synapses are formed between pairs of cells. The size, orientation, and exact position of cells are likely to effect their ability to form synapses with other nearby cells. This type of interaction may be modeled by adding random fluctuations,  $\delta'_{ij}$ , to  $k'_{ij}$ .

### 3.2.5 Summary

A simple equation of motion for a complex field involving only nearest neighbor couplings generates a pattern containing vortices which we identify with the pinwheels in the experiments. The vortices have circulations of  $\pm 180^\circ$  in equal ratios as desired. The vortices are formed during a critical period during which the field is sensitive to perturbations. Coupling with a quench random field, representing other fields or density fluctuations, can pin the vortices, stabilizing the pattern.

Our simulations give distribution of  $|z_i|$  that are much narrower than desired,

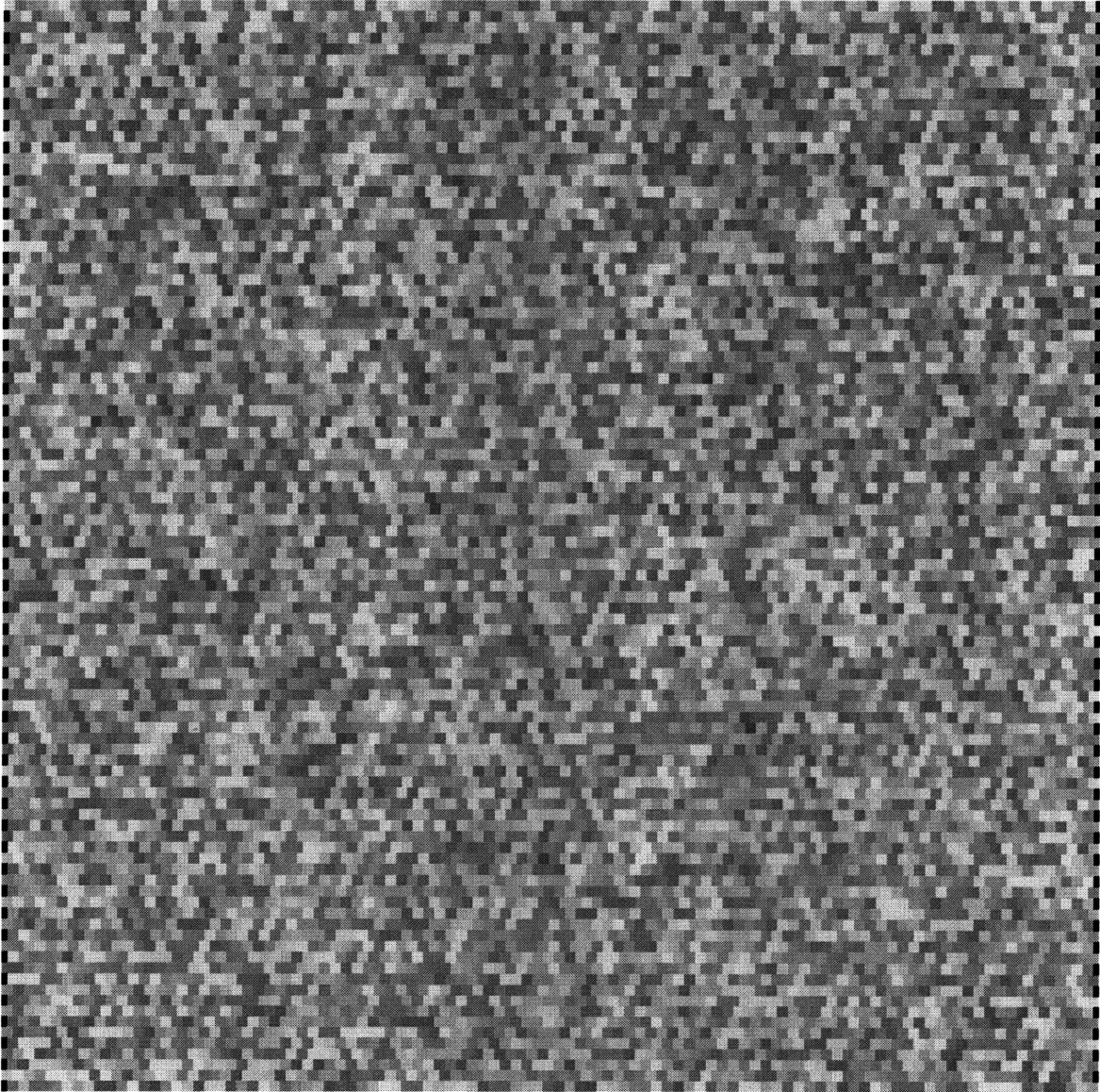


Figure 3-17: Simulated selectivity pattern generated by iterating Eq. (3.28). Here  $h'_i$  is distributed uniformly over the interval  $(-2, 2)$ , to widen the distribution of  $|z_i|$ . The large amount of randomness needed to widen the distribution of  $|z_i|$  disrupts the pattern of selectivity. In this simulation on a  $100 \times 100$  lattice,  $k'_s = 0.05$ ,  $\Delta t = 0.05$ . The simulation is interrupted after 2500 time constants when the pattern appeared to be stable.

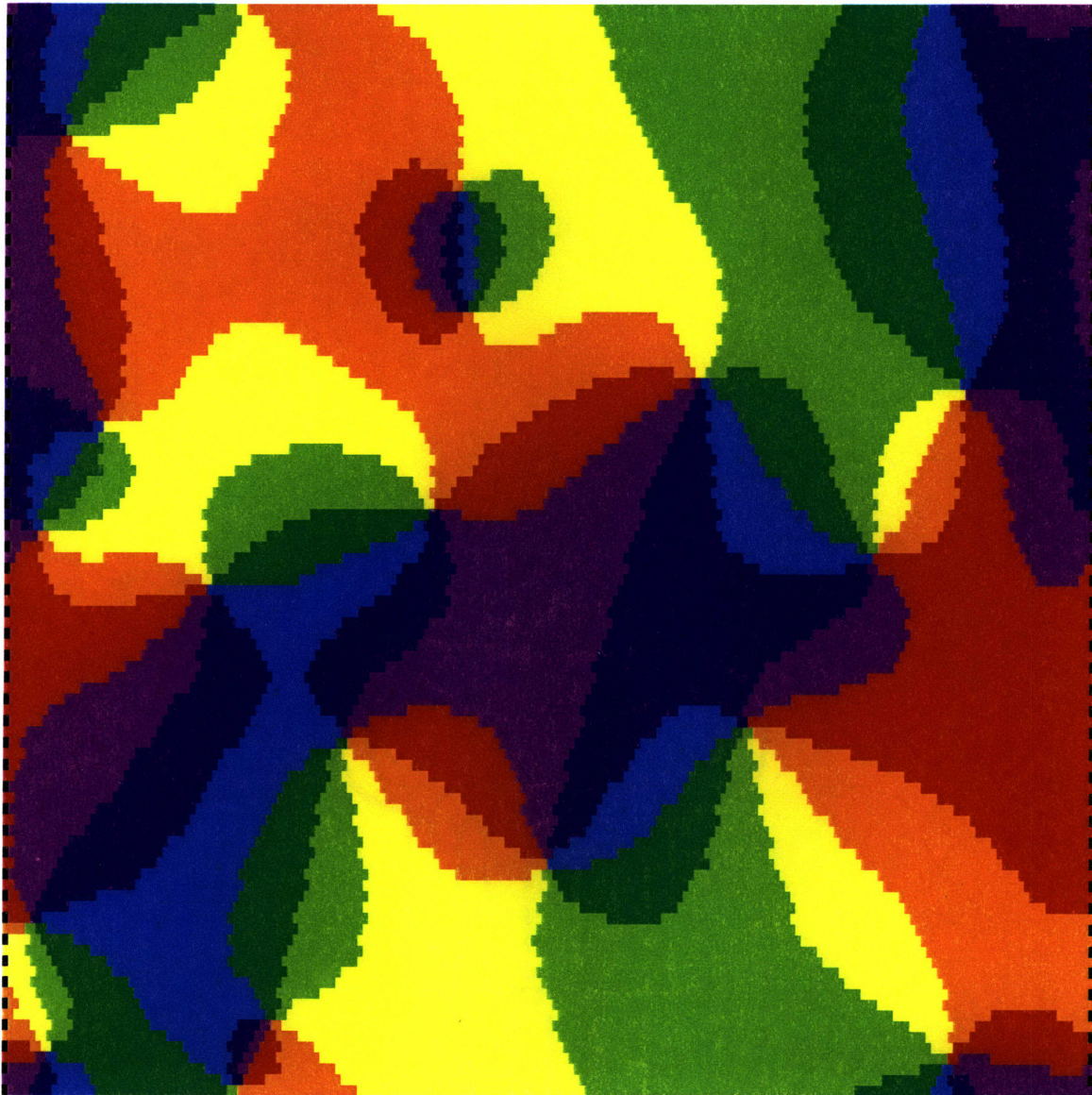


Figure 3-18: Simulated orientation pattern generated by iterating Eq. (3.28). This pattern is stable under further iteration. The presence of a quenched random field can stop the annihilation of vortices. This orientation pattern corresponds to the selectivity pattern shown in Fig. (3-17)

with a pattern of selectivity that is too uniform. Coupling randomness widens the distribution of  $|z_i|$  but also disrupts the pattern of selectivity. Our model also does not include the growth of the cortex. Since the density of pinwheels remains constant, new pinwheel must form as the cortex grows.

### 3.3 Coupling between Ocular Dominance and Orientation Selectivity

Coupling between ocular dominance and orientation selectivity can play an important role in the patterns of the two fields. Since orientation singularities lie in the center of ocular dominance bands, and lines of isoorientation meet ocular dominance domain walls perpendicularly, some form of coupling must exist. As we shall demonstrate, such interactions can also stabilize the pattern of pinwheels, and significantly effect the distribution of ocular dominance and selectivity.

#### 3.3.1 Local Variables and the Cost Function

We now construct a single cost function for the local variables of both fields. All the terms present in either individual cost function plus coupling terms must be included. As the coupling term must be invariant under  $m \rightarrow -m$  and independent of the complex angle, the simplest term allowed is  $m_i^2|z_i|^2$ . Higher order terms are possible in principle but not likely to be important in a macroscopic cost function. Our local cost function,

$$F(m_i, z_i) = a_2 m_i^2 + a_4 m_i^4 + a'_2 |z_i|^2 + a'_4 |z_i|^4 + \gamma m_i^2 |z_i|^2, \quad (3.30)$$

has five free parameters  $a_2$ ,  $a_4$ ,  $a'_2$ ,  $a'_4$ , and  $\gamma$ . Each  $m_i$  is coupled to the local  $z_i$ , resulting in coupled equations of motion,

$$\tau \frac{\partial m_i}{\partial t} = -2a_2 m_i - 4a_4 m_i^3 - 2\gamma m_i |z_i|^2, \quad (3.31)$$



$$\tau' \frac{\partial z_i}{\partial t} = -2a_2' z_i - 4a_4' z_i |z_i|^2 - 2\gamma z_i m_i^2, \quad (3.32)$$

where  $\tau$  and  $\tau'$  are time constants. To ensure finite, non-zero fixed points  $a_2$  and  $a_2'$  must be negative while  $a_4$  and  $a_4'$  are positive. By appropriately redefining  $F(m_i, z_i)$ ,  $m_i$ , and  $z_i$  we can absorb three of the coefficients and all the numeric factors, resulting in

$$\begin{aligned} \tau \frac{\partial m_i}{\partial t} &= m_i - m_i^3 - \gamma m_i |z_i|^2, \\ \tau' \frac{\partial z_i}{\partial t} &= z_i - z_i |z_i|^2 - \gamma' z_i m_i^2, \end{aligned} \quad (3.33)$$

where  $\gamma' = a_4'/a_4\gamma$ . The couplings,  $\gamma$  and  $\gamma'$ , do not have to be equal but must have the same sign. By introducing the term  $\gamma m_i^2 |z_i|^2$  in the cost function, we forced the interaction to be symmetric. However, we did not force the scale of ocular dominance and orientation preference to be similar. Eqs. (3.33) can be rewritten with identical coefficients for the coupling terms but different coefficients on the linear and cubic terms.

Our approach to coupling fields could easily be extended to include more fields or even a random field representing the effect of several fields. These additional fields appear in same manner as ocular dominance or orientation, each coupling to the square of the other fields, e.g. introducing a scalar field  $x_i$  adds terms to the cost function proportional to  $x_i^2 m_i^2$  and  $x_i^2 |z_i|^2$ . In principle a term such as  $x_i^2 m_i^2 |z_i|^2$  could also exist, but is less likely to be important due to its higher order. This could reflect some three way process where one field mediated an interaction between the other two, like a catalyst in a binary reaction. The local cost function now has 9 parameters,

$$F(m_i, z_i, x_i) = \sum_i (a_2 m_i^2 + a_4 m_i^4 + a_2' |z_i|^2 + a_4' |z_i|^4 + a_2'' x_i^2 + a_4'' x_i^4 + \gamma_{mz} m_i^2 |z_i|^2 + \gamma_{mx} m_i^2 x_i^2 + \gamma_{zx} x_i^2 |z_i|^2), \quad (3.34)$$

Rescaling leads to three coupled equations of motion, with 5 free parameters describ-

ing the coupling,

$$\begin{aligned}
\tau \frac{\partial m_i}{\partial t} &= m_i - m_i^3 - \gamma_1 m_i |z_i|^2 - \gamma_2 m_i x_i^2, \\
\tau' \frac{\partial z_i}{\partial t} &= z_i - z_i |z_i|^2 - \gamma_3 z_i x_i^2 - \gamma_4 z_i m_i^2, \\
\tau'' \frac{\partial x_i}{\partial t} &= x_i - x_i^3 - \gamma_5 x_i m_i^2 - \gamma_6 x_i z_i^2,
\end{aligned} \tag{3.35}$$

where  $\{\gamma_i\}$  are parameters with the constraint  $\gamma_1 \gamma_3 \gamma_5 = \gamma_2 \gamma_4 \gamma_6$ . This process can be continued in the obvious way for additional fields. A cost function for  $n$  fields results in  $n$  coupled equations with  $n(n-1)/2 - (2n+1)$  parameters. If field  $x_i$  has a very short relaxation time,  $\tau''$ , it quickly achieves its final values, acting as a random (although correlated) field on  $m_i$  and  $z_i$  at longer times.

### 3.3.2 Interactions

Based on our experience with uncoupled models for ocular dominance and orientation, we introduce interactions within each field. For orientation we introduce nearest neighbor interactions with strength  $k'_s > 0$ , while for ocular dominance we introduce an interaction,  $k(i, j)$ , that depends on the distance between site  $i$  and site  $j$ . For short distances  $k(i, j) > 0$  while for longer distances up to a cutoff  $k(i, j) < 0$ . The full equations of motion,

$$\begin{aligned}
\tau \frac{\partial m_i}{\partial t} &= -m_i - m_i^3 - \gamma m_i |z_i|^2 + \sum_j k(i, j) (m_j - m_i), \\
\tau' \frac{\partial z_i}{\partial t} &= z_i - z_i |z_i|^2 - \gamma' z_i m_i^2 + k'_s \sum_{j \in \text{n.n.}} (z_j - z_i),
\end{aligned} \tag{3.36}$$

contain five parameters in addition to the interaction  $k(i, j)$ . Setting  $\tau = 1$ ,  $\tau'$  should be determined by comparing the growth rate of orientation preference to ocular dominance. Unfortunately, there is currently not enough data on immature animals to compare the rates. For simplicity we set  $\tau' = \tau = 1$ , and add a further constraint of  $\gamma = \gamma'$ . There is no compelling reason for one field to play a dominate role over the other. Once again we choose to reverse the sign on the  $m_i$  term, as discussed in

Sec. (3.1.3).

### Coupling Between Defects

A small positive value of  $\gamma = \gamma'$  is enough to cause the vortices to tend to avoid the domain walls, see Fig. (3-19). The positive term  $\gamma m_i^2 |z_i|^2$  in the cost function of Eq. (3.30), implies that sites with both high ocular dominance and orientation selectivity incur an additional cost. Defects in either field, which have low values of  $m_i$  or  $z_i$ , can reduce the total cost by appearing at separate sites, so that two sites save a cost proportional to  $\gamma$  rather than just one site. (The existence of defects still adds to the total cost due to the other terms in the cost function.) The presence of orientation vortices in the center of ocular dominance bands leads to isoorientation lines which cross ocular dominance domains perpendicularly.

A positive value of  $\gamma$  indicates a competition between ocular dominance and orientation. In this case  $\gamma$  has the same sign as the quartic terms in the the cost function which limit the growth of the fields. If  $\gamma = 2$  these terms could be expressed as  $(m_i^2 + |z_i|^2)^2$ , a single term limiting the sum of the fields. A value of  $\gamma = 2$  appears to be too large, but the idea of competition still holds for weakly coupled fields.

Negative values of  $\gamma = \gamma'$  lead to vortices preferentially occurring on ocular dominance domain walls. In this case sites with either type of defect incur a cost proportional to  $\gamma$ , so that it is advantageous to have both types of singularities occur at a single site. This pattern, however, is not seen experimentally.

Large positive values of coupling distort the pattern of orientation and ocular dominance. The cortex becomes divided into regions responding only to orientation or only to ocular dominance. Across the centers of ocular dominance bands orientation becomes discontinuous. This discontinuity is similar to the fractures seen experimentally. However, for large coupling these fractures, rather than the pinwheels, become the dominant feature.

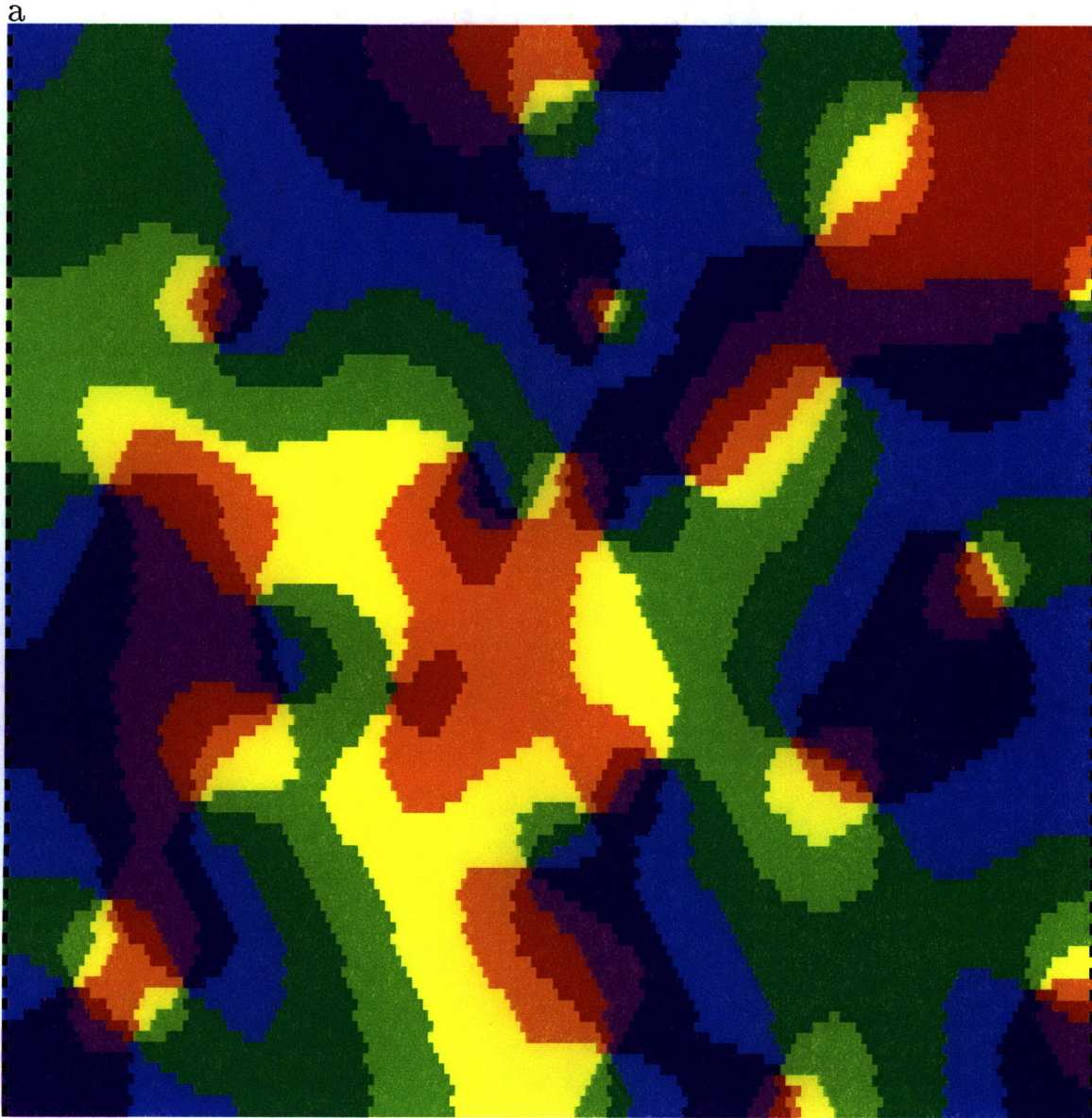
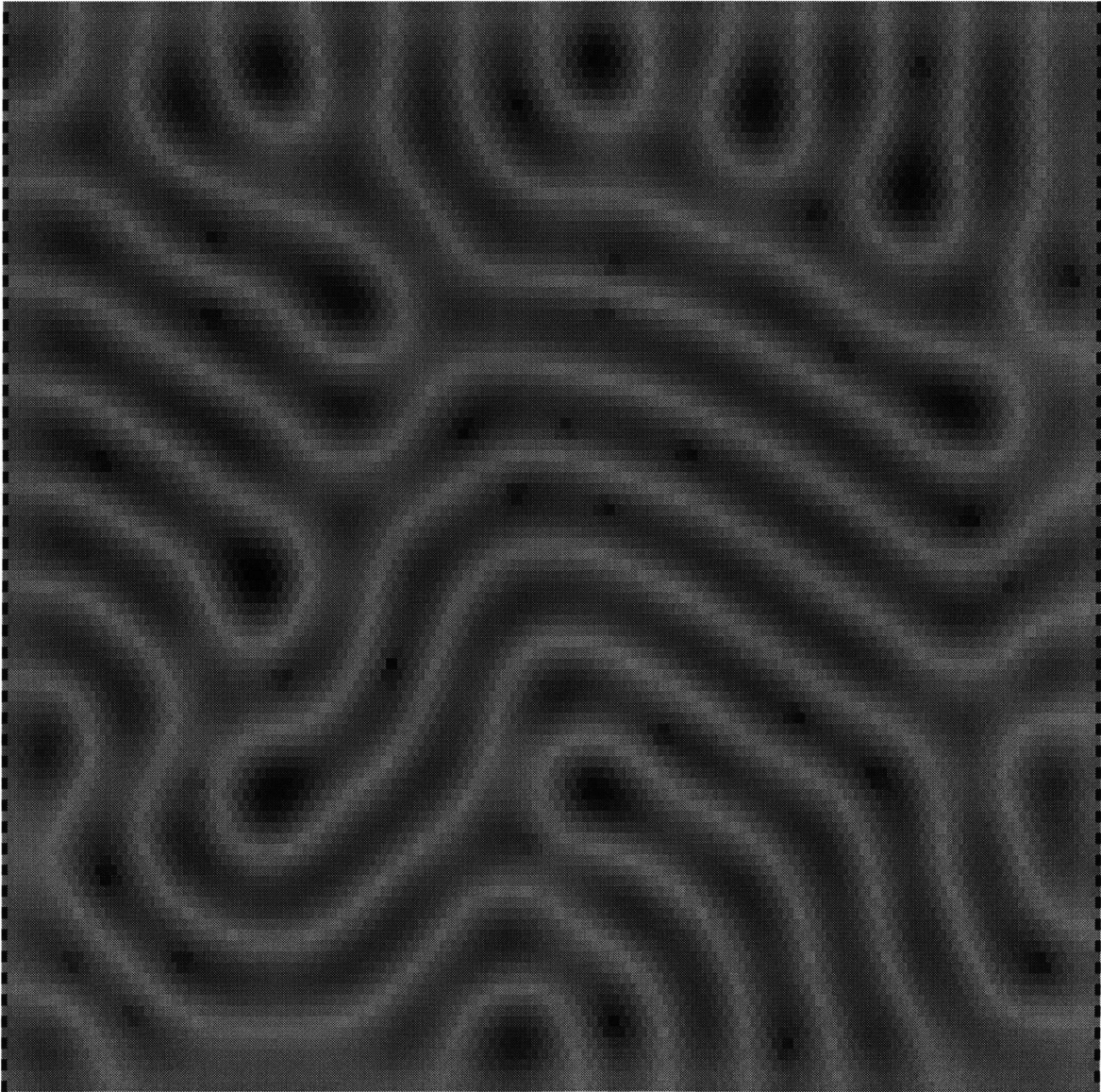
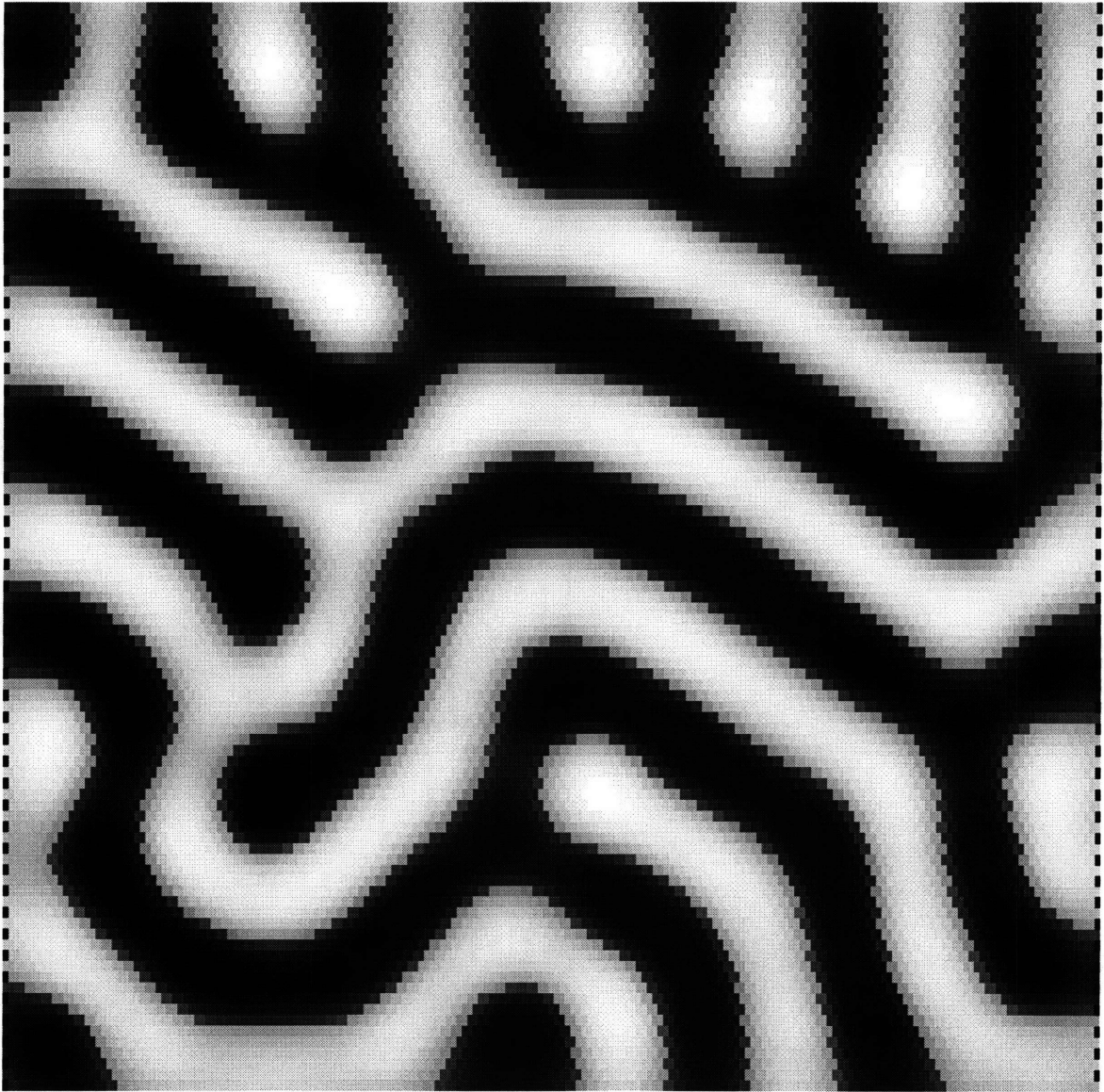


Figure 3-19: Simulated (a) orientation preference, (b) orientation selectivity, and (c) ocular dominance patterns generated by iterating Eqs. (3.36). The coupling between fields prevents the further annihilation of singularities. The locations of the singularities and ocular dominance domain walls are clearly visible in the orientation selectivity. In this simulation on a 100x100 lattice,  $\gamma = -0.1$ ,  $k_s^{(2)} = -0.05$ ,  $k_l^{(2)} = -0.025$ ,  $L = 10$ ,  $k'_s = 0.05$ , and  $\Delta t_m = \Delta t_z = 0.025$ . The equations of motion were iterated for 500 time constants. The pattern appeared to be stable during the last 250 time constants.

b



c



## Pinning the Defects

Coupling between ocular dominance and orientation preference can stabilize the pattern of orientation vortices. These defects are not able to pass through the barrier created by thick ocular dominance domain walls. Thin ocular dominance walls, created by nearest neighbor interactions, can be crossed by the vortices, so further neighbor interactions are necessary in the ocular dominance field. The singularities also become trapped by bends in the ocular dominance bands, as shown in Fig. (3-19).

A pattern free of vortices still has the globally lowest cost. However, the initial conditions do not evolve to the global minimum. Instead they become trapped in a local minimum that still contains vortices. Since vortices are topological defects they can only be removed by annihilation with opposite vortices (or edge effects). Due to the coupling, the ocular dominance domain walls are barriers to vortex migration. Moving onto a domain wall increases the cost of the pattern and is prohibited even though a lower cost may be achieved when the vortex has passed completely through the barrier. Domain walls formed by only nearest neighbor interactions are only 1 or 2 sites thick. Since a vortex suppresses ocular dominance in a 1 or 2 site radius (see Sec. (3.3.3) ), it can create a node in the domain wall as it passes through.

The typical distance between singularities is strongly influenced by the width and persistence of the ocular dominance bands. The width of bands forces the separation in the direction perpendicular to the bands to be at least of the order of the band width. In the direction parallel to the bands, the typical separation between singularities is limited by the persistence. In frequently branching and bending bands, the singularities are quickly trapped as they move within a band. In relatively straight bands, many singularities can move a significant distance without becoming entangled in the domain walls.

### 3.3.3 Distribution of $|z_i|$ and $|m_i|$

Coupling between orientation and ocular dominance effects the distribution of  $|z_i|$  and  $|m_i|$ , as well as the patterns of selectivity. It widens the distributions, bringing them

closer to the experimental observations. However, coupling alone does not widen the distributions sufficiently without causing disruption of patterns. Even together with long range ocular dominance interactions, the distributions are not sufficiently wide, as shown in Fig. (3-20).

An undesired feature of the couplings is its influence on the pattern of selectivity, as shown in Figure (3-19). Unlike the experimental case, the ocular dominance domains become visible in the patterns of selectivity. While the strength of this effect varies with the magnitude of  $\gamma$ , it is visible even at very small values of the coupling. Coupling to additional fields, or random noise, may disguise the effect from visual observation, but it would still be detectable statistically. No published statistical analysis of experimental data has shown any sign of the ocular dominance domain walls in orientation selectivity patterns.

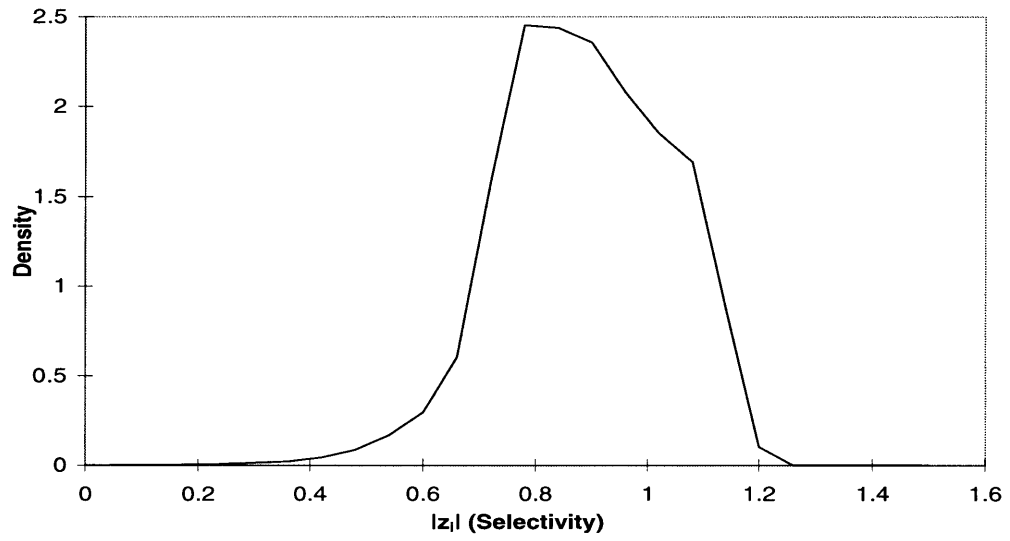
### 3.3.4 Summary

Introducing a coupling between the ocular dominance and the orientation selectivity models can create a tendency for the defects in the two fields to avoid each other. Thus, the orientation vortices stay away from the ocular dominance domain walls. A similar effect has been reported in the monkey. Placing the vortices in the center of ocular bands naturally causes lines of isoorientation to cross domain walls nearly perpendicularly. The coupling between the fields also stabilizes the pattern of orientation preference as vortices cannot migrate through thick domain walls. This method of stabilizing the ocular dominance pattern gives a possible explanation for the observation that pinwheel separation and ocular dominance bands appear to have very similar length scales.

Coupling the fields also presents a way to widen the distribution of  $m_i$  and  $z_i$ , so that they more closely match observations. Despite this improvement, there still appears to be a significant disparity between the modeled distributions and the actual ones. However, these distributions are one of the least studied experimental features, and their description is not precisely known. A more serious defect of the coupling is the influence of the ocular dominance domain walls on the patterns of selectivity.



a



b

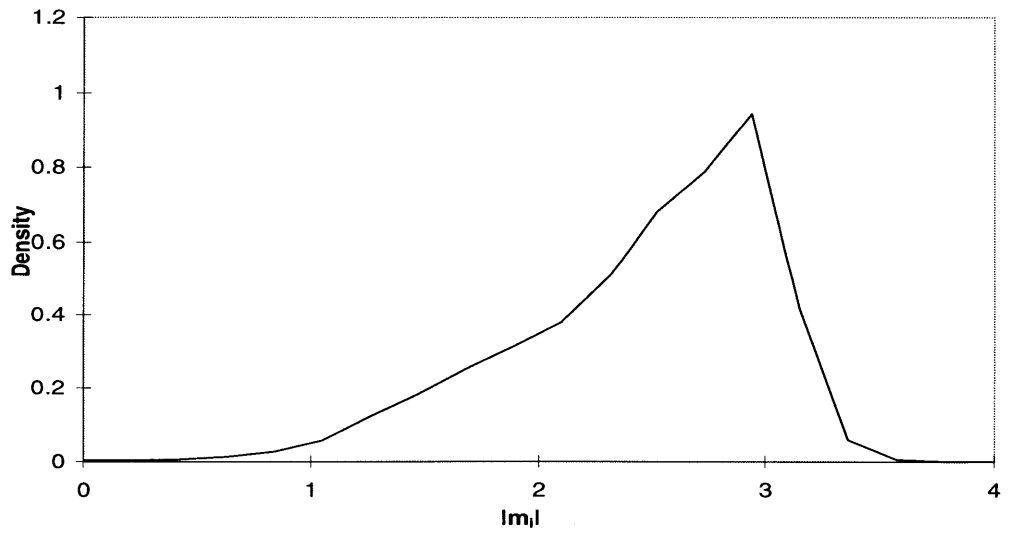


Figure 3-20: The distribution of (a)  $|z_i|$  and (b)  $|m_i|$ , corresponding to the patterns in Fig. (3-19).

This has not been reported in experiments to our knowledge.

# Chapter 4

## Conclusions

### **Insights from Macroscopic Modeling**

Using macroscopic modeling with a Landau-Ginzburg approach we are able to reproduce many of the features in the primary visual cortex. This approach highlights the nature and symmetry of the emergent properties of the cortex, and provides insight into the key features that are frequently missed in microscopic models.

We model ocular dominance as a real number indicating the dominant eye and the degree of preference. The symmetry between the two eyes limits the equations of our model to those unchanged under globally exchanging the eyes' responses. Initial conditions, reflecting a nearly binocular response, develop into a pattern of domains of two different preferred values, corresponding to the observed monocular bands. This development occurs during a critical period during which the model is sensitive to perturbations. The domains are separated by domain walls where the modeled ocular dominance changes rapidly. Competition between short range excitations, which favor continuity, and long range inhibitions, which favor diversity, stabilizes the domains, and results in a pattern of stripes. Without this competition, a system containing domain wall defects coarsens to minimize the length of the domain walls, eventually resulting in uniform (monocular) response.

We model orientation as a complex number to reflect both preference and selectivity. The symmetry among all orientations limits the equations of our model to a

few phenomenological parameters. Using these equations of motion to evolve random initial conditions, we create patterns which contain vortices, the natural defects in angular fields, which are naturally associated with the pinwheels observed in the cortex. As the vortices in an isolated angular field slowly annihilate leaving a single uniform angle, we expect that some external coupling stabilizes the pattern. We find that coupling to quenched noise, or to the pattern of ocular dominance, can stabilize the pattern of orientation.

In addition to stabilizing orientation patterns, coupling between the ocular dominance and orientation explains the tendencies for pinwheels to avoid the edges of ocular dominance bands. It is natural to think of this coupling as a result of the cortex's limited computational capacity, e.g. areas which respond strongly to orientation cannot simultaneously respond strongly to ocular dominance. This coupling links the typical separation between vortices to the length scales of the ocular dominance domains. This may explain why both features are observed to have very similar length scales. However, we must consider this interpretation with caution. Both orientation and ocular dominance are mediated by neural activity which has an inherent length scale. The size of neural arbors is roughly commensurate with both the band width and the separation between pinwheels.

It is also possible to stabilize the pattern of vortices by weakly coupling to a large number of number of fields. If one of these fields is ocular dominance, the vortices can still be driven away from the domain walls, but this will avoid the side effects from strong ocular dominance-orientation coupling that we have observed in our simulations. A more generalized coupling can also explain the presence of stable orientation patterns in animals which do not have detectable ocular dominance bands. The coupling between a large number of fields can again be motivated by competition for a limited computational capacity.

## **Open Questions**

Despite the success of macroscopic modeling, several questions remain open. The distribution of orientation selectivity and the magnitude of ocular dominance are not

modeled well by our approach. Most other models have not looked explicitly at these distributions (but do not seem to do any better), so it is an area in need of further study. The distribution of ocular dominance magnitude reflects the sharpness of the domain walls and plays an important role in monocular deprivation. Stripes with narrow domain walls are not able to easily narrow under the influence of monocular deprivation. Since limited information is currently available about these distributions, a better experimental study of these distributions would significantly guide the development of models.

The primary visual cortex grows significantly during the formation of orientation and ocular dominance patterns. Modeling this growth in a robust way has not yet been attempted. Simulating growth of the cortex requires adding lattice points during the simulation to reflect the addition of new cells. Coupling between growth and ocular dominance is necessary to explain the propensity of the growth to be perpendicular to the bands. Modeling growth also requires the spontaneous creation of vortex pairs, as the pinwheel density appears to remain constant. Additional experiments that probe the evolution of patterns during development will provide much more stringent tests for developmental models than are currently available.

More detailed characterization of the observed patterns will help greatly in differentiating between models. Currently, much of the comparison between model and experiment is simply visual. The use of fourier spectra provide some additional means of comparison, but again the comparison is mostly visual. Measuring correlation functions and characterizing possible defects allows more quantitative comparisons than discussions of linear zones, saddle points, fractures, and singularities. Recently Obermayer and Blasdel have begun work in this direction, measuring correlation functions in orientation patterns and finding that patterns cannot be entirely specified by the positions of their pinwheels.[71] Work in this direction will lead to additional quantitative tests for models and more insight into the working of the visual cortex.

# Bibliography

- [1] Eric R. Kandel, James H. Schwartz, and Thomas M. Jessell. *Principles of Neural Science*. Appleton & Lange, 1991.
- [2] Daniel J. Felleman and David C. Van Essen. Distributed hierarchical processing in the primate cortex. *Cerebral Cortex*, 1:1–47, 1991.
- [3] Simon LeVay, David H. Hubel, and Torsten N. Wiesel. The pattern of ocular dominance columns in macaque visual cortex revealed by reduced silver stain. *Journal of Comparative Neurology*, 159:559–576, 1975.
- [4] Gary G. Blasdel. Orientation selectivity, preference, and continuity in the monkey striate cortex. *The Journal of Neuroscience*, 12:3139–3161, 1992.
- [5] James T. McIlwain. *An Introduction to the Biology of Vision*. Cambridge University Press, 1996.
- [6] H. K. Hartline. The receptive fields of the optic nerve fibers. *American Journal of Physiology*, 130:690–699, 1940.
- [7] S. W. Kuffler. Discharge patterns and the functional organization of the mammalian retina. *Journal of Neurophysiology*, 16:37–68, 1953.
- [8] David H. Hubel. Evolution of ideas on the primary visual cortex, 1955-1978: A biased historical account. *Bioscience Reports*, 2:435–469, 1982.
- [9] S. W. Kluffler. Discharge patterns and functional organization of mammalian retina. *Journal of Neurophysiology*, 16:37–68, 1953.

- [10] D. H. Hubel and T. N. Wiesel. Functional architecture of macaque monkey visual cortex. *Proc. R. Soc. Lond. B*, 198:1–59, July 1977.
- [11] David H. Hubel, Torsten N. Wiesel, and Michael P. Stryker. Anatomical demonstration of orientation columns in macaque monkey. *Journal of Comparative Neurology*, 177:361–380, 1978.
- [12] W. J. H. Nauta and R. A. Gygax. Silver impregnation of degenerating axons in the central nervous system. *Stain Technology*, 29:91–93, 1954.
- [13] R. P. Fink and L. Heimer. Two methods for selective silver impregnation of degenerating axons and the synaptic endings in the central nervous system. *Brain Research*, 4:367–374, 1967.
- [14] D. H. Hubel and T.N. Wiesel. Laminar and columnar distribution of geniculocortical fibers in the monkey striate cortex. *Journal of Comparative Neurology*, 146:421–450, 1972.
- [15] R. Lasok, B. S. Joseph, and D. G. Whitlock. Evaluation of radiographic neuroanatomical tracing method. *Brain Research*, 8:319–336, 1968.
- [16] B. Grafstock. Transneuronal transfer of radioactivity in the central nervous system. *Science*, 172:177–179, 1971.
- [17] T. N. Wiesel, D. H. Hubel, and D. M. K. Lam. Autoradiographic demonstration of ocular-dominance columns in the monkey striate cortex by means of transneuronal transport. *Brain Research*, 79:273–279, 1974.
- [18] L. Sokoloff, M Reivich, C. S. Patlak, K. D. Pottigrew, M Des Rosiers, and C Kennedy. The [ $^{14}\text{C}$ ]-deoxyglucose method for the quantitative determination of local cerebral glucose consumption. *Transactions of the American Society for Neurochemistry*, 5:85, 1974.
- [19] C. Kennedy, M. H. Des Rosiers, O. Sakurada, and M Shinohara. Metabolic mapping of the primary visual system of the monkey by means of the autora-

- diographic [ $^{14}\text{C}$ ]-deoxyglucose technique. *Proceedings of the National Academy of Science (U.S.A.)*, 73:4230–4234, 1976.
- [20] L. B. Cohen, R. D. Keynes, and D Landowne. Changes in axon light-scattering that accompanies the action potential: current dependent components. *Journal of Physiology (London)*, 224:727–752, 1972.
- [21] Harry S. Orbach, Lawrence B. Cohen, and Amiram Grinvald. Optical mapping of electrical activity in rat somatosensory and visual cortex. *The Journal of Neuroscience*, 5(7):1886–1895, 1985.
- [22] Gary G. Blasdel and Guy Salama. Voltage-sensitive dyes reveal a modular organization in the monkey striate cortex. *Nature*, 321:579–585, 1986.
- [23] A Grinvald, E Lieke, R D Frostig, C D Gilbert, and T N Wiesel. Functional architecture of cortex revealed by optical imaging of intrinsic signals. *Nature*, 324:269–291, 1986.
- [24] Arthur W. Toga and John C. Mazziotta. *Brain Mapping: The Methods*. Academic Press, 1996.
- [25] Gary G. Blasdel. Differential imaging of ocular dominance and orientation selectivity in monkey striate cortex. *The Journal of Neuroscience*, 12:3115–3138, 1992.
- [26] V B Mountcastle. Modality and topographical properties of single neurons of a cat’s somatic sensory cortex. *Journal of Neurophysiology*, 20:408–432, 1957.
- [27] P. Rakic. Prenatal development of the visual system in the rhesus monkey. *Philosophical Transactions of the Royal Society of London B*, 278:245–260, 1977.
- [28] D. H. Hubel, T. N. Wiesel, and S LeVay. Plasticity of ocular dominance columns in the monkey striate cortex. *Philosophical Transactions of the Royal Society of London B*, 278:377–410, 1977.



- [29] D. Purves and A. LaMantia. Development of blobs in the visual cortex of macaques. *Journal of Comparative Neurology*, 322:1–7, 1993.
- [30] Gary G. Blasdel, Klaus Obermayer, and Lynne Kiorpes. Organization of ocular dominance and orientation columns in the striate cortex of neonatal macaque monkeys. *Visual Neuroscience*, 12:589–603, 1995.
- [31] Mirganka Sur. Study of unpublished data for orientation selectivity and preference in the ferret.
- [32] F. Worgotter and U. Th. Eysel. Quantitative determination of orientation and directional components in the response of visual cortical cells to moving stimuli. *Biological Cybernetics*, 57:349–355, 1987.
- [33] Barbara Chapman and Michael P. Stryker. Development of orientation selectivity in ferret visual cortex and effects of deprivation. *Journal of Neuroscience*, 13:5251–5262, 1983.
- [34] Klaus Obermayer and Gary G. Blasdel. Geometry of orientation and ocular dominance columns in monkey striate cortex. *The Journal of Neuroscience*, 13:4114–4129, 1993.
- [35] T. N. Wiesel and D. H. Hubel. Ordered arrangement of orientation columns in monkeys lacking in visual experience. *Journal of Comparative Neurology*, 158:308–318, 1974.
- [36] E Erwin, Klaus Obermayer, and K Schulten. Models of orientation and ocular dominance columns in the visual cortex: A critical comparison. *Neural Computation*, 7:425–468, 1995.
- [37] N V Swindale. The development of topography in the visual cortex: A review of models. *Network*, 7:161–247, 1996.
- [38] Klaus Obermayer, H Ritter, and K Schulten. A principle for the formation of the spatial structure of cortical feature maps. *Proceedings of the National Academy of Science, USA*, 87:8345–8349, 1990.

- [39] N. V. Swindale. A model for the formation of ocular dominance stripes. *Proceeding of the Royal Society of London, Series B*, 208:243–264, 1980.
- [40] N. V. Swindale. Coverage and the design of striate cortex. *Biological Cybernetics*, 65:415–424, 1991.
- [41] N. V. Swindale. Is the cerebral cortex modular? *Trends in Neuroscience*, 13:487–492, 1990.
- [42] V. Braitenberg and C. Braitenberg. Geometry of orientation columns in the visual cortex. *Biological Cybernetics*, 33:179–186, 1979.
- [43] K. G. Gotz. Do “d-blob” and “l-blob” hypercolumns tessellate the monkey visual cortex? *Biological Cybernetics*, 56:107–109, 1987.
- [44] A. S. Rojer and E. L. Schwartz. Cat and monkey cortical columnar patterns modeled by bandpass-filtered 2d white noise. *Biological Cybernetics*, 62:381–391, 1990.
- [45] Ernst Niebur and Florentin Worgotter. Orientation columns from first principles. In Frank H Eeckman and James Bower, editors, *Computation and Neural Systems*, chapter 62. Kluwer Academic Publishers, 1993.
- [46] Stephen Grossberg and Steven J Olson. Rules for the cortical map of ocular dominance and orientation columns. *Neural Networks*, 7:883–894, 1994.
- [47] A M Turing. The chemical basis for morphogenesis. *Philosophical Transactions of the Royal Society of London B*, 237:37–72, 1952.
- [48] Basabi Bhaumik and Chotta M Markan. A reaction-diffusion model for sequential development of orientation and ocular dominance maps. preprint.
- [49] N. V. Swindale. A model for the formation of orientation columns. *Proceeding of the Royal Society of London, Series B*, 215:211–230, 1982.
- [50] N. V. Swindale. A model for the coordinated development of columnar systems in primate striate cortex. *Biological Cybernetics*, 66:217–230, 1992.

- [51] John Hertz, Anders Krogh, and Richard G. Palmer. *Introduction to the Theory of Neural Computation*. Addison-Wesley Publishing Company, 1991. For a description of computational neural networks see this or a similar work.
- [52] Teuvo Kohonen. Self-organization of topologically correct feature maps. *Biological Cybernetics*, 43:59–69, 1982.
- [53] Ralph Linsker. From basic network principles to neural architecture: Emergence of spatial-opponent cells. *Proceedings of the National Academy of Science, USA*, 83:7508–7512, 1986.
- [54] Chr. von der Malsburg. Self-organization of orientation sensitive cells in the striate cortex. *Kybernetik*, 14:85–100, 1973.
- [55] Richard Durbin and Graeme Mitchison. A dimension reduction framework for understanding cortical maps. *Nature*, 343:644–647, 1990.
- [56] Ralph Linsker. From basic network principles to neural architecture: Emergence of spatial-opponent cells. *Proceedings of the National Academy of Science, USA*, 83:8390–8394, 1986.
- [57] Ralph Linsker. From basic network principles to neural architecture: Emergence of spatial-opponent cells. *Proceedings of the National Academy of Science, USA*, 83:8779–8783, 1986.
- [58] Kenneth D Miller, Joseph B Keller, and Michael P Strker. Ocular dominance columns development: Analysis and simulation. *Science*, 245:605–615, 1989.
- [59] Kenneth D Miller. Receptive fields and maps in the visual cortex: Models of ocular dominance and orientation columns. preprint.
- [60] L D Landau. On the theory of phase transitions. In D. Ter Haar, editor, *Collected Papers of L. D. Landau*, chapter 29, pages 193–216. Gordon and Breach, 1967.
- [61] L D Landau. On the theory of phase transitions. *Journal of Experimental and Theoretical Physics (Russian Language)*, 11:26, 1937.

- [62] V L Ginzburg and L D Landau. On the theory of superconductivity. In D. Ter Haar, editor, *Collected Papers of L. D. Landau*, chapter 73, pages 546–568. Gordon and Breach, 1967.
- [63] V L Ginzburg and L D Landau. On the theory of superconductivity. *Journal of Experimental and Theoretical Physics (Russian Language)*, 20:1064, 1950.
- [64] Charles Kittel and Herbert Kromer. *Thermal Physics*. W. H. Freeman and Company, 1980.
- [65] L P Gor'kov. Microscopic derivation of the ginzburg-landau equations on the theory of superconductivity. *Soviet Physics JETP*, 10:1064, 1959.
- [66] Kerson Huang. *Statistical Mechanics*. John Wiley & Sons, 1987.
- [67] Charles Kittel. *Introduction to Solid State Physics*. John Wiley & Sons, 1986.
- [68] J. R. Schrieffer. *Theory of Superconductivity*. Addison-Wesley Publishing Company, 1983.
- [69] A A Abrikosov. On the magnetic properties of superconductors of the second group. *Soviet Physics JETP*, 32:1174–1182, 1957.
- [70] P C Hohenberg and B I Halperin. Theory of dynamic critical phenomena. *Reviews of Modern Physics*, 49:435–479, 1977.
- [71] Klaus Obermayer and Gary G. Blasdel. Singularities in primate orientation maps. *Neural Computation*, 9:555–575, 1997.